MAGNETIC MEASUREMENTS
OF ANTIFERROMAGNETIC
KMnC1₃· 2H₂ O AND LiGuC1₃· 2H₂ O

Thesis for the Degree of Ph. D.
MICHIGAN STATE UNIVERSITY
PETER TONE BAILEY
1971



This is to certify that the

thesis entitled

MAGNETIC MEASUREMENTS OF ANTI-FERROMAGNETIC KMnCl₃·2H₂O AND

LiCuCl₃·2H₂O presented by

Peter Tone Bailey

has been accepted towards fulfillment of the requirements for

Ph.D. degree in Physics

Major professor

Date 5/21/71

O-7639



ABSTRACT

MAGNETIC MEASUREMENTS OF ANTIFERROMAGNETIC KMnCl₃·2H₂O AND LiCuCl₃·2H₂O

By

Peter Tone Bailey

A molecular field theory for calculating the anisotropy and exchange fields from the magnetic phase boundaries is given. The theory for $\text{LiCuCl}_3 \cdot 2\text{H}_2\text{O}$ assumes an intersublattice exchange, J_1 , and an intrasublattice exchange, J_2 , and a uniaxial anisotropy. This gives the field dependence of the transition temperature in terms of J_1 and J_2 .

For KMnCl₃·2H₂O, a two dimensional Ising model with eight sublattices is used. The centers of the ferromagnetic dimers are coplanar, and the dimers have an antiferromagnetic arrangement with each other. Assuming that a particular sublattice flops 180° at each of the four regions above the antiferromagnetic state, four spin interactions are calculated from the four boundary values at T=O°K. A brief theory of the effects of a non-uniaxial anisotropy is mentioned.

Specific heat measurements, field rotations, and field sweeps were done adiabatically to determine the magnetic phase boundaries. The apparatus and methods are described. For $\text{LiCuCl}_3 \cdot 2\text{H}_2\text{O}$, the results show a triple point at 4.2^{O}K and 12.7 kG. The ratio of J_2/J_1 is 17, implying a relatively large intrasublattice exchange. The total exchange field is 12.5 kG, and the anisotropy field is 3.1 kG. The rotations show that the spins flop in the AC plane, and the variation of the paramagnetic boundary for different field orientations indicates a non-uniaxial anisotropy.

The results for KMnCl₃·2H₂O show five distinct magnetic phases. Using field sweeps, two boundaries are found near 12 kG and 14 kG that look like first order spin flop boundaries. The other boundaries appear to be second order phase transititions since the specific heat shows an anomaly as the boundary is crossed. The magnetic field rotations show that in the first phase above the antiferromagnetic state, some or all of the spins may flop in one plane. Then in the second phase above the antiferromagnetic state, the spins may flop in another plane that is nearly perpendicular to the first one.

With the field perpendicular to the easy axis, specific heat measurements indicate an antiferromagnetic to paramagnetic boundary with less curvature than for the case with the field parallel to the easy axis. In a

second perpendicular position (90° from the above perpendicular position), two boundaries were observed. One boundary was similar to the other perpendicular one, and the other was somewhat more curved.

After extrapolating the phase diagram boundaries to T=0°K, the zero temperature field splitting for the lower magnetic phases is comparable to that for the upper magnetic phases as predicted from the Ising theory.

MAGNETIC MEASUREMENTS OF ANTIFERROMAGNETIC

 $\mathtt{KMnCl}_3 \cdot \mathtt{2H}_2\mathtt{O}$ AND $\mathtt{LiCuCl}_3 \cdot \mathtt{2H}_2\mathtt{O}$

Ву

Peter Tone Bailey

A THESIS

Submitted to
Michigan State University
in partial fulfillment of the requirements
for the degree of

DOCTOR OF PHILOSOPHY

Department of Physics

1971

PLEASE NOTE:

Some Pages have indistinct print. Filmed as received.

UNIVERSITY MICROFILMS

c=70/61

ACKNOWLEDGMENTS

The author wishes to express his thanks to all those who have helped in this study: to Dr. H. Forstat for invaluable assistance during the research; to Dr. J. A. Cowen and Dr. R. D. Spence for helpful discussions; to Mr. John R. Ricks for help with the experiments and data processing; and especially to the Air Force Office of Scientific Research, Office of Aerospace Research, United States Air Force for their financial support of this work.

TABLE OF CONTENTS

Chapte	r							Page
LIST O	F TA	ABLES	•	•	•	•	•	v
LIST O	F F	GURES	•	•		•	•	∀ii
INTROD	UCTI	ON	•	•	•	•	•	1
I.	GENE	RAL THEORY	•	•	•	•	•	2
	A.	Models for Antiferromagnetism .	•	•			•	2
•	в.	The Anisotropy Field	•	•			•	3
(c.	Spin Flopping	•	•			•	4
1	D.	Observing Spin Flop Boundaries .	•	•	•			7
•	Ε.	Observing Paramagnetic Boundarie						8
;	F.	Demagnetization Corrections						10
		•					-	
II.	LiCi	Cl ₃ ·2H ₂ 0 THEORY	•	•	•	•	•	11
III.	KMn(13.2H ₂ 0 THEORY	•	•	•	•	•	24
	A.	Ising Model	•	•	•	•	•	24
•	в.	Dipolar Anisotropy	•	•	•	•	•	31
(c.	The AF-P Perpendicular Boundary	•	•			•	32
IV.	EXPE	CRIMENTAL METHODS	•	•	•		•	37
	Α.	Experimental Apparatus	•	•			•	37
		1. Dewar and Calorimeter		•				37
		2. Sample Holder				•	•	41
		3. Vacuum Pumps					•	43 43
		 Pressure Gauges Thermometer Current Supplies 	•	•	•	•	•	45
		6. Measuring Electronics	•	•	•	•	•	46
		7. Magnet and Gaussmeter						48
	в.	Experimental Procedures	•	•	•	•	•	49
		1. Sample Preparation						49
		2. Preparing for Experiment						51

Chapte	er		Page
		3. Helium Transfer and Thermometer	5 2
		Calibration	52
		4. Adiabatic Field Rotations	54
		5. Adiabatic Magnetizations	55
		6. Specific Heat Measurements	56
		7. Removing Crystal	57
	C.	Data Analysis	58
		1. Converting Pressure to Temperature	58
		2. Thermometer Calibration Equation	58
		3. Chart Recorder Calibration	59
		4. Specific Heat, Rotations, Field	
		Sweeps	62
v.	LiC	uCl ₃ ·2H ₂ 0 RESULTS	63
	A.	Adiabatic Rotations	63
	в.	Adiabatic Magnetizations	63
	c.	Antiferromagnetic-Paramagnetic Boundary .	73
		-	
		1. Field Parallel to Easy Axis	73
		2. Field Perpendicular to Easy Axis	76
	D.	Antiferromagnetic-Spin Flop Boundary	78
	E.	Spin Flop-Paramagnetic Boundary	79
	F.	Anisotropy Energy	80
VI.	KMn	Cl ₃ ·2H ₂ O RESULTS	81
	A.	Adiabatic Rotations	81
	В.	"Antiferromagnetic-Spin Flop"	
	_ •	Boundaries	94
	c.	Easy Axis Shift	99
	_	-	
	D.	Antiferromagnetic-Paramagnetic and "Spin Flop-Paramagnetic" Boundaries	104
	E.	Exchange and Anisotropy Fields	105
CONCLU	JSION	NS AND SUGGESTIONS FOR FURTHER WORK	110
REFERE	ENCES	3	112
A TO TO EVALUE	\TV		111

LIST OF TABLES

Table				Page
1.	LiCuCl ₃ ·2H ₂ 0 AC plane isentropic rotations .	•	•	114
2.	LiCuCl ₃ ·2H ₂ 0 BC' plane isentropic rotations	•	•	115
3.	LiCuCl ₃ ·2H ₂ 0 isentropic magnetizations	•	•	116
4.	LiCuCl ₃ ·2H ₂ 0 specific heat data	•	•	117
5.	LiCuCl ₃ ·2H ₂ 0 isentropic magnetization critical fields	•	•	118
6.	LiCuCl ₃ ·2H ₂ 0 specific heat maximasample 1	•	•	119
7.	LiCuCl ₃ ·2H ₂ 0 angular dependence of critical field	•		119
8.	KMnCl ₃ ·2H ₂ 0 plane 1 isentropic rotations - twin	•	•	120
9.	KMnCl ₃ ·2H ₂ 0 plane 2 isentropic rotations - twin	•	•	121
10.	<pre>KMnCl₃·2H₂0 plane l isentropic rotations - single</pre>	•	•	122
11.	<pre>KMnCl₃·2H₂0 plane 2 isentropic rotations - single</pre>	•	•	123
12.	<pre>KMnCl₃·2H₂0 plane 3 isentropic rotations - single</pre>	•	•	124
13.	<pre>KMnCl₃·2H₂0 plane 4 isentropic rotations - single</pre>	•	•	125
14.	KMnCl ₃ ·2H ₂ 0 isentropic magnetization boundary points	_	_	126

Table	e	Page
15.	KMnCl ₃ ·2H ₂ 0 specific heat maxima	127
16.	KMnCl ₃ ·2H ₂ 0 isentropic magnetizations	128
17.	KMnCl ₃ ·2H ₂ 0 critical field angular dependence, single crystal	129
18.	KMnCl ₃ ·2H ₂ 0 critical field angular dependence and rotation minima, twin crystal	130
19.	KMnCl ₃ ·2H ₂ 0 specific heat data - twin	131
20.	<pre>KMnCl₃·2H₂0 isentropic magnetizations, 2/13/70</pre>	132

LIST OF FIGURES

Figur	re	Page
1.	LiCuCl ₃ ·2H ₂ 0 spin arrangement	. 12
2.	Definition of angles and vectors	. 16
3.	KMnCl ₃ ·2H ₂ 0 8 spin unit	. 25
4.	KMnCl ₃ ·2H ₂ 0 two dimensional dimer arrangement	. 26
5.	KMnCl ₃ ·2H ₂ 0 J ₃ interaction in BC plane and Ising spin model	. 28
6.	Pyrex helium dewar	. 38
7.	Cross section of body of calorimeter	. 39
8.	Front and side cross sections of top of calorimeter	. 40
9.	Sample holders	. 42
10.	Schematic diagram of pumping systems	. 44
11.	Diagram of electrical measuring circuits	. 47
12.	Example of data on chart recorder	. 61
13.	LiCuCl ₂ ·2H ₂ 0 AC plane isentropic rotations .	. 64
14.	LiCuCl ₃ ·2H ₂ 0 BC' plane isentropic rotation	. 65
15.	LiCuCl ₃ ·2H ₂ 0 BC' plane isentropic rotations .	. 66
16.	LiCuCl ₃ ·2H ₂ 0 isentropic magnetizations	. 68
17.	LiCuCl ₃ ·2H ₂ 0 specific heat data	. 69
18.	LiCuCl ₃ ·2H ₂ 0 specific heat data	. 70
19.	LiCuCl ₃ °2H ₂ 0 phase boundaries	. 71

Figur	re		P	age
20.	LiCuCl ₃ ·2H ₂ 0 angular dependence of critical field	•		72
21.	LiCuCl ₃ ·2H ₂ 0 fit to AF-P boundary	•	•	74
22.	LiCuCl ₃ ·2H ₂ 0 log-log plots for AF-P boundary	•	•	77
23.	KMnCl ₃ ·2H ₂ 0 crystal with rotation planes	•	•	82
24.	KMnCl ₃ ·2H ₂ 0 plane 1 isentropic rotations - twin	•	•	83
25.	KMnCl ₃ ·2H ₂ 0 plane 1 isentropic rotation - twin	•	•	84
26.	KMnCl ₃ ·2H ₂ 0 plane 2 isentropic rotations - twin	•	•	85
27.	KMnCl ₃ ·2H ₂ 0 plane l isentropic rotation - single	•	•	87
28.	KMnCl ₃ ·2H ₂ 0 plane l isentropic rotations - single	•	•	88
29.	KMnCl ₃ ·2H ₂ 0 plane 2 isentropic rotations - single	•		89
30.	KMnCl ₃ ·2H ₂ 0 plane 3 isentropic rotations - single	•	•	90
31.	KMnCl ₃ ·2H ₂ 0 plane 4 isentropic rotations - single	•	•	91
32.	KMnCl ₃ ·2H ₂ 0 plane 4 isentropic rotations - single	•	•	92
33.	KMnCl ₃ ·2H ₂ 0 phase boundaries	•	•	93
	KMnCl ₃ ·2H ₂ 0 isentropic magnetizations			95
35.	KMnCl ₃ ·2H ₂ 0 critical field angular dependence - single	•	•	96

Figure		Page
36.	${\rm KMnCl_3^{ \circ}2H_2^{ }0}$ plane 1 critical field angular dependence and rotation minima - twin .	97
37.	KMnCl ₃ ·2H ₂ 0 plane 2 critical field angular dependence and rotation minima - twin	98
38.	KMnCl ₃ ·2H ₂ 0 specific heat data - twin	100
39.	KMnCl ₃ ·2H ₂ 0 specific heat data - twin	101
40.	KMnCl ₃ ·2H ₂ 0 critical field best angle and	
	rotation extrema - single	102
41.	KMnCl ₃ ·2H ₂ 0 isentropic magnetizations	106

INTRODUCTION

The purpose of this study is to further develop the adiabatic method of studying antiferromagnets and to investigate some new crystals having the spin flop property. The unusual properties of KMnCl₃·2H₂O necessitated using some improved methods to investigate the phase boundaries. The use of a 21 kG magnet with a motor driven rotating base, a linear sweep circuit for changing the magnetic field, and a digital gaussmeter made data taking more precise. This enabled one to record small temperature changes by observing the output on a linear chart recorder.

Since the spins of both of the crystals studied were paired into dimers, modified molecular field theories were used to account for the spin interactions both within a dimer and between dimers. One could then estimate the exchange and anisotropy fields from the results.

The results for LiCuCl₃·2H₂O indicated that the spins flop 90° in the AC plane. Since KMnCl₃·2H₂O has an unusual number of phase boundaries, it appeared that the spins could flop 180° (at least at O°K), and an eight sublattice Ising model was used in the analysis.

I. GENERAL THEORY

A. Models for Antiferromagnetism

Several models have been introduced to explain the exchange interaction which leads to antiferromagnetism. The Heisenberg model uses an isotropic interaction between a spin, \underline{S}_i , and its neighboring spins, \underline{S}_j . The interaction potential energy of atom i is,

$$V_{i} = -2J\underline{s}_{i} \cdot (\Sigma_{j} \underline{s}_{j}), \qquad (1.1)$$

where the exchange integral, J, is negative for antiferromagnets.

The Ising model represents a very anisotropic case since it assumes that the interaction is between spin components in only one direction. Then the interaction potential for atom i is,

$$v_{i} = -2JS_{i_{z}} \Sigma_{j}S_{j_{z}}. \qquad (1.2)$$

The often used Weiss molecular field approximation expresses the spin interaction in terms of an exchange field, H_E . The z neighboring spins are represented by their statistical average, $\langle \underline{S}_i \rangle$,

$$V_{i} = -2zJ\underline{S}_{i} \cdot \langle \underline{S}_{j} \rangle \cdot \tag{1.3}$$

This can also be expressed as,

$$V_{i} = \underline{\mu}_{i} \cdot \underline{H}_{E}, \qquad (1.4)$$

where $\underline{\mu}_{i} = -g\mu_{B}\underline{S}_{i}$, and the exchange field is thus defined as,

$$H_E = 2z|J|\underline{\mu}_j/(g^2\mu_B^2) = 2z|J|\underline{M}_j/(Ng^2\mu_B^2)$$
 . (1.5)

Its magnitude at T = 0 is given by

$$H_E = 2z|J|M_O / (Ng^2 \mu_B^2),$$
 (1.6)

where N is the density of spins per sublattice, \underline{M}_j is the magnetization of the j sublattice, and \underline{M}_O is the saturation sublattice magnetization.

B. The Anisotropy Field

The anistropy energy for a uniaxial antiferromagnet may be expressed as, $^{\mbox{\scriptsize l}}$

$$E_{K} = -(1/2)K(\cos^{2}\theta_{i} + \cos^{2}\theta_{j}),$$
 (1.7)

where K is the anisotropy energy per unit volume and θ_i and θ_j are the angles that the sublattice magnetization vectors, \underline{M}_i and \underline{M}_j , make with the easy axis. Differentiating,

$$dE_{K} = K(\sin\theta_{i} \cos\theta_{j} d\theta_{i} + \sin\theta_{j} \cos\theta_{i} d\theta_{j}). \quad (1.8)$$

One can define anisotropy fields, H_{A_i} and H_{A_j} , by

$$E_{K} = -H_{A_{\dot{i}}} \quad M_{\dot{i}} \cos \theta_{\dot{i}} - H_{A_{\dot{j}}} \quad M_{\dot{j}} \cos \theta_{\dot{j}}. \tag{1.9}$$

If one considers that M_{i} and M_{j} are equal at zero applied field and represents them by M_{O} , then differentiating,

$$dE_{K} = (H_{A_{i}} \sin \theta_{i} d\theta_{i} + H_{A_{j}} \sin \theta_{j} d\theta_{j}) M_{o}. \qquad (1.10)$$

Comparing this with 1.8, then

$$H_{A_{i}} = K \cos \theta_{i} / M_{o}, H_{A_{j}} = K \cos \theta_{j} / M_{o}.$$
 (1.11)

For small θ_{i} and θ_{j} , a general anisotropy field can be expressed as,

$$H_{\lambda} = K / M_{\Omega}.$$
 (1.12)

C. Spin Flopping

The change of the thermodynamic potential is found by integrating

$$d\Phi = -S dT + V dP - M dH. \qquad (1.13)$$

With the external field, H, parallel to the easy axis in the antiferromagnetic (AF) state,

$$\Phi_{AF}(H) = -\int_{0}^{H} M(H') dH' = -\frac{1}{2} \chi_{\parallel} H^{2},$$
 (1.14)

assuming that the parallel susceptibility is independent of the external field. With the field applied parallel to the easy axis but with the spins flopped 90° to the easy axis (SF state), there is an anisotropy energy per unit volume, K, such that

$$\Phi_{SF}(H) = K - \frac{1}{2} \chi_{SF} H^2.$$
 (1.15)

If the anisotropy energy is very small compared to the exchange energy, then $\chi_{\rm SF}\!\approx\!\chi_{_{\|}}$. Then,

$$\Phi_{SF}(H) = K - \frac{1}{2} \chi_{\perp} H^2.$$
 (1.16)

The critical field for the AF-SF boundary can be found by equating these two potentials; then

$$H_{AF-SF} = [2K / (\chi_{\perp} - \chi_{\parallel})]^{1/2}.$$
 (1.17)

A slight error is introduced by assuming that χ_{\parallel} is independent of field, since the molecular field approximation shows that χ_{\parallel} increases with H as χ_{\perp} is unchanged. The low field values for χ_{\parallel} and χ_{\perp} are usually used, so that the calculation of H_{AF-SF} may then be slightly different from the experimental value.

The value of the critical field at T=0 can be expressed in terms of the anisotropy and exchange fields. Starting with the perpendicular susceptibility, l

$$\chi_{\perp} = 1 / (\lambda + K / 2 M_{\odot}^2),$$
 (1.18)

where λ is the molecular field constant for nearest neighbor interaction (1.6). Using H_A = K /M_O (eqn. 1.12),

$$\chi_{\parallel} = 2 M_{O} / (2H_{E} + H_{A}),$$
 (1.19)

and
$$\chi_{L} (2 H_E + H_A) K / M_O = 2 K.$$
 (1.20)

Substituting into 1.17,

$$H_{AF-SF} = [(2 H_E H_A + H_A^2) / (1 - \chi_{\parallel}/\chi_{\perp})]^{1/2},$$
(1.21)

or at T = 0,

$$H_{AF-SF}(0) = (2 H_E H_A + H_A^2)^{1/2}.$$
 (1.22)

To calculate the SF-P boundary field for a two sublattice model at T = 0, first evaluate the exchange, magnetic, and anisotropy energies of spins \underline{S}_i and \underline{S}_j , which are from different sublattices. Using 1.1 and 1.9 and summing over the z nearest neighbors, the spin energy is,

$$E(0) = -2 J \left(\underline{\underline{s}}_{i} \cdot \underline{\underline{s}}_{k} + \underline{\underline{s}}_{j} \cdot \underline{\underline{s}}_{1} \right)$$

$$- g\mu_{B} \left[\left(\underline{\underline{s}}_{i} + \underline{\underline{s}}_{j} \right) \cdot \underline{\underline{H}} + |\underline{\underline{s}}_{i} \cdot \underline{\underline{H}}_{A}| + |\underline{\underline{s}}_{j} \cdot \underline{\underline{H}}_{A}| \right].$$

$$(1.23)$$

The anistropy energy is expressed in terms of a field which is parallel to the easy axis.

Just above the AF-SF boundary, the spins are flopped, perpendicular to the easy axis and antiparallel to each other. Thus,

$$E(0)_{AF-SF} = 4 z J S^2.$$
 (1.24)

In the paramagnetic region, the spins are parallel to the external field, and

$$E(0)_{p} = -4 z J S^{2} - 2 g \mu_{B} S (H + H_{A}).$$
 (1.25)

Thus the field, H_{SF-P} , needed to change the spins from the perpendicular (SF) to the parallel (P) orientation is found by equating the energies in 1.24 and 1.25. Then,

$$H(0)_{SF-P} = - (4 z J S / g \mu_B) - H_A.$$
 (1.26)

Using 1.6 and the fact that J is negative,

$$H(0)_{SF-P} = 2 H_E - H_A.$$
 (1.27)

D. Observing Spin Flop Boundaries

As the external field is changed adiabatically, the temperature variation can be calculated as, ²

$$(dT/dH) = (\partial T/\partial H)_{S} = \frac{-(\partial S/\partial H)_{T}}{(\partial S/\partial T)_{H}}, \qquad (1.28)$$

where S is the entropy. Using the Maxwell relation

$$(\partial S/\partial H)_{T} = (\partial M/\partial T)_{H}, \qquad (1.29)$$

and
$$T (\partial S/\partial T)_{H} = C_{H}(T,H),$$
 (1.30)

where $C_{_{\mbox{\scriptsize H}}}$ is the constant field specific heat, then 1.28 is

$$(dT/dH) = -(T/C_H)(\partial M/\partial T)_H, \qquad (1.31)$$

or
$$(dT/dH) = - (T H/C_H) (\partial \chi/\partial T)_H$$
. (1.32)

In the antiferromagnetic state with $\chi = \chi_{||}$ and $(\partial \chi/\partial T) > 0$, (dT/dH) is negative. In the spin flop state with $\chi = \chi_{||}$ and $(\partial \chi/\partial T) = 0$, $(\partial T/\partial H) = 0$. Thus with an adiabatically increasing field aligned along the easy axis, the sample temperature should decrease until the spins flop and then should remain relatively constant.

It can be shown² that an adiabatic rotation should show a minimum in the AF state when the field is along the easy axis. Also, if the spins flop in the plane of rotation, there should be a relative maximum in the SF state at the easy axis position. If the spins flop perpendicular to the plane of rotation, there should be no temperature change on rotating near the easy axis for fields slightly above the AF-SF boundary. There the spins have almost no component along the easy axis or in the plane of rotation. Thus there is no change in the magnetic energy on rotating, as long as the spins remain flopped.

E. Observing Paramagnetic Boundaries

The AF-P and SF-P transitions are of second order. They can be observed by finding the discontinuity in the specific heat as a function of temperature in a constant field. Sometimes an isentrope can be used to denote the crossing of the paramagnetic boundary. Schelling and Friedberg noticed for MnBr₂·4H₂O that the intersection of

the isentrope with the AF-P phase boundary coincides with an inflection point in the isentrope.

It can be shown 4 that the isentropes cross the paramagnetic boundaries tangentially. If $S_{\rm b}({\rm H})$ is the entropy on the AF-P boundary, the entropy can be represented by a new variable,

$$s = S - S_b(H)$$
. (1.33)

Taking partial derivatives,

$$(\partial/\partial H)_{S} = (\partial/\partial H)_{S} - (dS_{b}(H)/dH)(\partial/\partial S)_{H}.$$
 (1.34)

Then,

$$(\partial T/\partial H)_{s} = (\partial T/\partial H)_{s} + (ds_{b}(H)/dH)(\partial T/\partial s)_{H}.$$
 (1.35)

From 1.30, $(\partial T/\partial S)_H = T/C_H$, and if the specific heat, C_H , diverges at the phase boundary, then the last term of 1.35 vanishes as s approaches zero. Then,

$$\lim_{s \to 0} (\partial T/\partial H)_{S} = (\partial T/\partial H)_{b}, \qquad (1.36)$$

where b refers to differentiation along the phase boundary.

Thus an isentrope near the boundary has the slope of the boundary. Under perfectly adiabatic conditions, the isentrope would continue along the boundary and would not cross it. However, background temperature effects in our experiments caused the isentrope to cross the boundary, and an inflection point was observed.

F. Demagnetization Corrections

The field, H', inside a sample is different from the applied field, H, due to the magnetization of the sample;

$$\underline{\mathbf{H}}' = \underline{\mathbf{H}} - \underline{\mathbf{D}} \underline{\mathbf{M}} , \qquad (1.37)$$

where $\underline{\underline{D}}$ is the tensor demagnetizing factor. A sphere has the lowest factor, a scalar $4\pi/3$. It would be difficult to shape the samples into spheres and then align them properly or to make demagnetization calculations for their odd shapes.

These corrections might be significant in the region near T_N where the magnetization is changing rapidly with temperature. In particular, the slopes of the isentropes are field dependent (1.32) and might be affected in this region. Since specific heat measurements were used to find most of the boundaries near T_N , the corrections were not used. All of the fields measured may be slightly higher than the actual field inside the crystal, especially in the low temperature region where \underline{M} approaches its saturation value.

II. LiCuCl₃·2H₂O THEORY

For LiCuCl₃·2H₂O, it is proposed that the copper ions are arranged in pairs with their spins parallel in each such dimer.⁵ The spins of the dimer are then antiparallel to those of the four nearest neighbor dimers (see Fig. 1). This model could be represented by an effective molecular field (in addition to the applied field, H) which represented the interaction between the spins of the (+) and (-) sublattices. Following Heller, one may write,

$$\underline{\mathbf{H}}_{\mathrm{E}} \ + = -\underline{\mathbf{a}} \cdot \underline{\mathbf{M}}_{\mp} - \underline{\mathbf{c}} \cdot \underline{\mathbf{M}}_{\pm} \ . \tag{2.1}$$

The tensor, $\underline{\underline{a}}$, corresponds to the antiferromagnetic exchange interaction between spins on different sublattices. The tensor, $\underline{\underline{c}}$, refers to the ferromagnetic exchange interaction within a sublattice, and $\underline{\underline{M}}$ refers to the magnetization on respective sublattices.

The anisotropy is included in these tensor coupling constants, and the contribution of the anisotropy to the molecular field is assumed to be a linear function of the sublattice magnetization. It is assumed that $\underline{\underline{a}}$ and $\underline{\underline{c}}$ have tetragonal symmetry about the preferred axis with values a $\underline{\underline{a}}$ and $\underline{\underline{c}}$ along the axis and \underline{a}_p and \underline{c}_p perpendicular to the axis.

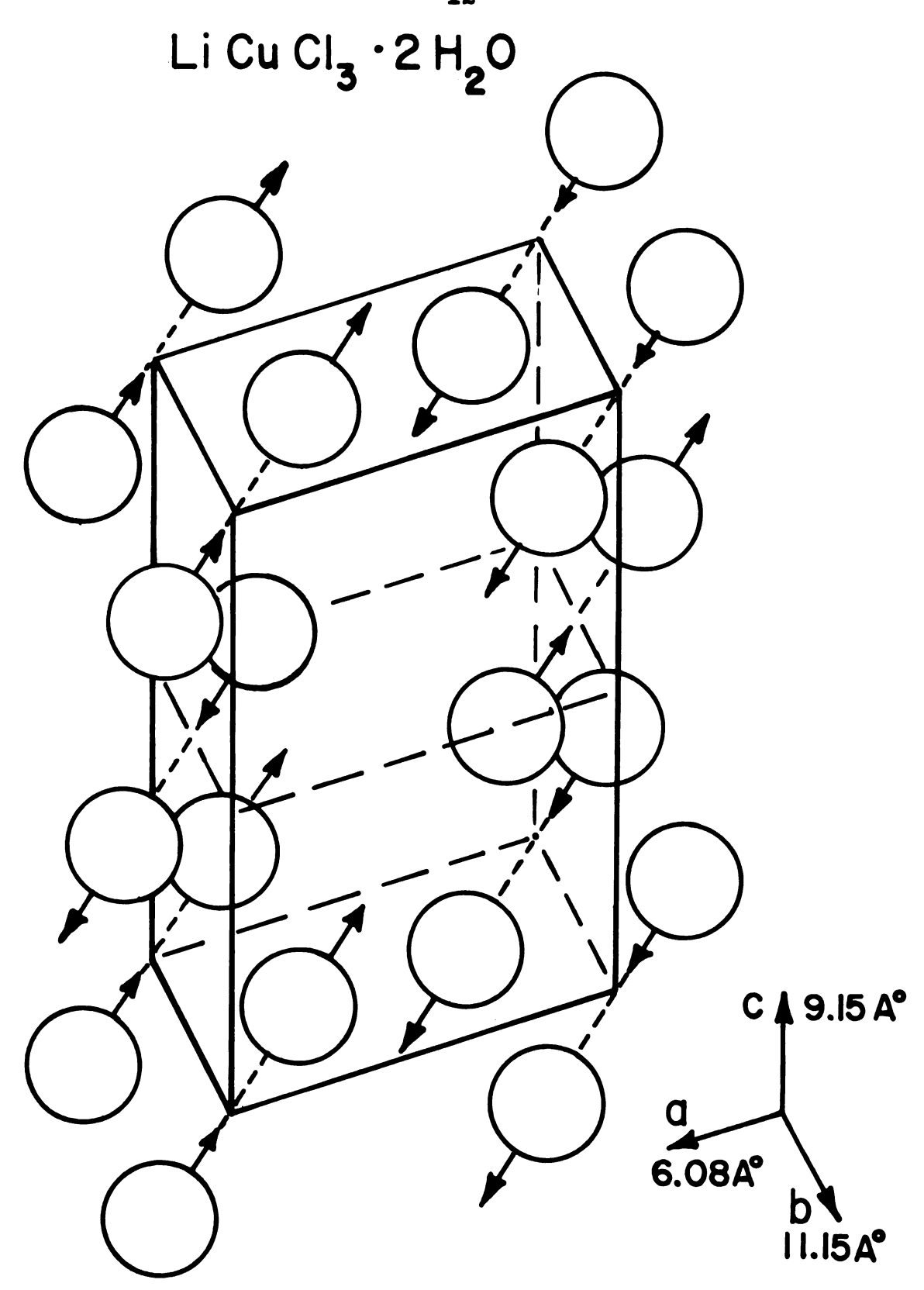


Figure 1. LiCuCl₃·2H₂O spin arrangement.

For each sublattice there are N spins, S, per unit volume, each with magnetic moment $Sg\mu_B$ where μ_B is the Bohr magneton and $g \cong 2$, as determined by Date. 7 With an applied field, H,

$$\underline{M}_{\pm} = \underline{M}_{oo} \, \underline{B}_{S} (|\underline{H} - \underline{\underline{a}} \cdot \underline{M}_{\pm} - \underline{\underline{c}} \cdot \underline{M}_{+} | \underline{Sg} \mu_{B} / \underline{k} \underline{T}), \quad (2.2)$$

where B_S is the Brillouin function, and

$$M_{OO} = NSg\mu_{B}$$
 (2.3)

is the saturated sublattice magnetization. It is also required that

$$\underline{\underline{M}}_{\pm}$$
 be parallel to $(\underline{\underline{H}} - \underline{\underline{a}} \cdot \underline{\underline{M}}_{\pm} - \underline{\underline{c}} \cdot \underline{\underline{M}}_{\pm})$. (2.4)

The reduced paramagnetic and antiferromagnetic parts of the magnetization are defined as respectively

$$\underline{P} = (\underline{M}_{+} + \underline{M}_{-})/2M_{OO}$$
 (2.5)

$$\underline{A} = (\underline{M}_{\perp} - \underline{M}_{\perp})/2\underline{M}_{00}. \tag{2.6}$$

The assumption that the contribution of the anisotropy to the molecular field is linear in the magnetization is not necessary for the cases with the field parallel or perpendicular to the easy axis. For a parallel field, the perpendicular components of \underline{M}_+ and \underline{M}_- are zero, and thus a_p and c_p are not used.

If one assumes this linearity for the case of a perpendicular field, then by equation 2.4,

$$M_{+||} \sim M_{+||} (a_{||} - c_{||}), \text{ and } (2.7)$$

$$M_{+p} \sim M_{+p} (-a_p - c_p) + H,$$
 (2.8)

since $M_p = M_+$ and $M_- = M_+$ by symmetry. By looking at 2.7 and 2.8, it can be seen that the contribution of anisotropy to the molecular field must be linear in the magnetization. Otherwise 2.4 would not hold.

Using the inverse Brillouin function, a new function is defined:

$$G(x) = B_S^{-1}(x)(S + 1)/3S.$$
 (2.9)

It can be shown that

$$G'(0) = 1$$
, $G''(0) = 0$, and
$$G'''(0) = -B_S'''(0)/[B_S'(0)]^3 = (27/15)(2S^2 + 2S + 1)/(S + 1)^2.$$
(2.10)

For a vector, V, G(V) is defined as,

$$G(\underline{V}) = \underline{V} G(|\underline{V}|)/|\underline{V}|. \tag{2.11}$$

Using the unit vectors $\frac{1}{\|}$ and $\frac{1}{p}$ which are respectively parallel and perpendicular to the preferred axis,

$$\underline{v} = v_{||} \underline{1}_{||} + v_{p}\underline{1}_{p}$$
 (2.12)

Using 2.2, 2.5, 2.6, and 2.11,

$$G(\underline{P} + \underline{A}) - G(\underline{P} - \underline{A}) = (\underline{1}_{+}B_{S}^{-1}|\underline{P} + \underline{A}| - \underline{1}_{-}B_{S}^{-1}|\underline{P} - \underline{A}|) (S+1)/3S,$$
(2.13)

where $\underline{1}_{+} = \underline{M}_{+}/|\underline{M}_{+}|$, and $\underline{1}_{-} = \underline{M}_{-}/|\underline{M}_{-}|$. For purposes of simplification, write \underline{K} as,

$$\underline{K} = [G(\underline{P} + \underline{A}) - G(\underline{P} - \underline{A})](3kT)/[g\mu_B(S+1)] \qquad (2.14)$$

$$= \underline{1}_{+} |\underline{H} - \underline{\underline{a}} \cdot \underline{M}_{-} - \underline{\underline{c}} \cdot \underline{M}_{+} | - \underline{1}_{-} |\underline{H} - \underline{\underline{a}} \cdot \underline{M}_{+} - \underline{\underline{c}} \cdot \underline{M}_{-} |.$$

The plane of spins is defined by the unit vectors $\frac{1}{||}$ and $\frac{1}{||}$ as shown in Fig. 2.

From 2.4, the only non-zero components of $(\underline{H} - \underline{\underline{a}} \cdot \underline{M}_{-} - \underline{\underline{c}} \cdot \underline{M}_{+})$ are those parallel to $\underline{1}_{+}$. Then from 2.14,

$$\underline{K} = \underline{1}_{+} \left[\cos \theta_{+}^{(H)} - a \|^{M}_{-} - c \|^{M}_{+} \right] + \sin \theta_{+}^{(H)} - a_{p}^{M}_{-} - c_{p}^{M}_{+} \right]
+ \underline{1}_{-} \left[\cos \theta_{-}^{(H)} - a \|^{M}_{+} - c \|^{M}_{-} \right] + \sin \theta_{-}^{(-H)} + a_{p}^{M}_{+} + c_{p}^{M}_{-} \right].$$
(2.15)

Parallel and perpendicular components of \underline{K} are taken using,

$$\frac{1}{+} = \cos \theta_{+} \frac{1}{||} + \sin \theta_{+} \frac{1}{||}$$

$$\frac{1}{-} = -\cos \theta_{-} \frac{1}{||} + \sin \theta_{-} \frac{1}{||}$$

Then,

$$K_{\parallel} = \cos^{2} \theta_{+} (H_{\parallel}^{-} a_{\parallel}^{M}_{-\parallel}^{-} c_{\parallel}^{M}_{+\parallel}^{+}) + \cos \theta_{+} \sin \theta_{+} (H_{p}^{-} a_{p}^{M}_{-p}^{-} c_{p}^{M}_{+p}^{+})$$

$$- \cos^{2} \theta_{-} (H_{\parallel}^{-} a_{\parallel}^{M}_{+\parallel}^{-} c_{\parallel}^{M}_{-\parallel}^{-}) - \cos \theta_{-} \sin \theta_{-} (-H_{p}^{+} a_{p}^{M}_{+p}^{+} c_{p}^{M}_{-p}^{-}),$$

$$(2.17)$$

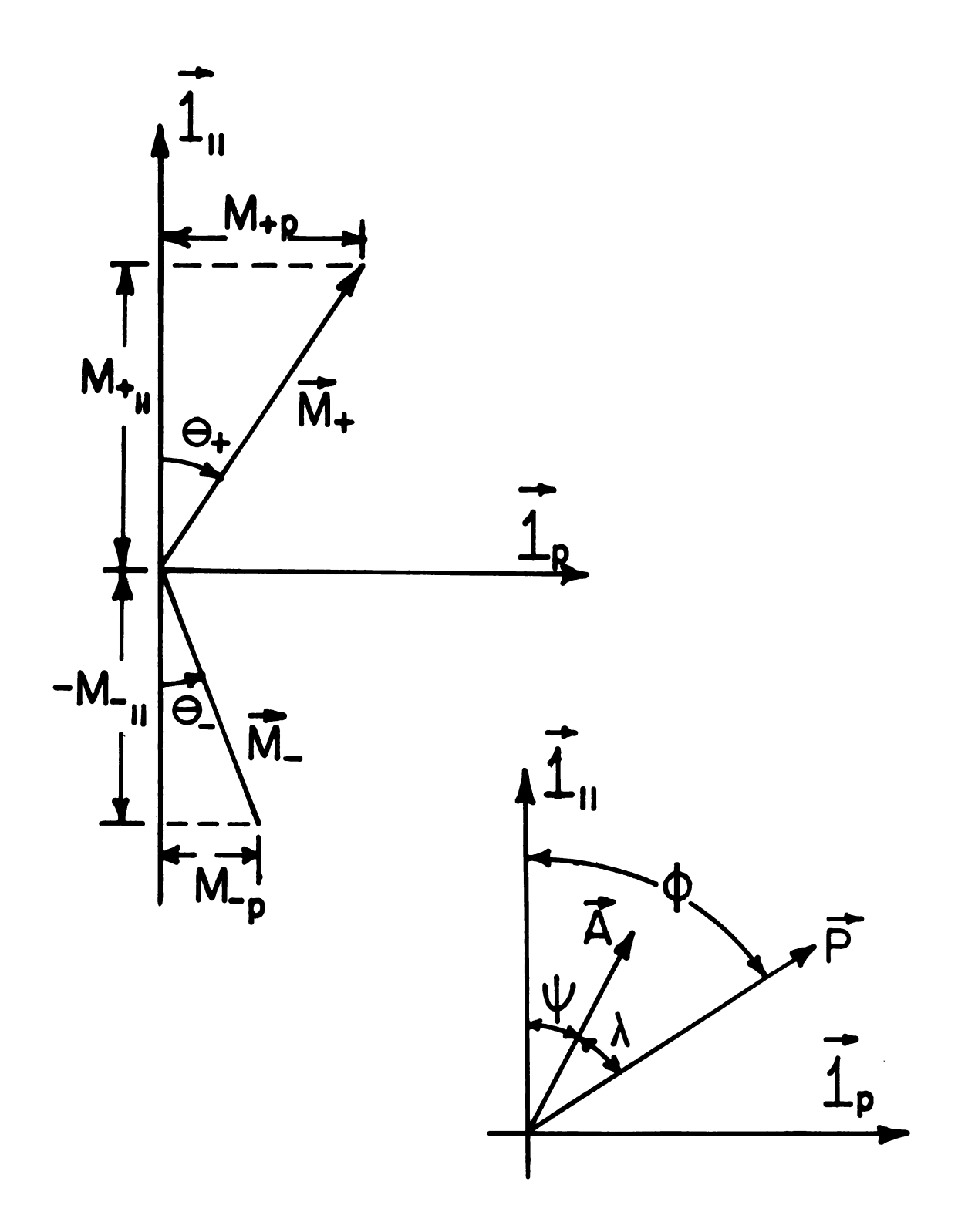


Figure 2. Definition of angles and vectors.

and,

$$K_{p} = \cos \theta_{+} \sin \theta_{+} (H_{\parallel} - a_{\parallel} M_{-\parallel} - c_{\parallel} M_{+\parallel})$$

$$+ \sin^{2} \theta_{+} (H_{p} - a_{p} M_{-p} - c_{p} M_{+p})$$

$$+ \cos \theta_{-} \sin \theta_{-} (H_{\parallel} - a_{\parallel} M_{+\parallel} - c_{\parallel} M_{-\parallel})$$

$$+ \sin^{2} \theta_{-} (-H_{p} + a_{p} M_{+p} + c_{p} M_{-p})$$
(2.18)

Using 2.4 it is found that,

$$(H_{p} - a_{p}M_{-p} - c_{p}M_{+p}) = \tan \theta_{+} (H_{||} - a_{||}M_{-||} - c_{||}M_{+||})$$

$$(H_{p} - a_{p}M_{+p} - a_{p}M_{-p}) = -\tan \theta_{-} (H_{||} - a_{||}M_{+||} - c_{||}M_{-||}).$$

$$(2.19)$$

Finally,

$$K_{\parallel} = (\cos^{2}\theta_{+} + \sin^{2}\theta_{+}) (H_{\parallel} - a_{\parallel} M_{-\parallel} - c_{\parallel} M_{+\parallel}) - (\cos^{2}\theta_{-} + \sin^{2}\theta_{-}) (H_{\parallel} - a_{\parallel} M_{+\parallel} - c_{\parallel} M_{-\parallel}) = (a_{\parallel} - c_{\parallel}) (M_{+\parallel} - M_{-\parallel}).$$
 (2.20)

Similarly,

$$K_{p} = (\cos^{2}\theta_{+} + \sin^{2}\theta_{+}) (H_{p} - a_{p}M_{-p} - c_{p}M_{+p})$$

$$- (\cos^{2}\theta_{-} + \sin^{2}\theta_{-}) (H_{p} - a_{p}M_{+p} - c_{p}M_{-p})$$

$$= (a_{p} - c_{p}) (M_{+p} - M_{-p}). \qquad (2.21)$$

Then returning to 2.14,

$$\frac{1}{2} [G(P + A) - G(P - A)]$$

$$= \frac{(s + 1)g\mu_{B}}{6kT} [(a|| - c||) (M + M - M)] + (a_{P} - c_{P}) (M + M - M)]$$

$$= \frac{NS(S + 1)g^{2}\mu_{B}^{2} (a|| - c||)}{3kT} \left(\frac{M + M - M}{2M_{OO}} + \left(\frac{a_{P} - c_{P}}{a|| - c||}\right) \frac{M + M - M}{2M_{OO}}\right)$$

$$(2.22)$$

since $M_{OO} = Ng\mu_B s$. To simplify the constant coefficient, consider the case with \underline{H} along the preferred axis giving $M_{+p} = 0 = M_{-p}$. Then the right side of 2.22 is,

$$\frac{\text{NS}(S+1)g^{2}\mu_{B}^{2}}{3kT} \qquad (a_{\parallel}^{-c}\parallel) (\underline{M}_{+\parallel}^{-} - \underline{M}_{\parallel}^{-})/2M_{00}. \qquad (2.23)$$

Using 2.10, G(A) can be expanded in a series;

$$G(A) = A + (A^3/6) G'''(0) + \dots$$
 (2.24)

As T approaches Tn from below (assuming a small field, \underline{H}), then the left side of 2.22 may be expanded to yield:

$$[G(\underline{P} + \underline{A}) - G(\underline{P} - \underline{A})]/2 = (\underline{M} + |-\underline{M}|)/2M_{00}$$
 (2.25)

since \underline{M}_{+} and \underline{M}_{-} are very small in this case. For 2.23 and 2.25 to be equivalent,

$$T_{N} = (a_{\parallel} - c_{\parallel}) Ng^{2} \mu_{B}^{2} S(S + 1)/3k.$$
 (2.26)

Then 2.22 is finally,

$$[G(\underline{P} + \underline{A}) - G(\underline{P} - \underline{A})]/2 = (\underline{A}_{||} + Q\underline{A}_{||})/t, \qquad (2.27)$$

where
$$t = T/T_n$$
 and $Q = \left(\frac{a_p - c_p}{a_{||} - c_{||}}\right)$.

An expression can similarly be obtained for $[G(\underline{P} + \underline{A}) + G(\underline{P} - \underline{A})]$ as done for equation 2.14:

$$\underline{L} = [G(\underline{P} + \underline{A}) + G(\underline{P} - \underline{A})] 3kT/(g\mu_B(S + 1))$$

$$= \underline{1}_+ |\underline{H} - \underline{\underline{a}} \cdot \underline{M}_- - \underline{\underline{c}} \cdot \underline{M}_+| + \underline{1}_- |\underline{H} - \underline{\underline{a}} \cdot \underline{M}_+ - \underline{\underline{c}} \cdot \underline{M}_-|.$$
 (2.28)

Proceeding as was done for 2.16,

$$\underline{L} = \frac{1}{+} \left[\cos \theta_{+} (H_{\parallel} - a_{\parallel} M_{-\parallel} - c_{\parallel} M_{+\parallel}) + \sin \theta_{+} (H_{p} - a_{p} M_{-p} - c_{p} M_{+p}) \right]$$

$$- \underline{1}_{-} \left[\cos \theta_{-} (H_{\parallel} - a_{\parallel} M_{+\parallel} - c_{\parallel} M_{-\parallel}) + \sin \theta_{-} (-H_{p} + a_{p} M_{+p} + c_{p} M_{-p}) \right].$$
(2.29)

Then, as was calculated for 2.18,

$$L_{\parallel} = \cos^{2}\theta_{+} (H_{\parallel} - a_{\parallel} M_{-\parallel} - c_{\parallel} M_{+\parallel}) + \cos\theta_{+} \sin\theta_{+} (H_{p} - a_{p} M_{-p} - c_{p} M_{+p})$$

$$+ \cos^{2}\theta_{-} (H_{\parallel} - a_{\parallel} M_{+\parallel} - c_{\parallel} M_{-\parallel}) + \cos\theta_{-} \sin\theta_{-} (-H_{p} + a_{p} M_{+p} + c_{p} M_{-p})$$

$$= 2H_{\parallel} - (a_{\parallel} + c_{\parallel}) (M_{+\parallel} + M_{-\parallel}). \qquad (2.30)$$

Also,

$$L_{p} = \cos^{\theta}_{+} \sin^{\theta}_{+} (H_{\parallel} - a_{\parallel} M_{-\parallel} - c_{\parallel} M_{+\parallel}) + \sin^{2}_{\theta}_{+} (H_{p} - a_{p} M_{-p} - c_{p} M_{+p})$$

$$- \cos^{\theta}_{-} \sin^{\theta}_{-} (H_{\parallel} - a_{\parallel} M_{+\parallel} - c_{\parallel} M_{-\parallel}) - \sin^{2}_{\theta}_{-} (-H_{p} + a_{p} M_{+p} + c_{p} M_{-p})$$

$$= 2H_{p} - (a_{p} + c_{p}) (M_{+p} + M_{-p}). \tag{2.31}$$

Thus, $[G(\underline{P}+\underline{A}) + G(\underline{P}-\underline{A})]/2 = \frac{(s+1)g\mu_{B}}{3kT} \left[\frac{1}{||} [H_{||}^{-}(a_{||}^{+}c_{||}^{-})(M_{+}^{+}H_{-}^{+})] \frac{Ng\mu_{B}S}{4M_{OO}}] + \frac{1}{||} [H_{p}^{-}(a_{p}^{+}c_{p}^{-})(M_{+}^{+}H_{-}^{+})] \frac{Ng\mu_{B}S}{4M_{OO}}] \right]$ $= \frac{1}{t} (\underline{F} - \underline{WP}_{||} - \underline{RWP}_{p}), \qquad (2.32)$

where

$$W = \frac{a_{\parallel} + c_{\parallel}}{a_{\parallel} - c_{\parallel}}, \quad R = \frac{a_{p} + c_{p}}{a_{\parallel} + c_{\parallel}}, \quad \text{and}$$

$$\underline{F} = \frac{g\mu_{B}(s+1)}{3kT_{N}} \quad \underline{H}.$$

Upon using the expansion 2.24, the left side of 2.32 is equal to \underline{P} for temperatures not too far below T_N (A<<1) and in moderate applied fields (P<<1). This gives,

$$\underline{P}_{\parallel} = \underline{F}_{\parallel} / (t+W), \underline{P}_{p} = \underline{F}_{p} / (t+RW).$$
 (2.33)

Since isotropic interactions predominate over anisotropic interactions, $a_p/a_{\parallel}^{\approx} 1^{\approx} c_p/c_{\parallel}$. Thus $R \approx 1$ and \underline{P} is proportional and parallel to \underline{F} for this case.

The bulk magnetization is,

$$\underline{\underline{M}}_{+}(\underline{T},\underline{\underline{H}}) + \underline{\underline{M}}_{-}(\underline{T},\underline{\underline{H}}) = \underline{\underline{X}}(\underline{T}) \cdot \underline{\underline{H}} \approx X_{\underline{N}}\underline{\underline{H}}$$
 (2.34)

where the tensor, $\frac{\chi}{z}$, is taken as a constant scalar, $\frac{\chi}{N}$, for our purposes. Then 2.34 may be rewritten as

$$\underline{P} = \chi_{N} \underline{H} / 2M_{OO}. \qquad (2.35)$$

The temperature dependence of \underline{A} is calculated from 2.27 by regarding P as a known quantity. Define

$$G_{\underline{D}}(\underline{A}) = [G(\underline{P} + \underline{A}) - G(\underline{P} - \underline{A})]/2 \qquad (2.36)$$

and expand according to 2.24.

$$G_{\underline{D}}(\underline{A}) = [(\underline{P}+\underline{A})-(\underline{P}-\underline{A})+(|\underline{P}+\underline{A}|^{2}(\underline{P}+\underline{A})-|\underline{P}-\underline{A}|^{2}(\underline{P}-\underline{A}))G'''(0)/6]/2$$

$$= \frac{1}{2} \left[(\underline{P}+\underline{A}) [1+(\underline{P}^{2}+\underline{A}^{2}+2\underline{P}\underline{A}\cos\lambda)G'''(0)/6] \right].$$

$$(\underline{P}-\underline{A}) [1+(\underline{P}^{2}+\underline{A}^{2}-2\underline{P}\underline{A}\cos\lambda)G'''(0)/6] \right].$$

Or,

$$G_{D}(\underline{A}) = \underline{A} [1 + (\underline{P}^{2} + \underline{A}^{2})G'''(0)/6] + \underline{P}(\underline{P} \cdot \underline{A})G'''(0)/3.$$
 (2.38)

where the angle, λ , is defined in Fig. 2.

Taking the components of 2.38 which are in the \underline{A} direction,

$$A \left[1 + (A^{2} + P^{2})G'''(0)/6 + P^{2} \cos^{2} \lambda G'''(0)/3\right]$$

$$= (A_{\parallel} \cos \psi + QA_{p} \sin \psi)/t$$

$$= \left[(1-\sin^{2} \psi) + Q\sin^{2} \psi\right]A/t, \qquad (2.39)$$

where the angle, ψ , is defined in Fig. 2. The components of 2.38 which are normal to the <u>A</u> direction are

$$P^{2}A \cos \lambda \sin \lambda G^{m}(0)/3 = AP^{2} \sin 2\lambda G^{m}(0)/6$$

$$= (-\sin \psi + \cos \psi QA_{p}) = (-A/t)(1-Q)\sin \psi \cos \psi. \tag{2.40}$$

If the applied field is weak enough so that,

$$P^2 G^{\text{IM}}(0)/6 << (1 - Q),$$
 (2.41)

then <u>A</u> is essentially parallel to $\frac{1}{||}$, i.e., $\psi \approx 0$. Then $(1-Q)\sin^2\psi << P^2(1+2\cos^2\lambda)G'''(0)/6$, and since A^2 is small compared to P^2 $(1+2\cos^2\lambda)$, equation 2.39 may be written with $\lambda \approx \phi$;

$$A[1 + P^{2}(1 + 2\cos^{2}\phi)G'''(0)/6] = A/t,$$
 (2.42)

where ϕ is defined in Fig. 2. From 2.10 and 2.35 this becomes,

$$A/t = A \left[1 + \frac{3(2S^2 + 2S + 1)}{40(s+1)^2 M_{QQ}^2} (1 + 2\cos^2\phi) \chi_N^2 H^2\right]. \quad (2.43)$$

For $T_N - T_N(H) \le T_N$, this becomes

$$T_{N}(H) = T_{N} \left[1 - \frac{3(2s^{2}+2s+1)}{40(s+1)^{2}} \left(\frac{\chi_{N}}{M_{OO}}\right)^{2} H^{2} (1+2cos^{2}\phi)\right].$$
 (2.44)

When the field, \underline{H} , is applied perpendicular to the preferred axis, \underline{M}_+ and \underline{M}_- have equal lengths, \underline{M}_0 , as they turn toward \underline{H} . Then equation 2.27 yields, (with $\theta_+ = \theta_-$)

$$G(M_{\circ}/M_{\circ\circ})(\underline{M}_{+}-\underline{M}_{-})/M_{\circ} = (\underline{M}_{+}-\underline{M}_{-})/(tM_{\circ\circ}),$$
 (2.45)

or
$$G(M_0/M_{00}) = M_0/(tM_{00})$$
 (2.46)

assuming $(\underline{M}_{+} - \underline{M}_{-}) \neq 0$. Since 2.46 is independent of $\underline{H}_{+}, \underline{M}_{+}$ and \underline{M}_{-} have a constant length as they turn toward \underline{H}_{-} .

In order to check the experimental results with 2.44, in particular, the phase boundary between the paramagnetic (P) and antiferromagnetic (AF) states, the following molecular field calculations will be used,

$$\chi_{N} = N_{t} g^{2} \mu_{B}^{2} s(s+1)/(6kT_{N}) = N_{t} g^{2} \mu_{B}^{2}/(4z_{1}J_{1})$$
 (2.47)

where N_t is the total number of spins per unit volume and $M_{OO} = N_t g \mu_B S/2$. Assuming a general form for T_N ,

$$T_{N} = (2s(s+1)/(3k)) \sum_{i} z_{i} |J_{i}|$$
 (2.48)

where J_1 and J_2 are the intersublattice and intrasublattice exchange interactions respectively, and z_1 refers to the number of nearest neighbors, then 2.44 becomes,

$$(T_{N}-T) = \frac{g^{2}\mu_{B}^{2}(z_{1}|J_{1}|+z_{2}|J_{2}|)(2s^{2}+2s+1)(1+2\cos^{2}\phi)H^{2}}{80k z_{1}^{2} J_{1}^{2} s(s+1)}, (2.49)$$

or,
$$(2s^{2}+2s+1) \left[1+\frac{z_{2}|J_{2}|}{z_{1}|J_{1}|}\right] g^{2}\mu_{B}^{2} H^{2} (1+\cos^{2}\phi)$$

$$(T_{N}-T) = \frac{120 k^{2} T_{N}}{(2.50)}$$

Assuming no intrasublattice interaction,

$$(T_N-T) = \frac{(2s^2+2s+1)g^2\mu_B^2H^2(1+2cos^2\phi)}{120 k^2T_N},$$
 (2.51)

where T_N is written in terms of $|J_1|$, or

$$(T_N-T) = \frac{g^2 \mu_B^2 (2s^2+2s+1) (1+2\cos^2\phi) H^2}{80 kz_1 |J_1| s (s+1)}$$
 (2.52)

III. KMnCl₃·2H₂O THEORY

A. Ising Model

To explain some of the results for the phase diagram of KMnCl₃·2H₂O which indicates five distinct magnetic phases and four boundaries at T = 0, an eight sublattice Ising model is introduced. An eight spin unit has two dimers 8 with all the spins antiparallel to those in its other two dimers (Figs. 3, 4). Oguchi has done an analysis using a four spin unit for CoCl₂·2H₂0. There are four different spin interactions assumed, with J_1 being the intradimer exchange interaction between spins 3.85 A° apart. The J₂, J₃, J₄ interactions are the average of the interactions between a spin and its two neighbor dimers with the interdimer separations being respectively 6.5 A°, 6.9 A°, and 7.4 A°. J_4 represents the short diagonal of a parallelogram whose long diagonal is 11.1 A°. These interactions are shown in Fig. 4 which depicts a plane of dimers. A dimer in this plane, which is parallel to the AB plane, is 9.91 A° (along the C axis) from the closest dimer in a neighboring plane.

It was not necessary to consider all the interactions between a spin and the individual spins of neighboring dimers. If this were done in the calculation

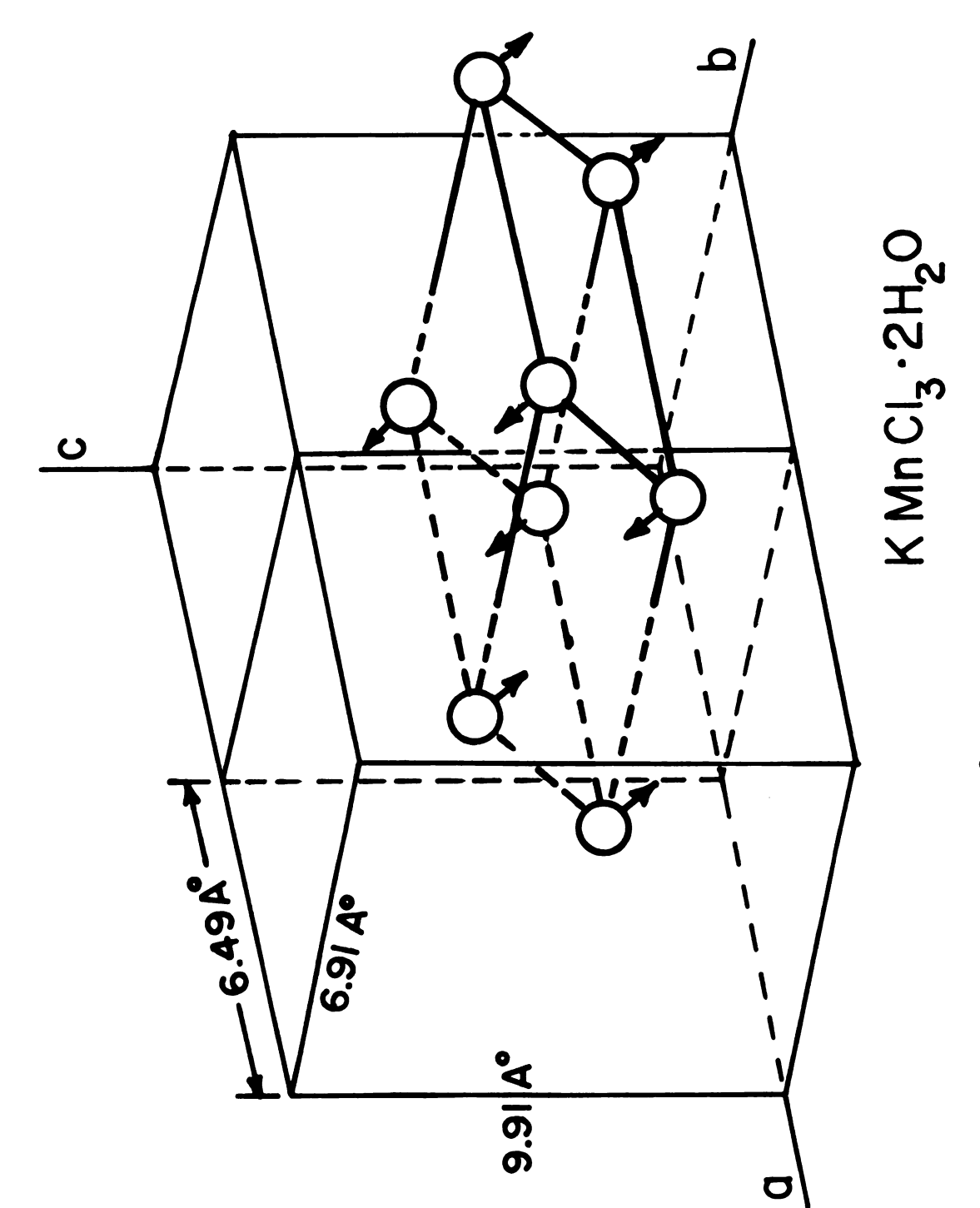


Figure 3. KMnCl₃·2H₂0 8 spin unit.

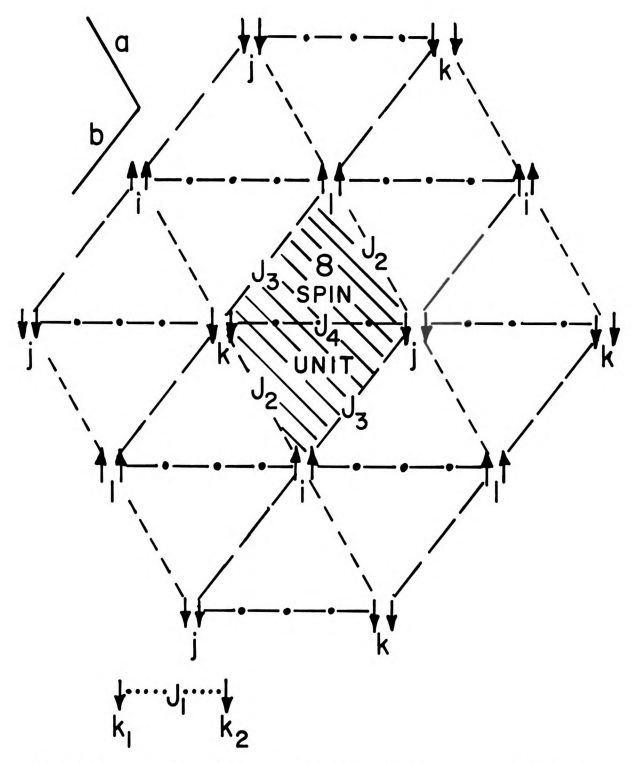


Figure 4. $\mathrm{KM_{n}C1_{3}^{\circ}2H_{2}O}$ two dimensional dimer arrangement.

below, the interactions from the two neighbor dimers would be coupled together and thus could be represented by a single interaction. However, the spin is usually closer to one neighbor dimer than another (Fig. 5a). Then each neighbor dimer would probably cause a different interaction, and thus the J value represents the average of the two interactions.

In summing up all the interactions in Fig. 4, the interactions between the eight spin unit and neighboring dimers are halved because only half of the interacting spins belong to the eight spin unit. In Fig. 5a, one can check whether the spins of a dimer (k_1, k_2) have similar total interactions. Considering a factor of 1/2 for interactions outside the unit (bounded by k_1 , k_2 , l_1 , l_2), one obtains similar totals, remembering that k_1 and k_1 ' are of the same sublattice and thus both are involved in the interaction. A similar figure for the k-j interaction gives the same result.

There is a Zeeman term in addition to the Ising spin interaction. For each of the boundary field values (Fig. 5b), the energies of the two bounding regions are set equal. The values of the exchange constants can thus be found from these four fields. $S_{il}^{\ z}$, the z component of S_{il} , is represented by il. As shown in Fig. 4, the sublattices are repeated through the crystal. The energy is then found from equation 1.2,

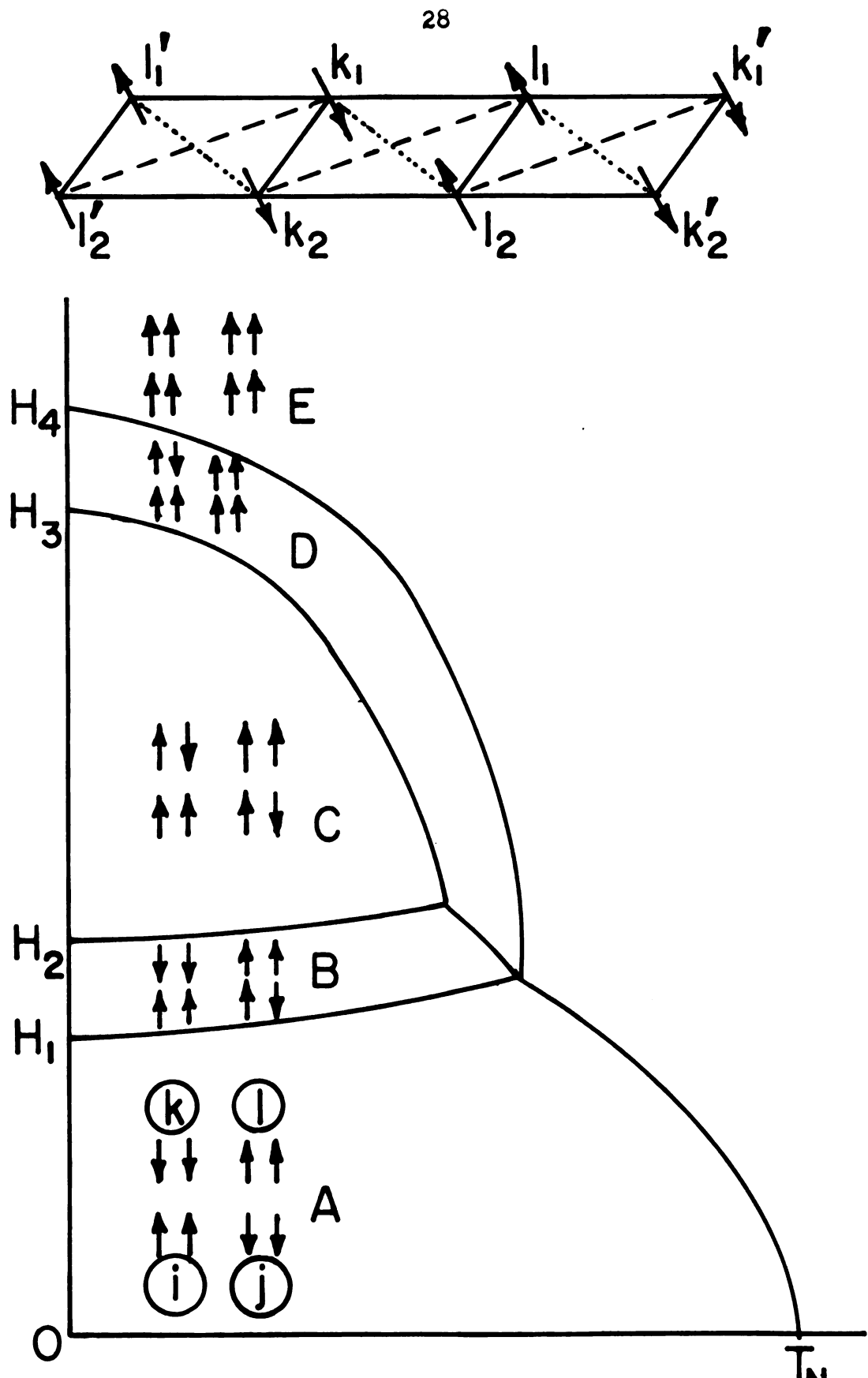


Figure 5. KM_nCl₃·2H₂O J₃ interaction in BC plane and Ising spin model.

$$\begin{split} \mathbf{E} &= -2 \ \mathbf{J_1} \ (\text{il i2} + \text{j1 j2} + \text{k1 k2} + \text{l1 l2}) \\ &- 4 \ \mathbf{J_2} [(\text{il + i2}) (\text{k1 + k2}) + (\text{j1 + j2}) (\text{l1 + l2})] \\ &- 4 \ \mathbf{J_3} [(\text{il + i2}) (\text{j1 + j2}) + (\text{l1 + l2}) (\text{k1 + k2})] \\ &- 4 \ \mathbf{J_4} [(\text{k1 + k2}) (\text{j1 + j2}) + (\text{l1 + l2}) (\text{i1 + i2})] \\ &- g \mu_{\text{B}} \ \text{H} \ (\text{il + i2 + j1 + j2 + k1 + k2 + l1 + l2}) \,. \end{split}$$

In the antiferromagnetic state (region A of Fig. 5b),

$$E_A = 8 S^2 (-J_1 + 4 J_2 + 4 J_3 - 4 J_4).$$
 (3.2)

For the four other phases,

$$E_B = 4 S^2 (-J_1 + 4 J_2 + 4 J_3 - 4 J_4) - 2 S g\mu_B H$$
 (3.3)
(jl changes sign)

$$E_C = -16 \text{ S}^2 \text{ J}_4 - 4 \text{ S } g\mu_B \text{ H, (kl changes sign)}$$
 (3.4)

$$E_D = 4 S^2 (-J_1 - 4 J_2 - 4 J_3 - 4 J_4) - 6 S g\mu_B H,$$
 (3.5)
(j2 changes sign)

$$E_E = -8 \text{ s}^2 (J_1 + 4 J_2 + 4 J_3 + 4 J_4) - 8 \text{ S } g\mu_B \text{ H.}$$
 (3.6)
(k2 changes sign)

Setting $E_A = E_B$ at their boundary field, H_1 ,

$$(2 J_1 - 8 J_2 - 8 J_3 + 8 J_4) = g\mu_R H_1/S.$$
 (3.7)

Similarly for $E_B = E_C$, $E_C = E_D$, and $E_D = E_E$,

$$(2 J_1 - 8 J_2 - 8 J_3) = g\mu_B H_2/S,$$
 (3.8)

$$(-2 J_1 - 8 J_2 - 8 J_3) = g\mu_B H_3/S$$
 (3.9)

$$(-2 J_1 - 8 J_2 - 8 J_3 - 8 J_4) = g\mu_B H_4/s.$$
 (3.10)

From equations 3.7, 3.8, 3.9, and 3.10,

$$J_4 = -g\mu_B (H_2 - H_1)/8 S = -g\mu_B (H_4 - H_3)/8S,$$
 (3.11)

From 3.8 and 3.9,

$$J_1 = -g\mu_B (H_3 - H_2)/4S.$$
 (3.12)

Using 3.11 and 3.12 in 3.7,

$$J_2 + J_3 = -g\mu_B (H_2 + H_3)/16 \text{ S.}$$
 (3.13)

The J_2 and J_3 interactions are coupled. It is interesting to note from 3.11 that

$$H_2 - H_1 = H_4 - H_3.$$
 (3.14)

If an exchange field is defined as $H_E = 2z|J|S/g\mu_B$, and since the number of neighboring dimers from Fig. 4 is $z_1 = 1$, $z_2 = z_3 = z_4 = 2$, then

$$H_{E1} = \frac{1}{2}(H_3 - H_2)$$
, $H_{E2} + H_{E3} = \frac{1}{4}(H_2 + H_3)$, $H_{E4} = \frac{1}{2}(H_2 - H_1)$. (3.15)

B. Dipolar Anisotropy

It is believed that an anisotropic dipole-dipole interaction could contribute significantly to the total anisotropy. Since each spin has only one nearest neighbor, there is no cancellation of dipole fields by symmetrically positioned neighbors. The Mn-Mn separation is only 3.85 A°, relatively short for manganese salts; and the interaction is proportional to $1/r^3$:

$$H_{d} = \underline{\mu}_{i} \cdot \underline{\mu}_{j} / (r_{ij})^{3} - 3(\underline{\mu}_{i} \cdot \underline{r}_{ij}) (\underline{\mu}_{j} \cdot \underline{r}_{ij}) / (r_{ij})^{5}. \quad (3.16)$$

The line joining the spins is \underline{r}_{ij} , and $\underline{\mu}_i = g\mu_B\underline{s}_i$ is the spin magnetic movement.

The principal contribution to the anisotropy is the spin-orbit interaction which results from the crystalline electric field quenching the spin-orbit degeneracy. A change in the magnitude of the dipolar anisotropy could shift the easy axis (total anisotropy direction) if they are not collinear. From equation 3.16, the lowest energy state is with μ_i and μ_j parallel to \underline{r}_{ij} , which is the dipolar anisotropy direction. For KMnCl₃·2H₂O, this direction is almost perpendicular to the easy axis, certainly not collinear.

Taking the nearest neighbor dipole interactions for the eight spin Ising model of Fig. 5b, the interaction changes as the phase boundaries are crossed. In the

antiferromagnetic state (A), the spins make equal angles (θ) of about 90° with \underline{r} ; thus $\cos^2\theta$ <<1. For regions A and E,

$$H_{dA} = H_{dE} = 2(2 - 6\cos^2\theta) \mu^2/r^3$$
 (3.17)

The other regions give,

$$H_{dB} = H_{dD} = (2 - 6 \cos^2 \theta) \mu^2 / r^3,$$
 (3.18)

$$H_{dC} = 0.$$
 (3.19)

If the Ising model is correct for this crystal, an easy axis shift in going from region A to B should be duplicated in going from B to C. Then there should be an equal but opposite shift going from C to D and from D to E. Thus regions A and E should have the same easy axis, and likewise for B and D.

C. The AF-P Perpendicular Boundary

If a crystal has uniaxial anisotropy, one can calculate an AF-P phase boundary for fields applied perpendicular to the easy axis. It is required that the spins on one sublattice, \underline{M}_1 , be parallel to their total effective field, \underline{H}_{eff_1} ; or

$$\underline{\mathbf{H}}_{\mathbf{eff}_{1}} \times \underline{\mathbf{M}}_{1} = 0, \tag{3.20}$$

where $\underline{H}_{eff_1} = \underline{H} - \underline{H}_{E}\underline{M}_2/\underline{M}_0$, and \underline{H}_{E} is given by equation 1.6.

The interaction from the uniaxial anisotropy field, \underline{H}_{AZ} , is assumed to be proportional to \underline{M}_1 . With the applied field, \underline{H}_{Y} , along the y axis toward which the spins rotate, and δ being the angle made with the z axis (which is the easy axis), 3.20 becomes

$$\begin{vmatrix}
\underline{i} & \underline{j} & \underline{k} \\
0 & (H_{y}^{-H_{E}M_{2}\sin\delta/M_{O}}) & (H_{E}^{M_{2}+H_{Az}M_{1}})\cos\delta/M_{O} \\
0 & (M_{1}\sin\delta) & (M_{1}\cos\delta)
\end{vmatrix} = 0$$
(3.21)

Then,

$$M_1 H_y - [M_1 M_2 H_E / M_0 - (H_E M_2 + H_{Az} M_1) M_1 / M_0] \sin \delta = 0.$$
 (3.22)

From Shapira and Foner, 10 $M_1 = M_2$ for a perpendicular field, and $\sin \delta = 1$ ($\delta = 90^{\circ}$) at the AF-P transition. Then the AF-P boundary is given by

$$H_{y} = (2H_{E} + H_{Az}) M_{1}(T)/M_{o},$$
 (3.23)

where the magnitude of $\rm M_1$ and $\rm M_2$ is assumed to be independent of the field, $\rm H.^{10}$

If an additional small anisotropy field, ${}^{H}_{Ay}({}^{H}_{Ay}({}^{H}_{Az}),$ is assumed to have its axis parallel to y, then applying a field, ${}^{H}_{y}$, gives a different AF-P boundary. Using 3.20,

$$0 = \begin{vmatrix} i & j & k \\ 0 & [H_{y} + (H_{Ay}M_{1} - H_{E}M_{2}) \sin\delta/M_{0}] & (H_{E}M_{2} + H_{Az}M_{1}) \cos\delta/M_{0} \\ 0 & M_{1} \sin\delta & M_{1} \cos\delta \end{vmatrix}.$$
(3.24)

Then,

$$0 = M_1 H_y + (H_{Ay} M_1 - 2H_E M_2 - H_{Az} M_1) M_1 \sin \delta / M_0.$$
 (3.25)

Since $M_1 = M_2$ and $\sin \delta = 1$ at the AF-P boundary,

$$H_y = (2H_E + H_{Az} - H_{Ay})M_1(T)/M_0.$$
 (3.26)

The anisotropy assists in aligning the spins with $H_{_{\!\!\!\boldsymbol{V}}}$, and the AF-P intercept at T = 0 occurs at a lower field that that given by equation 3.23.

With a field, H_{χ} , applied perpendicular to this $\mathbf{H}_{\mathbf{A}\mathbf{V}}$ axis and the easy z axis, the spins rotate toward the x axis. Then

This gives an equation similar to 3.22; and the AF-P boundary is

$$H_{x} = (2H_{E} + H_{Az}) M_{1}(T)/M_{O}.$$
 (3.28)

Since the spins have rotated in a plane perpendicular to $H_{\mbox{Ay}}$, this additional anisotropy has no effect in this case.

One can calculate the AF-P perpendicular boundary near T_N for a two sublattice Ising or Heisenberg model. Assuming no anisotropy for the Heisenberg case, a field, H_y , is applied perpendicular to the easy axis, z, (as in 3.21) with δ the angle made with the z axis $(\underline{H}_{eff} = \underline{H}_y - \lambda \underline{M}_2)$. Then from 3.20,

i j k
$$0 M_1 \sin \delta M_1 \cos \delta = 0.$$

$$0 H_y^{-\lambda M_2 \sin \delta} \lambda M_2 \cos \delta (3.29)$$

Then as in 3.22,

$$\sin \delta = H_{V}/[2\lambda M_{2}(0,T)];$$
 (3.30)

or at the AF-P boundary where δ = 90°,

$$H_{y} = 2\lambda M_{2}(O,T).$$
 (3.31)

For T just below T_N at zero field, 10

$$M_2(0,T)=Ng\mu_BS[10(S+1)^2/(6S^2+6S+3)]^{1/2}(1-T/T_N)^{1/2}.$$
 (3.32)

Then using $kT_N = (2/3)S(S + 1)z_1|J_1|$, the AF-P boundary is, ¹⁰

$$(T_N-T) = (2s^2 + 2s + 1)g^2\mu_B^2H^2/(120 k^2T_N).$$
 (3.33)

With the Ising model, only the z components contribute to the effective field,

$$\underline{\mathbf{H}}_{\mathsf{eff}} = \underline{\mathbf{H}}_{\mathsf{Y}} - \underline{\mathbf{M}}_{\mathsf{2}_{\mathsf{Z}}} \tag{3.34}$$

Then,
$$\underline{M}_1 \times \underline{H}_{eff} = 0 = (\lambda M_1 M_2 \sin \delta - M_1 H) \cos \delta$$
, (3.35)

and $\sin \delta = H_y/\lambda M_2$, or at the AF-P boundary,

$$H = \lambda M_2(O,T)$$
. (3.36)

Using this in 3.32 would give

$$(T_N^{-T}) = (2s^2 + 2s + 1)g^2 \mu_B^2 H^2 / 30k^2 T_N,$$
 (3.37)

which is four times the result obtained from equation 3.33.

TV. EXPERIMENTAL METHODS

A. Experimental Apparatus

1. Dewar and Calorimeter

The low temperature apparatus consisted of the pyrex helium dewar shown in Fig. 6, and the calorimeter shown in Figs. 7 and 8. The dewar was made to specifications by H. S. Martin and Son, Evanston, Illinois. The lower portion was tapered to fit between the poles of a magnet. With the dewar filled with liquid helium and the outer vacuum can (C) evacuated, a temperature of 1.0° K could be attained by pumping on the bath in the helium can (A).

Heat leaks to the helium can (A) were reduced by several means. German silver, having a low thermal conductivity, was used for the pumping lines from the outer can flange to the inner can (B) and helium can (A). The pumping lines leading from the main dewar was used for the inner can (B) and helium can (A). A nylon spacer was put in the outer can (C) to prevent this outer can from touching the inner can (B). The inner can pumping lines, containing the electrical leads, were surrounded at their lower ends by the liquid helium in the helium can (A).

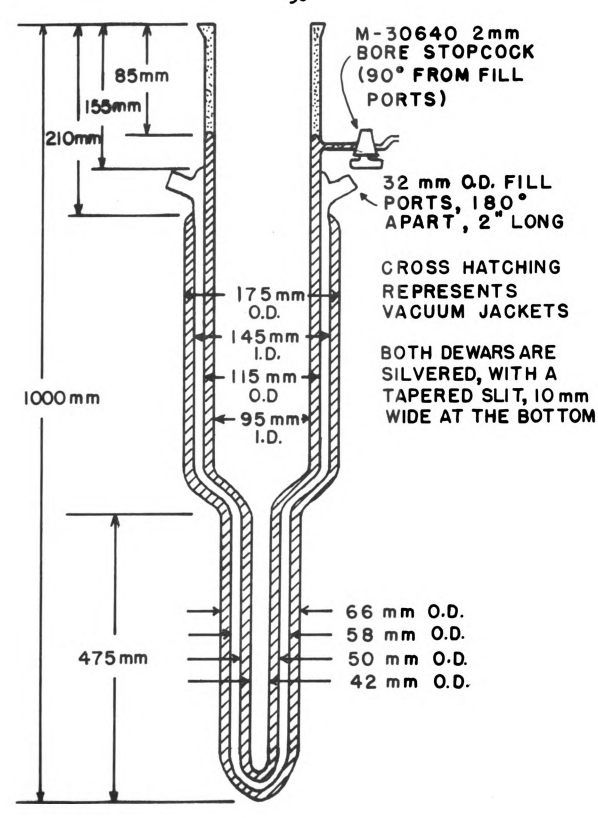


Figure 6. Pyrex helium dewar.

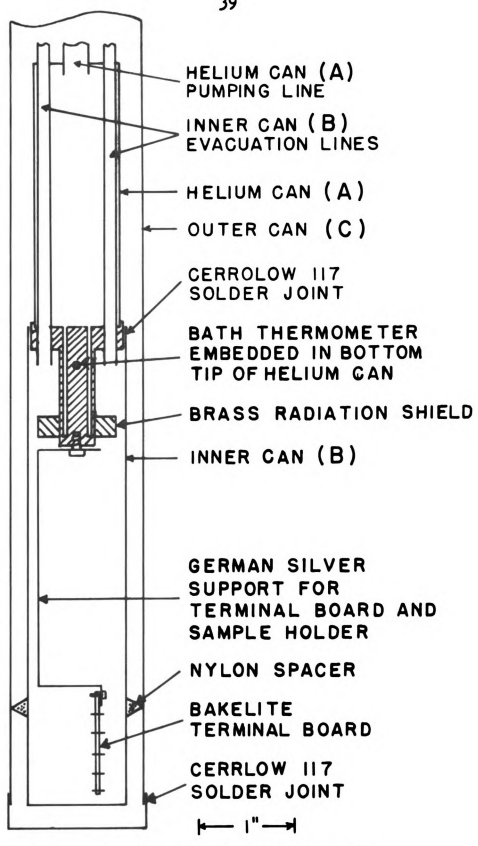
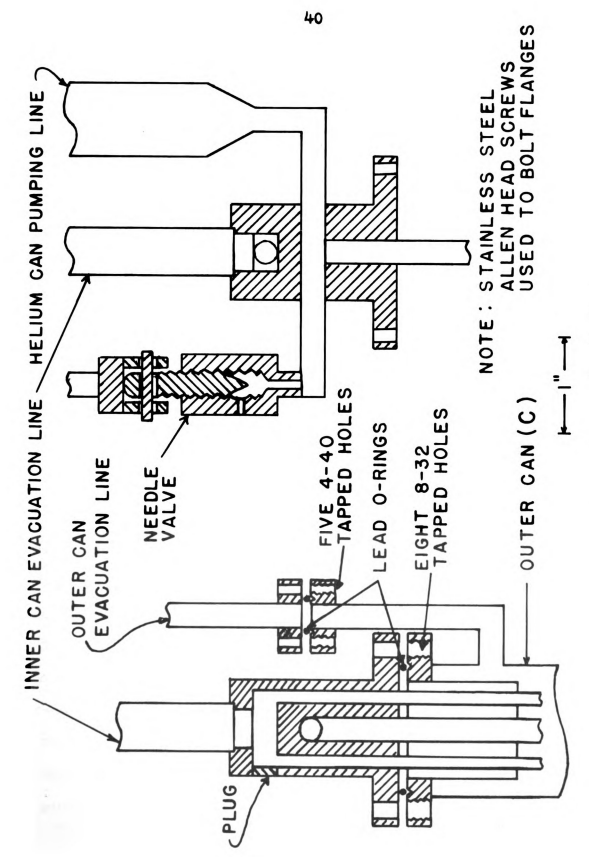


Fig. 7. Cross section of body of calorimeter.



Front and side cross sections of top of calorimeter. Fig. 8.

The electrical leads were varnished to the bottom of the helium can (A) for good thermal contact.

To reduce radiation, right angle bends were put in the pumping lines to the inner can (B), helium can (A), and outer can (C). Also, a brass radiation shield was placed below the ends of the inner can pumping lines, and an extra shield was placed at the end of the outer can pumping line. To increase the thermal resistance between the sample and bath in order to isolate the sample, the sample was supported by a nylon holder which was attached to the bakelite terminal board. The terminal board was connected to the helium can (A) by a strip of German silver.

2. Sample Holder

A nylon c-clamp was made to size for each sample and was attached to the nylon support (see Fig. 9). Nylon was used for its low thermal conductivity, and also since it could be cut easily and tapped for bolt threads. 2 Screws had to be tight since the crystal would experience a torque in the magnetic field. The larger nylon support was used when it appeared that the KMnCl₃·2H₂O crystal may have moved during a rotation experiment. When this much stronger support was used, no change in crystal position could be observed.

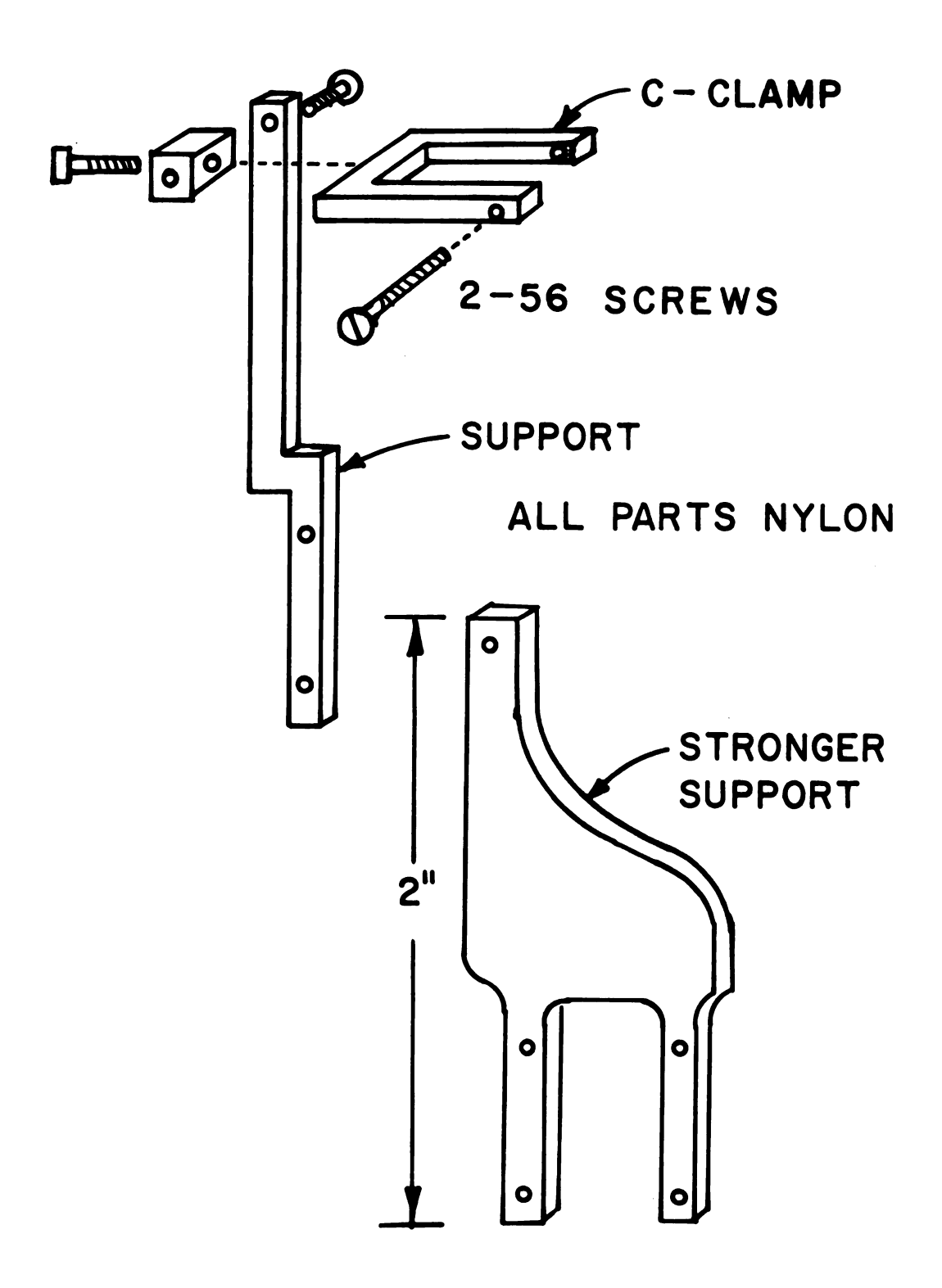


Figure 9. Sample holders.

The nylon support and c-clamp provided a thermal path between the bath and sample. On rotating the field, the sample temperature would change considerably, and the thermal path would tend to slowly bring the sample temperature back to its original value. This heat leak would have less effect on a sample with a large heat capacity. Thus, the smaller support, with a lower thermal conductivity, was used for the smaller samples.

3. Vacuum Pumps

A Welch Duo-Seal pump was used to maintain a vacuum on the U-tube manometers and to evacuate the McLeod gauge after a reading. Another such pump was used as a forepump for the air cooled Veeco EP 2AI 350 watt diffusion pump which could attain a pressure of 10⁻⁶ mm Hg. This system was used to pump out the inner and outer cans. A high capacity Stokes vacuum pump was used to pump on the dewar or the bath in the helium can. The pumping system is shown schematically in Fig. 10.

4. Pressure Gauges

A mercury filled U-tube manometer was used to measure helium can pressures above 2.5 cm Hg. Below that pressure an oil filled U-tube manometer was used to roughly observe the lowering of the pressure in equal temperature intervals for thermometer calibration, while a McLeod gauge measured these pressures accurately.

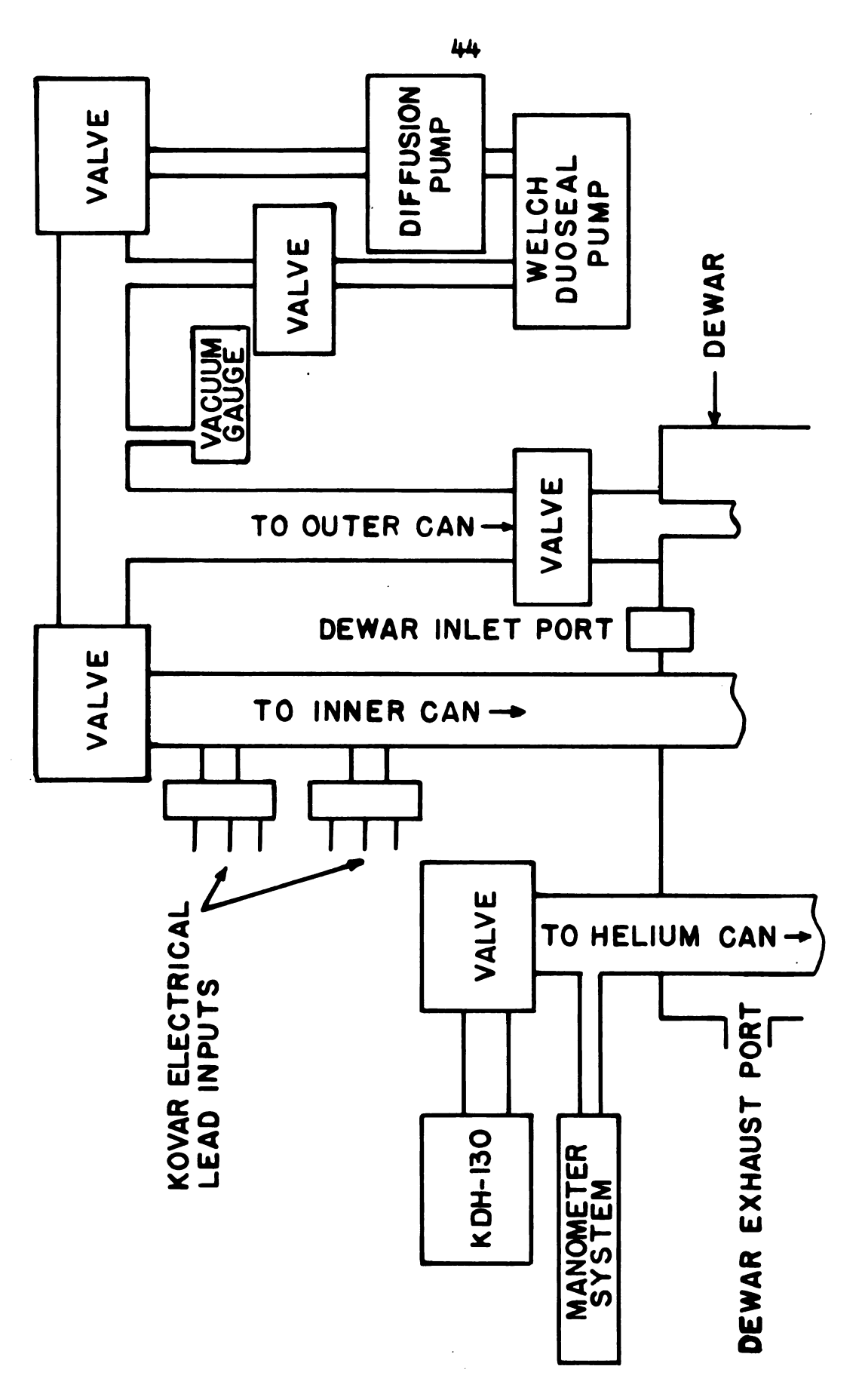


Fig. 10. Schematic diagram of pumping systems.

The high vacuum system for the inner and outer cans could be read on a NRC 831 vacuum ionization gauge. This simultaneously gave readings for the ion gauge at pressures below .001 mm Hg and for two thermocouple gauges. Both the helium can and the dewar had a U.S.G. pressure guage which gave rough readings (30 in. vacuum to 15 P.S.I.).

5. Thermometer Current Supplies

The sample and bath thermometers were 1/10 watt,
56 ohm, Allen Bradley carbon resistors. One set of leads
carried a constant current of one or ten microamperes,
while another set measured the voltage across the resistor
potentiometrically.

The sample thermometer current supply consisted of two 28 volt Mallory mercury batteries in series with three precision resistors, a variable 20 megohm carbon potentiometer, and a 100 K ohm precision resistor, all totalling 56 megohms. The current could be adjusted to one microampere by setting the variable resistor while potentiometrically measuring the voltage across the 100 K ohm resistor. The bath thermometer supply had 5.6 megohms and 10 microamperes. It was noticed that room temperature variations would give rise to fluctuations in these current supplies. After the supplies for the sample and bath

thermometers were enclosed in a 1/2-inch thick wooden box, these fluctuations were substantially reduced.

6. Measuring Electronics

The sample thermometer voltage was measured by a Leeds and Northrup K-3 potentiometer with a galvanometer system consisting of a Leeds and Northrup 9835-B microvolt amplifier and a Leeds and Northrup dual pen Speedomax G recorder with a 5 millivolt range card. The amplifier could be adjusted to give the amount of sensitivity desired. The bath thermometer voltage was measured by a similar system using the other pen of the two pen recorder with a 10 millivolt range card. The circuits are diagrammed in Fig. 11.

The voltage across the sample heater was measured with a Data Technology 323 integrating digital voltmeter. The heater current was measured by using a Leeds and Northrup Speedomax G single pen recorder to read the voltage across a precision resistor in series with the heater. A filtered Lambda LM263 power supply (0 to 32 volts) in series with a set of variable resistors totaling 10 megohms provided the heater current. The heater was turned on and off by a relay connected to an electronic timer which was preset to run for a selected time interval.

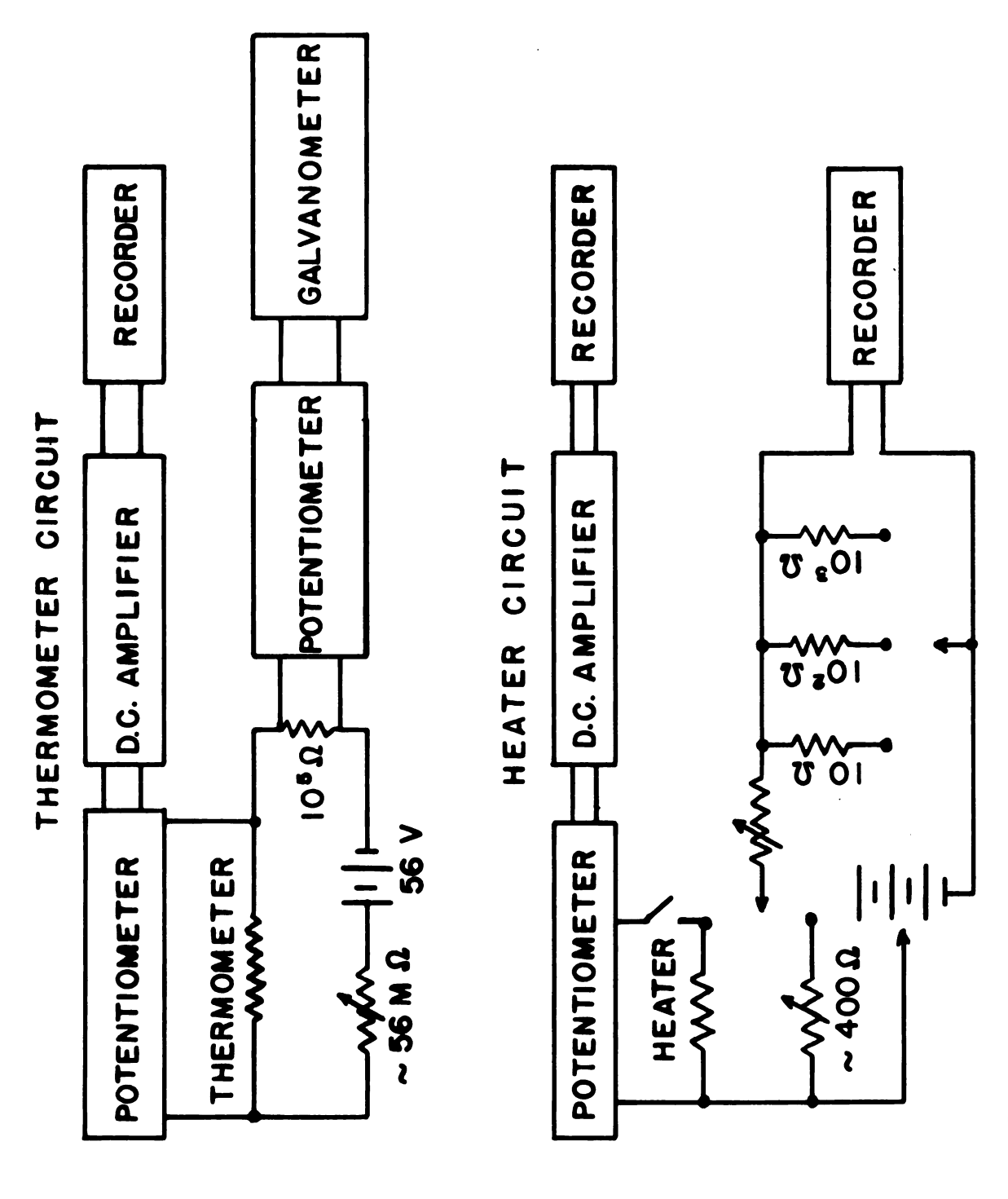


Fig. 11. Diagram of electrical measuring circuits.

7. Magnet and Gaussmeter

The magnetic field was provided by a water cooled Harvey Wells 22 KG magnet with a Harvey Wells DC power supply providing up to 200 amperes at 80 volts. An electric motor with two reduction boxes could rotate the magnet at 2.8, 14, or 70 degrees per minute. Angles were measured using the 360 gear teeth on the base of the magnet. The field could be increased or decreased linearly at any desired rate up to 3000 gauss per minute. This sweep circuit compares the output from a stationary coil on the magnet pole with the set reference voltage. This voltage difference drives the integrator and high frequency correcting amplifier, forcing the field to be proportional to the time integral of the reference voltage. Using a constant reference voltage gave a constant sweep rate.

The field was measured to within 10 gauss with a Bell 660 digital gaussmeter using a Hall probe. The probe was taped to the face of the pole, slightly off center, where the field strength was equal to that on the midpoint of the axis of the poles. The calibration of the gaussmeter was checked with a Rawson-Lush rotating coil gaussmeter using a Rawson-Lush 501 indicator. A nuclear magnetic resonance experiment had demonstrated the Rawson-Lush gaussmeter to be accurate to within 50 gauss.

B. Experimental Procedures

1. Sample Preparation

The LiCuCl₃·2H₂O crystals were grown from an aqueous solution containing approximately 14.9 grams of LiCl and 60 grams of CuCl₂·2H₂O, both reagent grade chemicals. For KMnCl₃·2H₂O, the solution contained approximately 179 grams of MnCl₂·4H₂O and 27.0 grams of KCl, also reagent grade chemicals. These amounts were determined by examining the solubility phase diagram. The solutions were kept at room temperature in a dry box which had a small dehumidifier to enhance the crystal growth. The crystals were generally grown to approximately one gram in size.

The crystallographic axes were determined from the prominent crystal faces and, if necessary, by x-ray diffraction. From proton resonance and x-ray diffraction data, LiCuCl₃·2H₂O has its easy magnetization axis in the AC plane which is represented by a face normal to the B axis. Since the crystal has the tendency to deteriorate on handling, the x-ray work was done rapidly in order to check the B axis orientation.

With KMnCl₃·2H₂O, the crystal faces were not easily recognized, and the easy magnetization axis was not perpendicular to any crystal axis. Thus, x-ray work was imperative, not only for determining the axes but also to

decide whether the crystal was single or twinned. Figs. 1 and 3 show the crystal spin arrangements of LiCuCl₃·2H₂O and KMnCl₃·2H₂O respectively.

After determining the crystal axes, the crystals were weighed. Then, a heater (approximately 400 ohms of 1.4 mil diameter, double enameled Evanohm* wire) was wound on the crystal, and a 1/10 watt, 56 ohm Allen Bradley carbon resistor thermometer was mounted on the crystal. Both heater and thermometer were connected at each end with two six inch coiled manganin wires with nominal resistivity of thirty ohms per foot. The resistors were cooled by a fan during soldering to reduce any damage from overheating.

To protect the crystals and to provide mechanical support for the heater and thermometer, the KMnCl₃·2H₂O crystals were coated with a thin layer of clear glyptal (G.E. 1202 varnish). The LiCuCl₃·2H₂O samples, however, were coated with Fluorolube** grease since they were not sufficiently stable at room temperature to allow varnish to dry. An 1/8" thick nylon c-clamp was then put on the crystal and tightened so the crystal would not turn when placed in a magnetic field.

^{*}Obtained from Wilbur B. Driver Co., Newark, N.J.

^{**}Obtained from Cenco.

2. Preparing for Experiment

Using information on the morphology of the crystal as well as the direction of easy magnetization, generally obtained from x-ray work and nuclear magnetic resonance, the crystals were mounted so that the axis of easy magnetization was in the plane of the magnet's rotation. It was possible to do this within five degrees of the desired position. Further, the orientation first chosen was generally the one which was the least ambiguous in its direction. Sometimes there was a small alignment error, indicated by the fact that the critical fields were unusually high. Furthermore, the discernment of this critical field by the adiabatic method became more and more difficult at higher temperatures.

During the first run, a plot was made of the critical field as a function of magnet rotation. This plot would serve as a guide for insuring proper alignment, since the minimum critical field generally was obtained for the best alignment. This plot also served to indicate any alignment error when the sample was rotated ninety degrees about the magnetization axis. The small corrections in angle were achieved trigonometrically by measuring the positions with a cathetometer. This technique was repeated until the spin flop field was at its lowest value.

After the clamp and sample were mounted on the nylon holder, the leads were soldered to the terminal board. Then the inner can (B) was sealed with low temperature Cerrolow 117 solder, and the electrical leads were checked at the terminals on top of the calorimeter.

Lead O-rings were fitted to the outer can (C) which was then bolted tightly in place. To help keep the LiCuCl₃·2H₂O samples from melting during this preparation, the inner (B) and outer can (C) evacuation lines were shut; and the cans were submerged in liquid nitrogen.

Next the calorimeter was lowered into the dewar and the dewar was then evacuated. The outer dewar was filled with liquid nitrogen, and after about twenty minutes, helium gas was put into the dewar to cool the calorimeter overnight. The outer can (C) was usually checked for leaks by pumping on it; and if vacuum tight, it was then filled with helium gas.

3. Helium Transfer and Thermometer Callibration

Prior to the liquid helium transfer, the sample thermometer resistance, atmospheric pressure, and room temperature readings were taken with the sample at liquid nitrogen temperature. To further check for any possibility of vacuum leaks, the inner (B) and outer (C) cans were evacuated separately to a pressure of 2×10^{-4} mm Hg. If

the system appeared to be tight, approximately 2 mm Hg of helium exchange gas were put into both cans.

The needle valve to the liquid helium can (A) was closed and four or five liters of liquid helium were transferred into the helium dewar by pumping on the dewar to keep its pressure about one pound below the pressurized storage dewar. The sample and bath thermometers were monitored to observe their cooling. Using a level sensor consisting of four carbon resistors placed at different levels in the liquid helium dewar, it was possible to check the height of the incoming liquid helium.

After transferring, the needle valve on the liquid helium can (A) was opened to permit filling. Then the magnet was rolled into position and the field was brought up to the value chosen for calibration. The outer vacuum can (C) was then evacuated in order to thermally isolate the inner vacuum can (B) and liquid helium can (A) from the liquid helium dewar. When the sample and bath thermometers had reached equilibrium, the thermometer calibration was begun. This involved pumping on the liquid in the helium can (A) which necessitated closing the helium can needle valve. Generally 10-15 calibration points were taken in the temperature range 4.2-1.0° K. The calibration process consisted of reading the vapor pressure of the liquid on a mercury manometer and a McLeod gauge, and reading the resistance of the sample thermometer on a

Leeds and Northrup K-3 potentiometer with a fixed current of one microampere through the carbon thermometer.

4. Adiabatic Field Rotations

After the calibration had been completed, the inner vacuum can (B) was evacuated to isolate the sample. With the field at the calibration value, the magnet was rotated while the sample resistance was observed. A maximum in resistance (minimum temperature) was sought, as this indicated the position of the easy axis. The magnet was then fixed at this position (equivalent to being parallel to this easy axis). The field was then increased, and the temperature of the sample changed along this adiabatic curve. After the critical field was determined, 180 degree rotations were done in the antiferromagnetic and spin flop phases. The rotations in the spin flop state enabled one to determine the direction to which the spins flopped.

During a rotation, the bath temperature was held nearly constant, but the small heat leak through the sample holder would cause the sample temperature to differ slightly at positions 180 degrees apart. Because the sample temperature tended to differ from the bath temperature during most of the rotation experiment, this caused an annoying background warming or cooling in the sample. For this reason any maximum or minimum temperature

position could be shifted and had to be corrected for this heat leak. The background temperature effect could be observed by stopping the rotation and noting that the sample had not reached an equilibrium temperature. It was for this reason that it was necessary to do rotations of a few degrees, so that the sample could not be very far from temperature equilibrium, and hence the minimum position could be found more accurately.

5. Adiabatic Magnetizations

To determine the first order SF-AF (spin flopantiferromagnetic) boundary, the field, aligned with the
magnetization axis, was swept at 1000 or 2000 gauss per
minute. It was observed that the sample cooled while
still in the antiferromagnetic state; and when the spin
flop boundary was reached, the sample temperature would
either increase or would remain unchanged in agreement
with the expected effect from equation 1.32. Generally
data were taken at slower field sweeps, over smaller
field increments in order to minimize any possible heat
leaks.

The critical field for the SF-AF boundary was also checked at several angles. The magnetic field was increased to higher values in order to see whether the SF-P (spin flop-paramagnetic) boundary could be reached. The SF-AF boundary was consequently mapped out by taking

adiabatic curves for different starting temperatures. For the case of KMnCl₃·2H₂O, inflection points were observed at the SF-P boundary and at the AF-P (antiferromagnetic-paramagnetic) boundary by sweeping the field near these boundaries. Both of these boundaries were also obtained more accurately from specific heat data.

6. Specific Heat Measurements

In order to observe the AF-P boundary and SF-P boundary, specific heat measurements were taken. With a uniform slight warming or cooling of the sample thermometer as a background, a heater current of approximately 10 micro-amperes was used for twenty to forty seconds. Parameters recorded were the heater voltage, current, time, and also the number of divisions the chart recorder pen moved during the heating period. Calibration of the chart was also obtained by recording the pen positions at the extrema of the chart.

Sometimes it was possible to visually observe on the recorder the position of the maximum in the specific heat. This occurred when the number of chart divisions suddenly increased for a given heat input. These specific heat measurements were taken for different values on the magnetic field, thus enabling one to plot out the AF-P and SF-P boundaries.

After a specific heat measurement at a given field, it was generally necessary to introduce a small amount of exchange gas into the sample container in order to cool the sample to lower temperatures (and hence below the phase boundary) before the start of another specific heat measurement at another field. The inner can (B) was then evacuated before more data was taken.

7. Removing Crystal

At the end of the experiment, the helium in the dewar and helium can (A) was pumped away. If an experiment was to be rerun with the same sample orientation, the liquid nitrogen dewar was filled up so that the sample would remain cold. Procedures outlined in C. were then repeated for the next experimental run. When there would be several days between runs for KMnCl₃·2H₂O, the dewars were allowed to warm up (not adding any liquid nitrogen) with nitrogen gas in them and in the inner can (B), both of which were vented to the atmosphere by a one-way valve.

To remove the calorimeter, the liquid helium dewar was filled with nitrogen gas. The inner vacuum can (B) was filled with air or nitrogen before it was unsoldered. Then the sample orientation could be changed or the crystal could be removed after unsoldering the leads.

C. Data Analysis

1. Converting Pressure to Temperature

The manometer pressures were changed to pressures at 0°C by correcting for the density change of the mercury, and a hydrostatic pressure correction was made for all points above the lambda point of helium to account for the height of liquid helium above the sample. Below the lambda point there is no temperature gradient in the liquid helium, and hence no hydrostatic correction was necessary.

All pressures were read on a mercury manometer, except those below 2.5 cm Hg, for which a McLeod gauge was used. The corrected helium pressure readings were converted to temperatures using the "1958 He⁴ Scale of Temperatures." The first calibration point was taken at liquid nitrogen temperature for which the temperature can be calculated using 13

$$T = \frac{255.821}{6.49594 - \log_{10} P} + 6.6.$$

Here P is atmospheric pressure read in millimeters and corrected to 0°C.

2. Thermometer Calibration Equation

A least squares fit to the calibration points was performed using a Hewlett Packard 9100A calculator and using the standard equation 14

$$\sqrt{\frac{\log R}{T}} = a + b \log R.$$

This calculation was done immediately after the calibration was completed so that the results could be used as a close check on temperatures while running the experiment.

For the M.S.U. CDC 6500 computer, the equation was modified to give a better fit:

$$T = \log R \left[\frac{a + b \log R}{4 \cdot 1 - \sum_{n \in \mathbb{N}} (\log R)^n} \right]^{-2}$$

A fourth degree polynomial gave the best fit to the calibration points below 4.2°K. When extrapolation above these points was needed (as e.g., for LiCuCl₃·2H₂O), the polynomial was omitted giving the basic two parameter equation. This linear fit gave the best results when only the six highest points were used.

3. Chart Recorder Calibration

For specific heat points, magnet rotations, and field sweeps, the data was taken with the chart recorder pen offset from its null position. The thermometer resistance, R_T , could be calculated on the computer from the potentiometer setting, R_O , and the number of divisions, D, that the recorder pen was to the right of null, using the following equation: 2

$$R_{T} = \frac{R_{O} - [C_{1} - C_{2}R - 2C_{3}R^{2} - 3C_{4}R^{3}]D}{1 + [C_{2} + 2C_{3}R + 3C_{4}R^{2}]D}$$

An iteration process was used to determin $R_{\mathbf{T}}$, by initially setting R equal to $R_{\mathbf{O}}$ to obtain a first approximation of $R_{\mathbf{T}}$. This new $R_{\mathbf{T}}$ value was then substituted for R in the above equation, to determine a second approximation to $R_{\mathbf{T}}$, etc. This process was repeated until two successive values for $R_{\mathbf{T}}$ differed by 0.1%.

The coefficients, C, were found from a least squares fit to the voltage calibration points using the relation:

$$\frac{R_{O}L - R_{O}R}{DL - DR} = C_{1} + C_{2}R_{T} + C_{3}(R_{T})^{2} + C_{4}(R_{T})^{3}.$$

A voltage calibration point was taken whenever the increase or decrease of sample temperature necessitated moving the recorder pen across the recorder chart by changing the potentiometer setting. The resistance change in these two settings is represented by $(R_OL - R_OR)$, and (DL - DR) is the corresponding change in divisions (see Fig. 12a). The resistance value, R_T , used for the calibration point was approximately by the average resistance, $(R_OL + R_OR)/2$, since the null was at the page center and the pen was moved from one side of the page to the other.

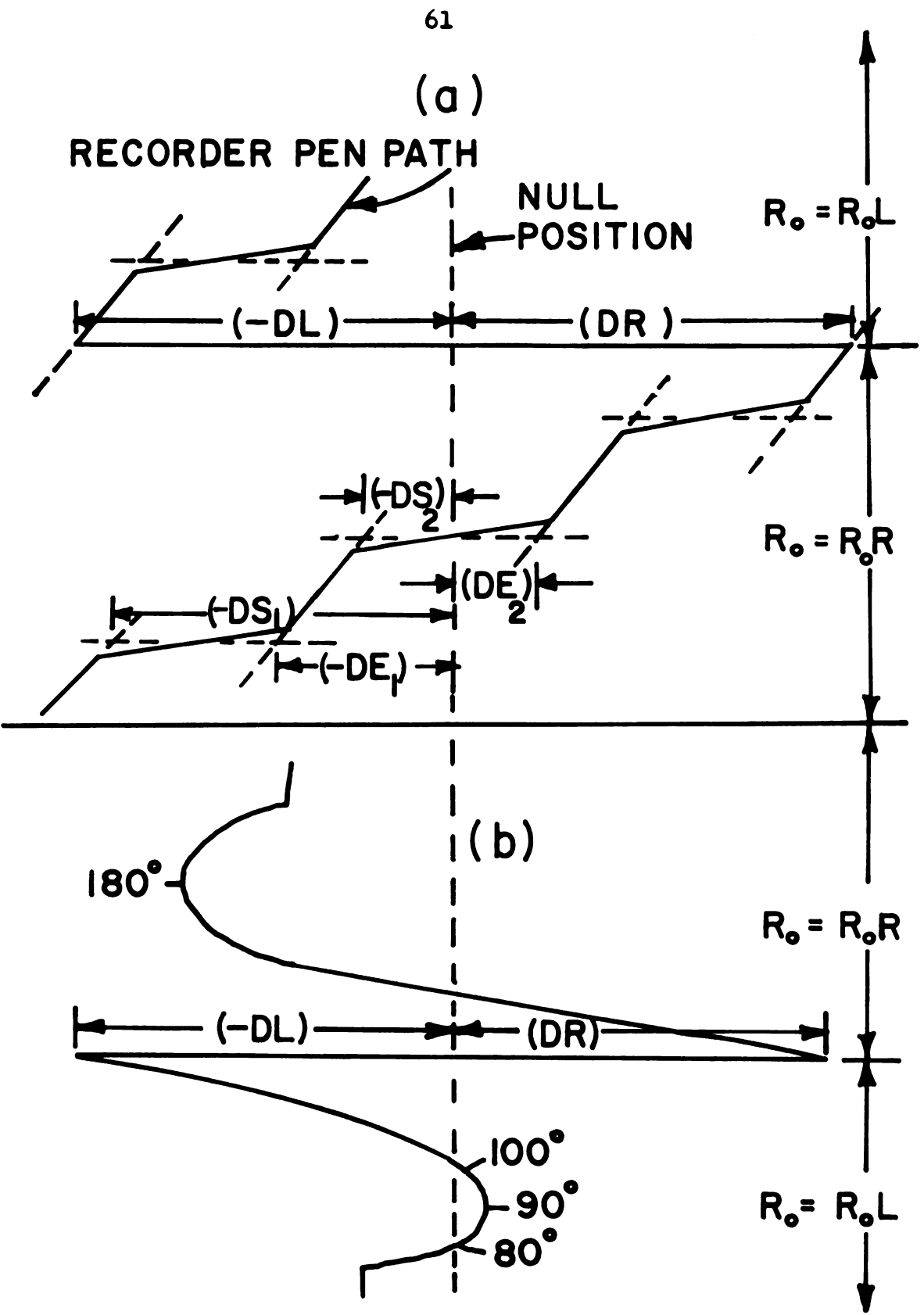


Figure 12. Example of data on chart recorder.

4. Specific Heat, Rotations, Field Sweeps

For specific heat points, the heat input was the product of the heater voltage, current, and heating time. The sample mass and molecular weight were used in order to convert heat capacity measurements to specific heat results. The heat leaks were subtracted out graphically as in Fig. 12a. Resistances were calculated for the start and end of each specific heat point. The temperature difference was used in the specific heat calculation, and the average of the two temperatures was taken as the temperature for that point.

For magnetic rotations and field sweeps, the chart recorder was marked when a certain angle or field was reached. As in the specific heat measurements, the temperature was determined from the resistance, which was calculated from the potentiometer setting and the divisions from the null position. Voltage calibration points were taken whenever the pen had to be moved, as with specific heat points (see Fig. 12b).

V. LiCuCl₃·2H₂O RESULTS

A. Adiabatic Rotations

In order to align the crystal so that the external field lies along the direction of easy magnetization, it is necessary to perform an adiabatic rotation of the external field in the AF state. The easy axis is determined as the temperature minimum in this rotation. This can be seen in Fig. 13a for H = 9.0 kG, when the rotation was done in the AC plane (see Table 1 in Appendix). In fact, this indication (Fig. 13b) is taken as a sign that the spin-flopping has occurred. Furthermore, this type of behavior also indicates that the spins have flopped in the plane (rather than out of it).

For comparison, rotations in the BC' plane (Figs. 14 and 15, and Table 2 of Appendix) show a small cusp starting to develop at 11.2 kG at the easy axis position. The cusp gets larger but fades out above 13 kG.

B. Adiabatic Magnetizations

When the field is increased adiabatically, the sample cools until the spin flop critical field is reached. Then the sample temperature would level out or increase

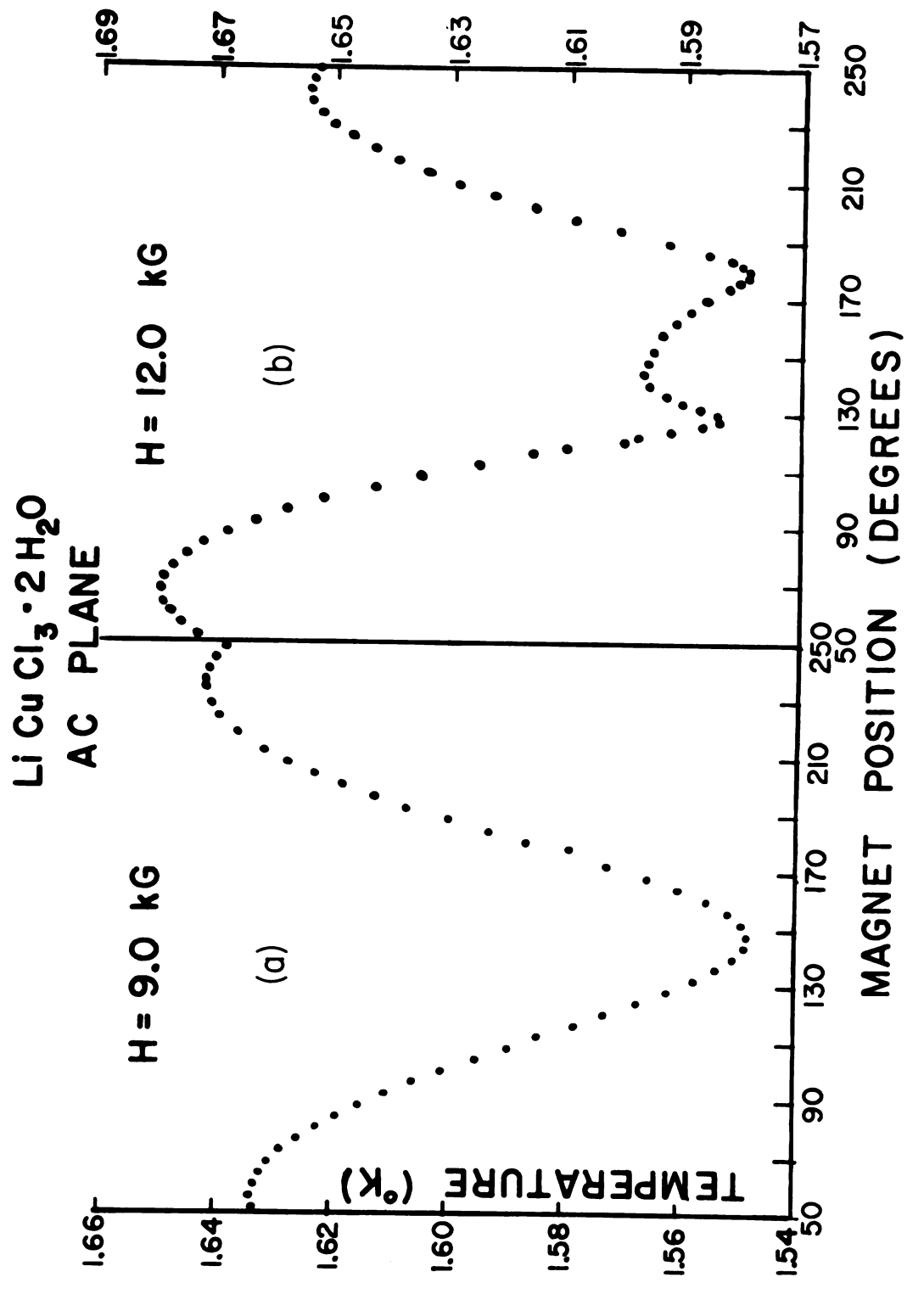


Figure 13. LiCuCl₃·2H₂O AC plane isentropic rotations.

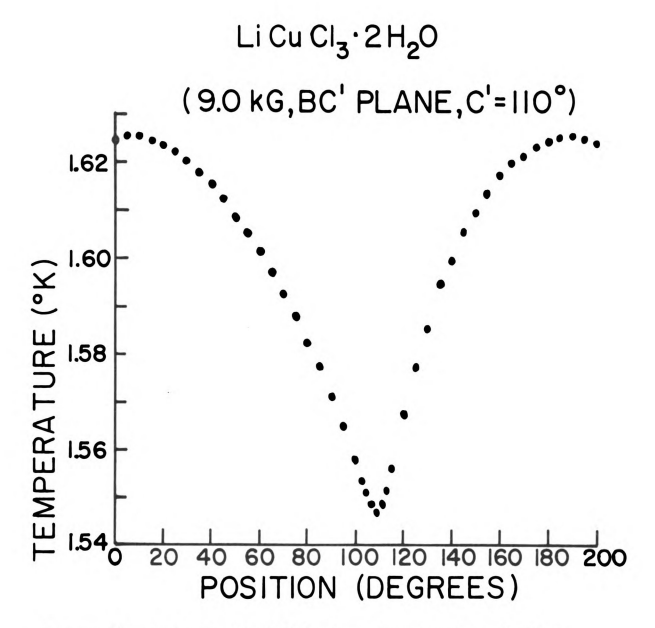


Figure 14. LiCuCl₃.2H₂0 BC' plane isentropic rotation.

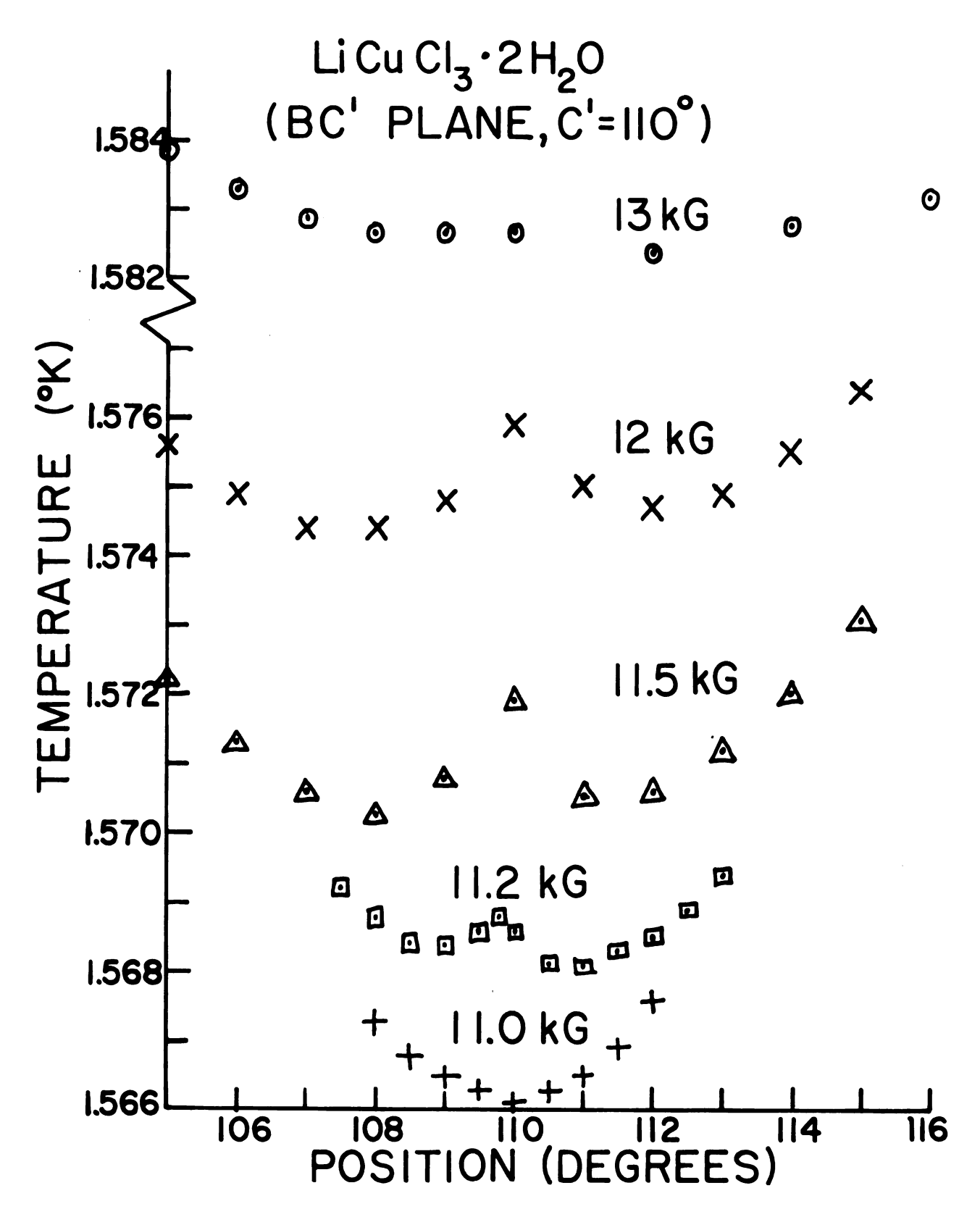


Figure 15. LiCuCl₃·2H₂0 BC' plane isentropic rotations.

as predicted by equation 1.32. These adiabatics are shown in Fig. 16 and Table 3 in Appendix. The AF-P and SF-P boundaries were found by specific heat measurements (Figs. 17, 18) and the magnetic phase diagram is shown in Fig. 19 (Tables 4, 5, and 6 of Appendix).

At the lowest temperatures, the AF-SF boundary was slightly lower for the AC plane than for the BC' plane (C' is the easy axis in the AC plane) (see Fig. 19). It was thought that the easy axis might have been slightly out of the rotation plane for the BC' case. At higher temperatures, however, the AF-SF boundary for the AC orientation occurred at higher fields and was more difficult to resolve than for the BC' case. Most of the difficulty lay in the reduced sensitivity of the sample thermometer near 4°K, causing a lower signal to noise ratio, and the fact that the temperature change of the isentropes was smaller than that found for other antiferromagnets.

An interesting effect in the BC' plane is that at the easy axis position there is a maximum for the critical field as a function of angle (Fig. 20a and Table 7 of Appendix). However, the sharpest anomaly for a field sweep occurred at the easy axis position, and the anomalies became broader and less distinct as the angle differed from the easy axis.

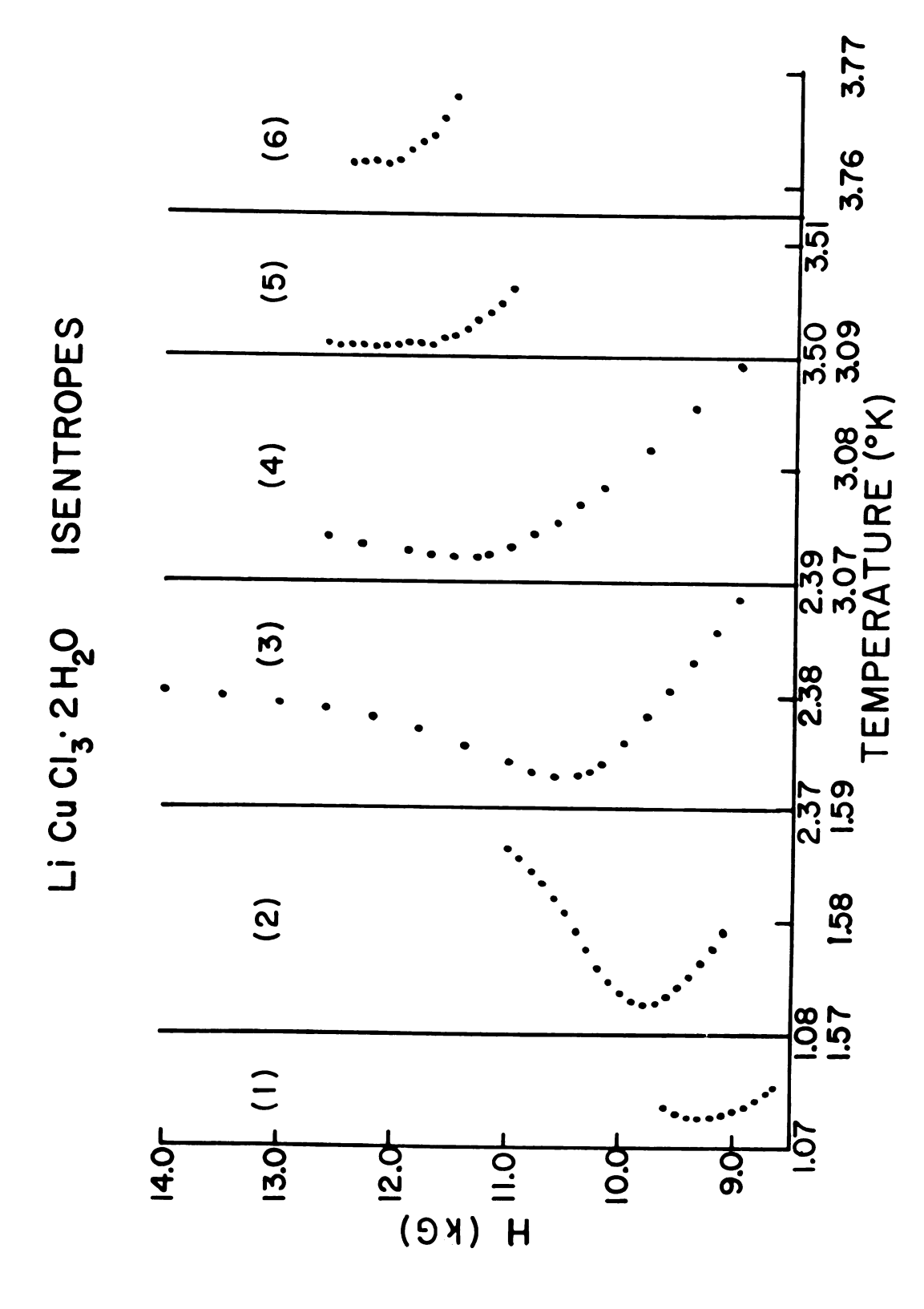


Figure 16. LiCuCl₃·2H₂O isentropic magnetizations.

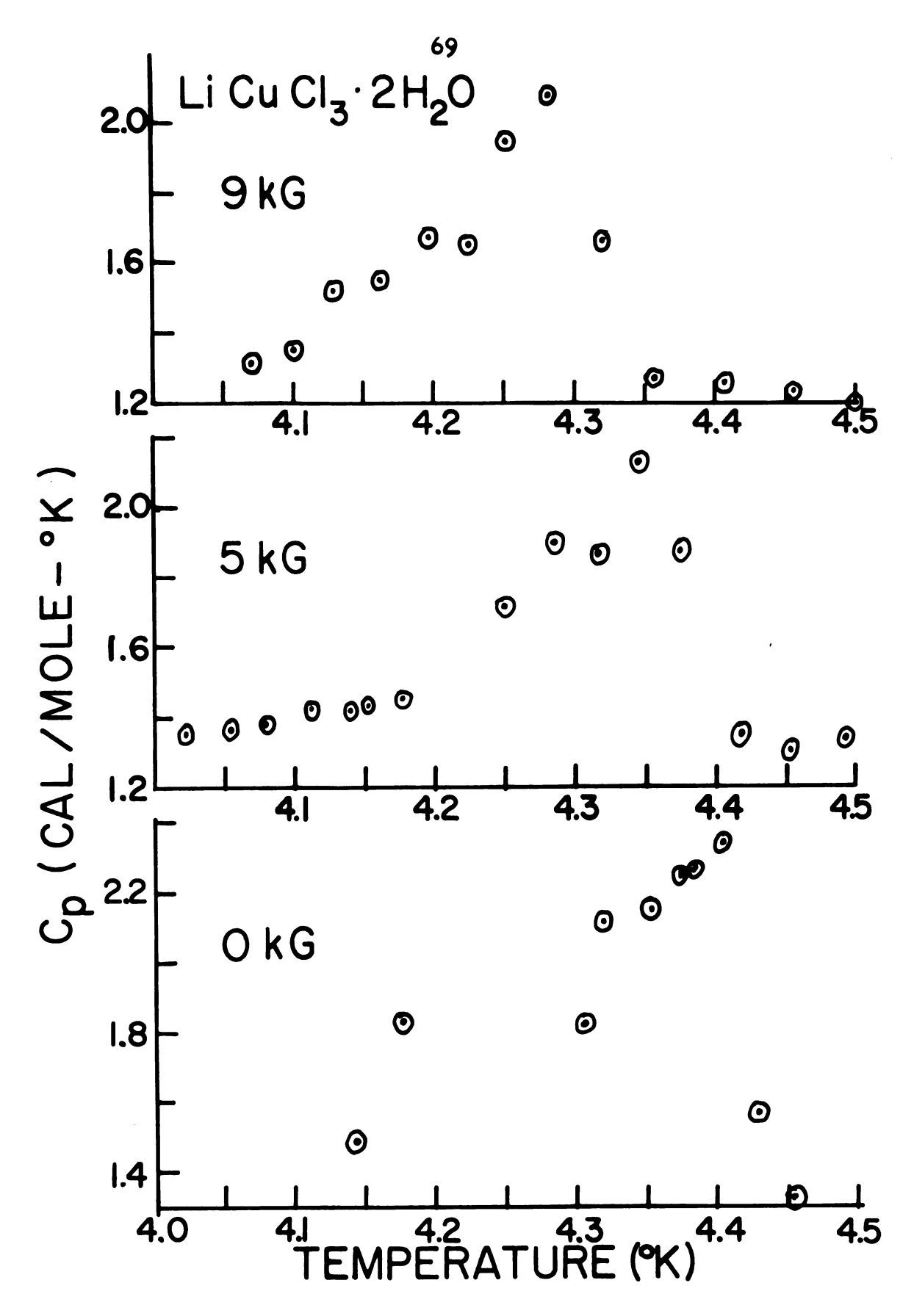


Figure 17. LiCuCl₃·2H₂0 specific heat data.

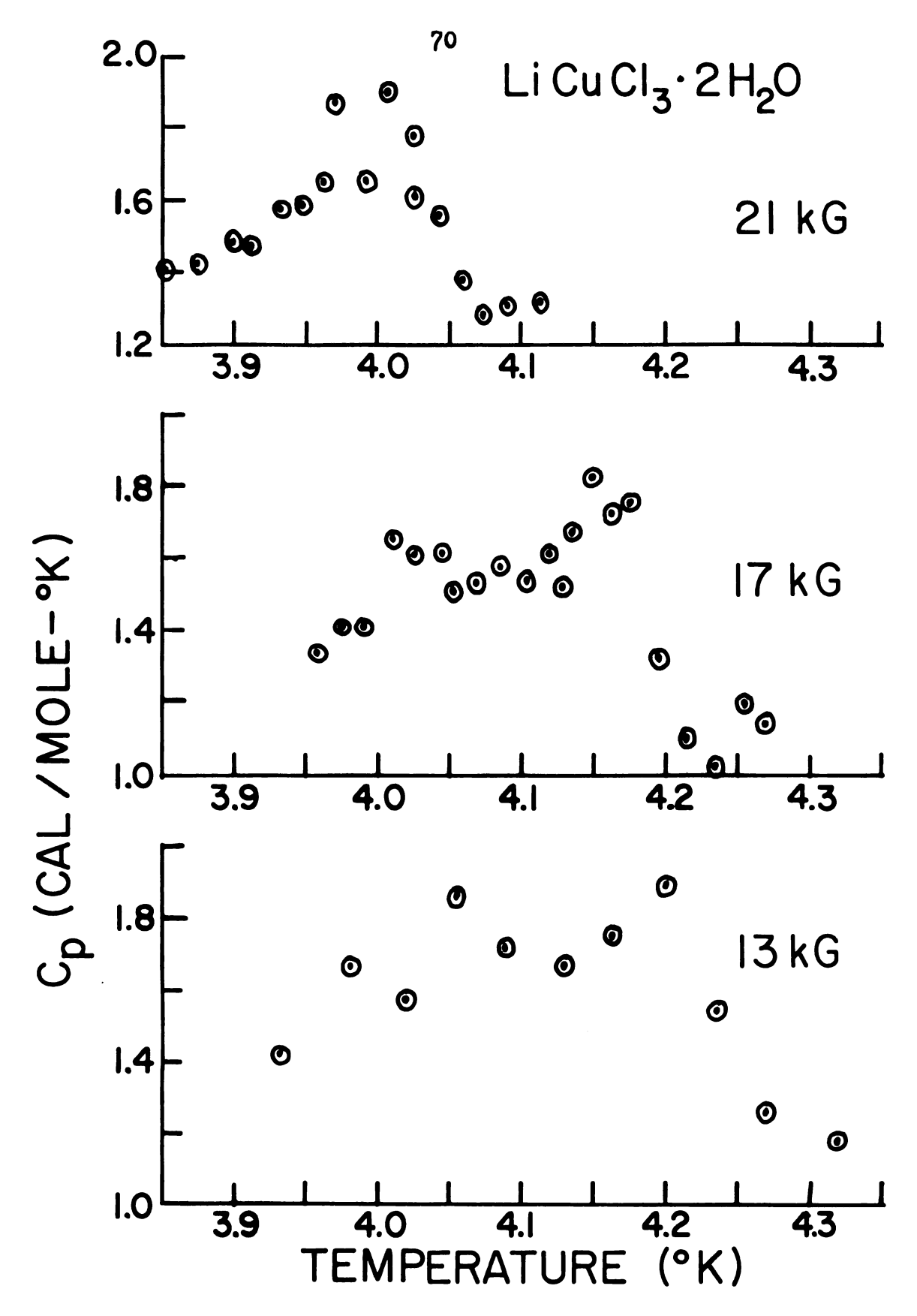


Figure 18. LiCuCl₃.2H₂0 specific heat data.

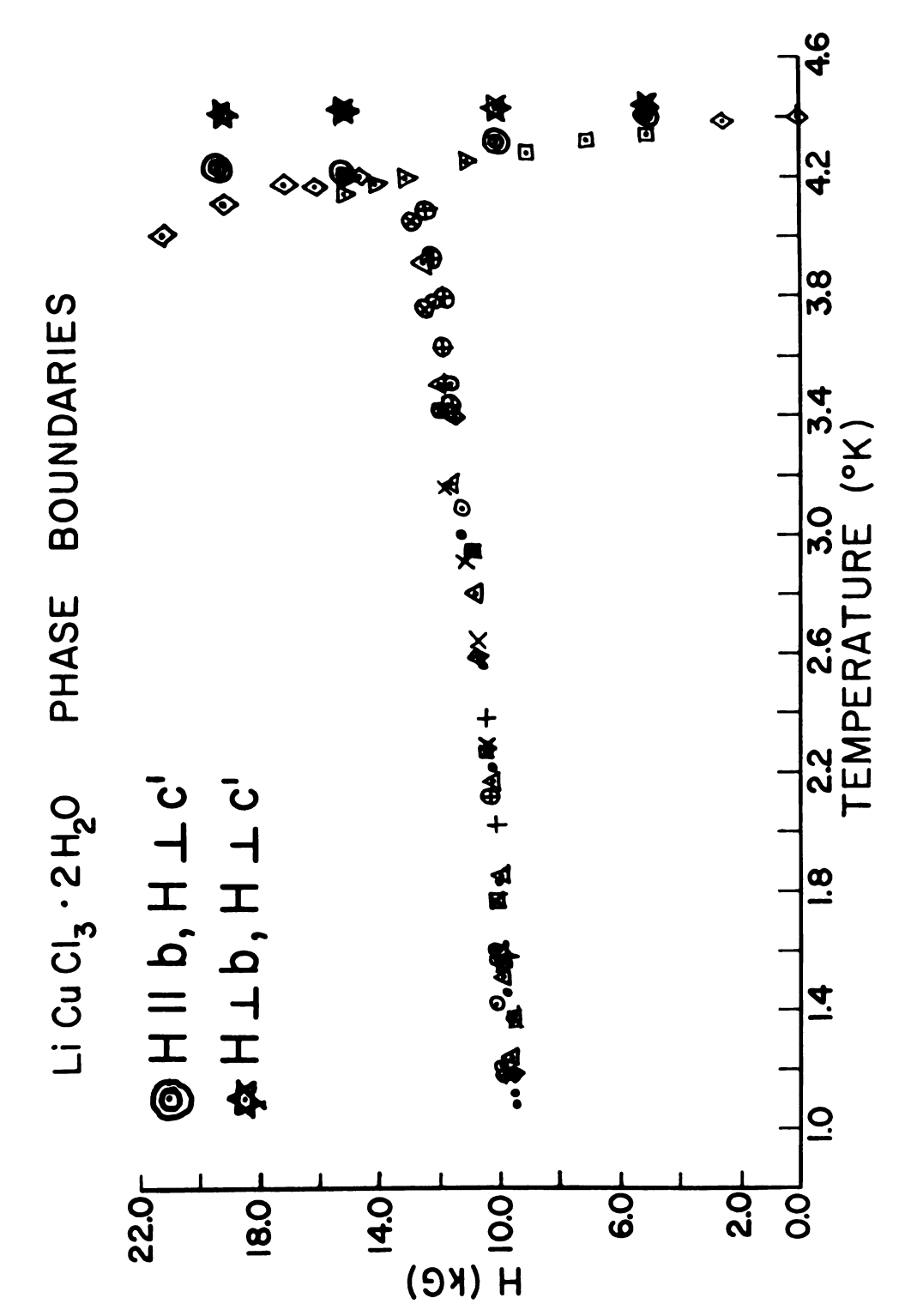


Figure 19. LiCuCl3.2H20 phase boundaries.

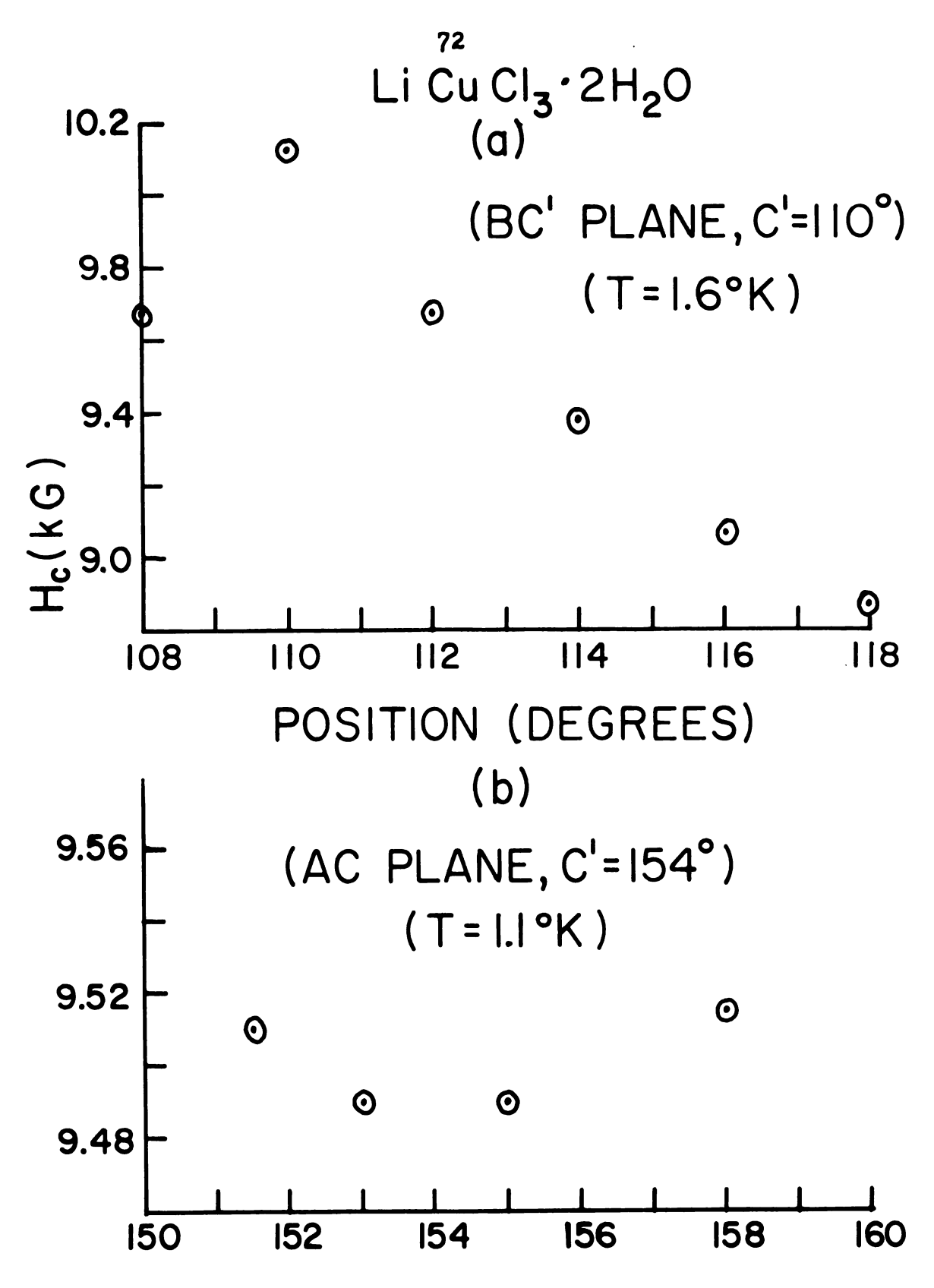


Figure 20. LiCuCl₃·2H₂0 angular dependence of critical field.

In the AC plane (Fig. 20b) there is a slight increase in critical field as the angle is varied from the easy axis. This is a more common effect and can be more easily understood, since the field strength along the C'axis is diminished when the field is off axis.

C. Antiferromagnetic-Paramagnetic Boundary

1. Field Parallel to the Easy Axis

This boundary is obtained from specific heat measurements, the data for which is given in Figs. 17, 18, and Table 4 of Appendix. For T close to $T_{\rm N}$, one can use equation 2.52 which neglects any intrasublattice interaction and assumes that the anisotropy energy is small compared to the exchange energy. For the case with the external field parallel to the easy axis this becomes,

$$(T_N^{-T}) = \frac{3g^2 \mu_B^2 (2s^2 + 2s + 1) H^2}{80kz_1 |J_1| s(s + 1)}$$
 (5.1)

A linear least squares fit to T vs. ${\rm H}^2$ constrained to pass through T at H = 0 is shown in Fig. 21. The fit is,

$$(T_N - T) = 1.35 \times 10^{-9} H^2,$$
 (5.2)

with H in gauss. Using equation 5.1, with $S = \frac{1}{2}$ and $z_1 = 4$, one obtains on comparing coefficients,

Li Cu Cl₃·2H₂O AF - P BOUNDARY

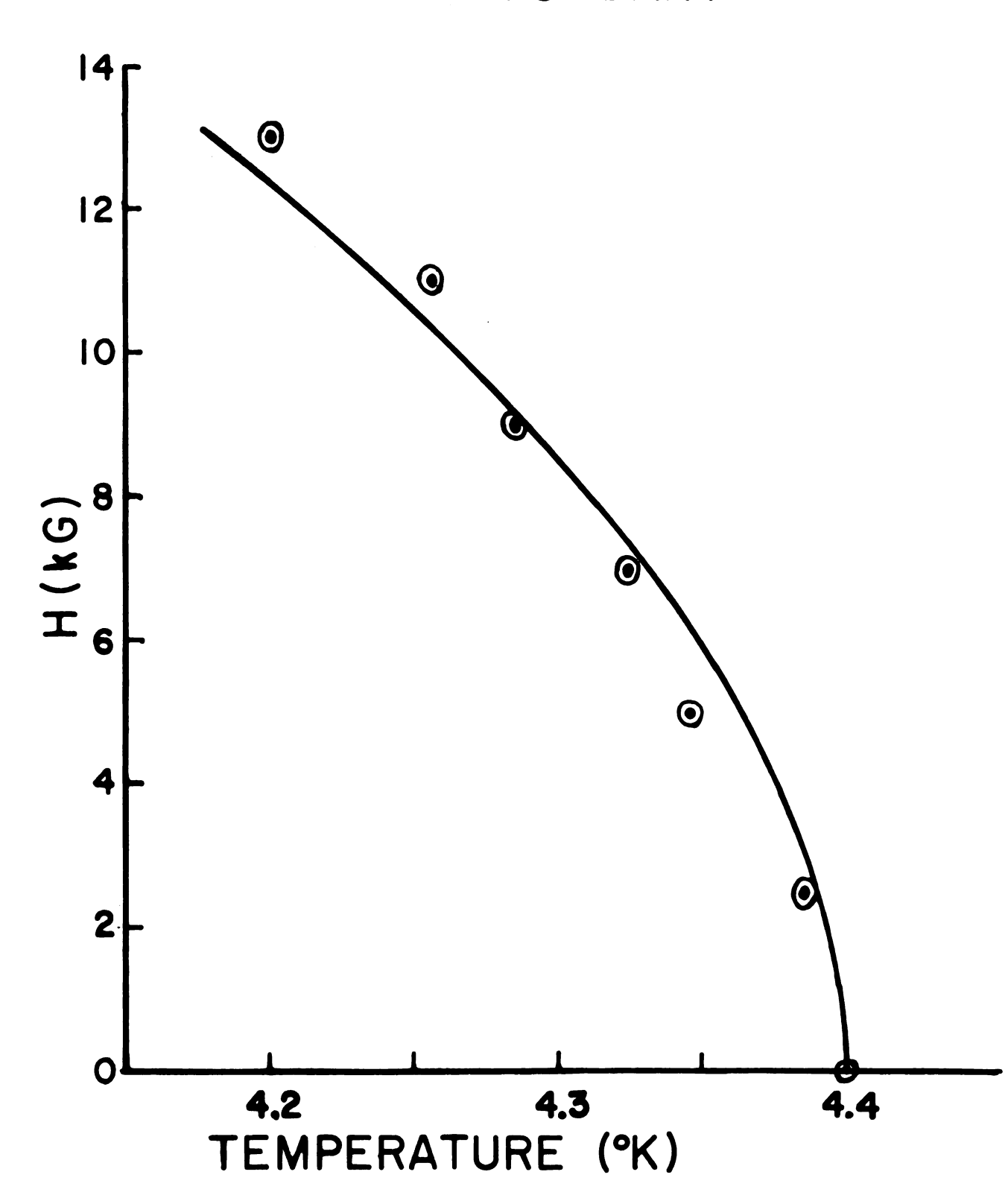


Figure 21. LiCuCl₃·2H₂O fit to AF-P boundary.

$$\frac{J_1}{k} = 0.42^{\circ} K. \tag{5.3}$$

Then the exchange field can be approximated using 1.5,

$$H_{E} = \lambda M \simeq \frac{2Sz_{1}|J_{1}|}{g\mu_{B}}.$$
 (5.4)

The result is, $H_E = 12.5$ kG.

If one uses the more general form for T_N (equation 2.48), it is possible to calculate an intrasublattice exchange interaction, i.e., using equation 2.50,

$$(T_N - T) = \frac{(2S^2 + 2S + 1) g^2 \mu_B^2 \left[1 + \frac{z_2 J_2}{z_1 J_1}\right] H^2}{40 k^2 T_N}.$$
(5.5)

This gives,

$$(T_N - T) = .26 \times 10^{-9} \left[1 + \frac{z_2 J_2}{z_1 J_1} \right] H^2.$$
 (5.6)
With $z_1 = 4$ and $z_2 = 1$, $\frac{J_2}{J_1} \approx 17$.

Such a large intrasublattice exchange is in agreement with the large amount of short range ordering persisting above the Neel temperature. 15 As deduced from the specific heat measurements, 48% of the total magnetic entropy is recovered above T_N . Although the above calculations have been made assuming that $(T_N - T)$ is proportional to H^2 , it is of interest to examine how the present data deviate (if any) from this relationship. For this

reason a plot has been made of $(T_N - T)$ vs. H, as shown in Fig. 22a. This result is given analytically as

$$(T_N - T) = 5.38 \times 10^{-9} \text{ H}^{1.38}.$$
 (5.7)

This deviation is not too suprising since the present data are extended over a wider range of temperature than is possibly valid for the two-sublattice molecular field approximation.

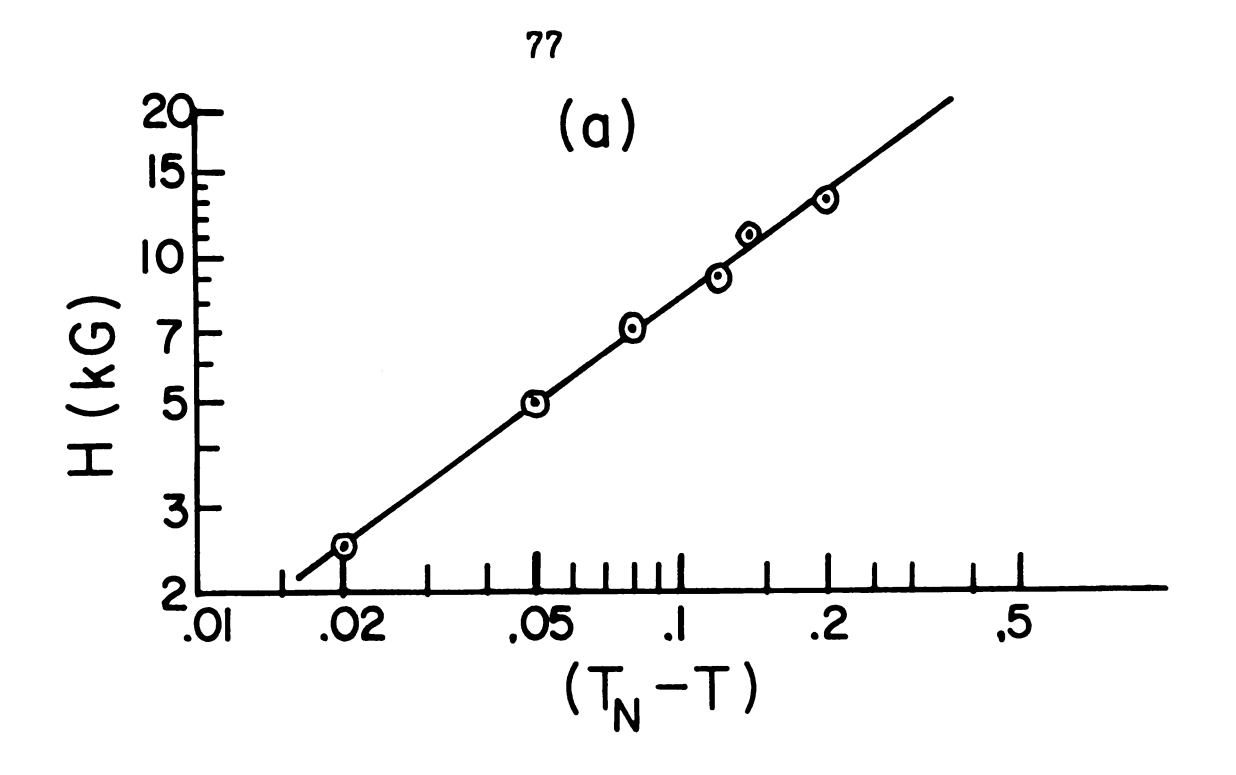
This notion is further substantiated by using the equation of Bienenstock 16 describing the AF-P boundary as

$$T = T_N \left[1 - \left(\frac{H}{H_C} \right)^2 \right]^G$$
, $H_C = \frac{2Sz_1 J_1}{g\mu_B}$, (5.8)

based on a two sublattice model. Plotting $\log \left(\frac{T}{T_N}\right)$ vs. $\log \left[1-\left(\frac{H}{H_C}\right)^2\right]$, as in Fig. 22b, does not give a straight line. However, a line drawn roughly through the points gives G * .02, which is lower than Bienenstock's values of G = .35 and .36 for the simple cubic and bcc lattices respectively. Although the crystal structure of LiCuCl $_3$ ·2H $_2$ O is neither simple cubic nor bcc, the difference given above can not be accounted for merely on the basis of crystal structure.

2. Field Perpendicular to the Easy Axis

With the external field aligned along the b axis and perpendicular to the c'axis, there are four data



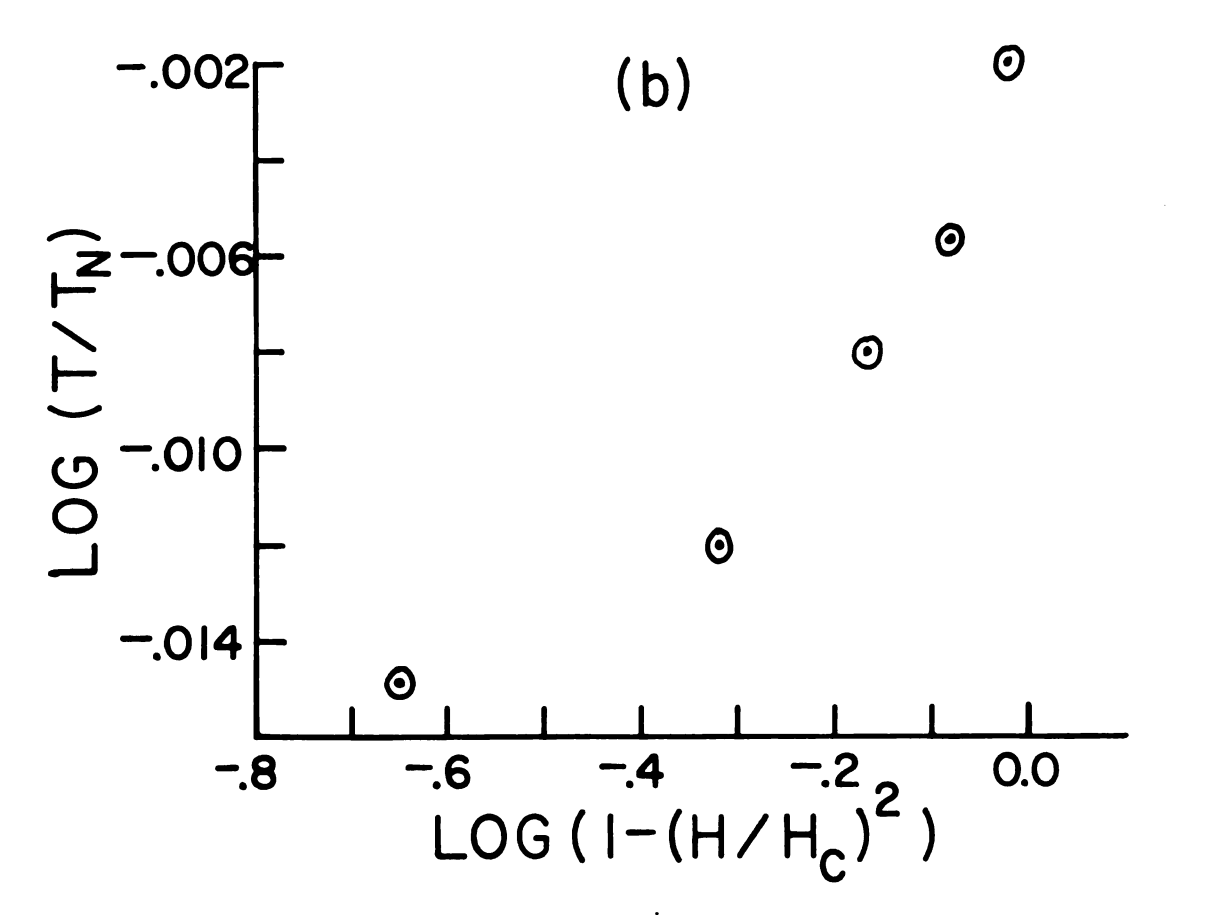


Figure 22. LiCuCl₃·2H₂O log-log plots for AF-P boundary.

points (see Fig. 19) which can be approximately fit by

$$(4.39 - T) = .54 \times 10^{-9} H^2.$$
 (5.9)

The ratio of this coefficient to that for the field parallel is 0.4. From equations 2.50 and 2.51 we would have expected a ratio of 0.33.

However, for the field perpendicular to both the b and c'axes, an approximate fit gives,

$$(4.42 - T) = 0.04 \times 10^{-9} H^2.$$
 (5.10)

Thus it would appear from this brief evidence that the anisotropy in these two directions is not similar (see 3.23 and 3.26). Consequently the assumption of tetragonal symmetry about the easy axis may not be valid for LiCuCl₃·2H₂0, so that a modification in the original equations might be necessary.

D. Antiferromagnetic-Spin Flop Boundary

The AF-SF boundary has a slight curvature and can be fit to the equation,

$$H = 9.36 + 0.078 T + 0.173 T^{2}$$
. (5.11)

This boundary intersects the paramagnetic boundary at the triple point, 4.2°K and 12.7 kG. The zero temperature intercept is 9.36 kG $(H(0)_{SF-AF})$. Equation 1.22,

 $H(0)_{SF-AF} = (2H_EH_A + H_A^2)^{1/2}$, enables one to calculate an anisotropy field (H_A) of 3100 gauss. Expressing the anisotropy field as a temperature gives,

$$T_A = \frac{\mu_B^H A}{k} = 0.21$$
°K. (5.12)

This is comparable to the temperature depression by the external field of the AF-P boundary at the triple point. This suggests that equation 2.44 is valid for $\operatorname{LiCuCl}_3 \cdot 2\operatorname{H}_20$ much closer to T_N than has been assumed. Such a difference also indicates that the anisotropy plays a larger role in $\operatorname{LiCuCl}_3 \cdot 2\operatorname{H}_20$ than originally expected. A more detailed comparison would require a modification of equation 2.51, so that the anisotropy is taken into account more explicitly.

E. Spin Flop-Paramagnetic Boundary

A linear least squares fit to T vs. H² gives,

$$T = 4.323 - 0.654 \times 10^{-9} H^2,$$
 (5.13)

with H in gauss. The zero temperature intercept is 81.5 kG, and the zero field intercept is 4.323°K. The latter temperature depression is expected on the basis of the molecular field approximation. Furthermore, one would expect that the spin flop case should be similar to the case with the field perpendicular to the easy axis, save for the anisotropy energy. One finds that the coefficient,

 0.654×10^{-9} , is not much different than the coefficient, 0.54×10^{-9} , in equation 5.9 which represents the case of the external field perpendicular to the easy axis and along the b axis.

F. Anisotropy Energy

The anisotropy energy per unit volume can be found from 1.17,

$$H_{AF-SF} = [2K/(X_{\perp}-X_{||})]^{1/2}.$$

From a plot of magnetization vs. external field, 17 the susceptibilities at 1.4°K are,

$$(X_1 - X_{\parallel}) = (.026 - .0078) \text{ emu/mole} = .0182 \text{emu/mole}.$$
(5.14)

Using the density of .0113 mole/cc, this can be expressed as 2.06×10^{-4} emu/cc. Since the spin flop field is 9.7 kG, the anisotropy energy is therefore,

$$K = 9700 \text{ ergs/cc.}$$
 (5.15)

An alternative calculation can be made for K using l.6 and l.12, where λ can be written as $1/\chi$. Then,

$$K = H_E H_A \chi_{\perp}. \tag{5.16}$$

Using χ =.000294 emu/cc, one obtains K=11400 ergs/cc, which is in reasonable agreement with 5.15.

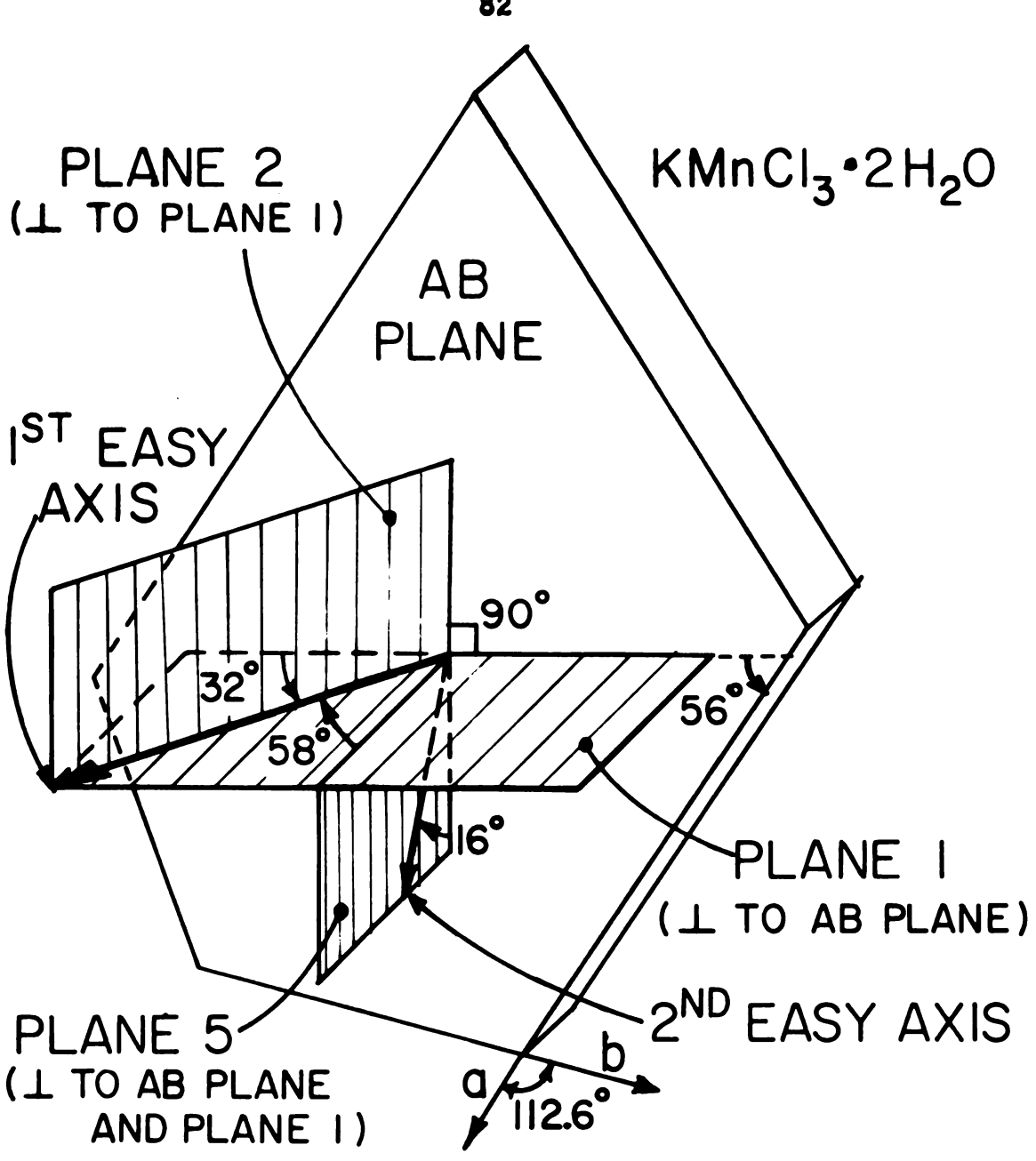
VI. KMnCl₃2H₂0 RESULTS

A. Adiabatic Rotations

The first crystal tried was twinned, as is not uncommon for these crystals. 11 Performing magnetic rotations in plane 1 (see Fig. 23), two temperature minima were observed in the AF state (Fig. 24 and Table 8 of Appendix), corresponding to two magnetization axes about 70° apart. At a field of 12.5 kG (Fig. 24), each minimum is replaced by a relative maximum which indicates that the spins have flopped within the plane of rotation. At 18 kG, this spin flopping effect disappears (Fig. 25 and Table 8 of Appendix).

Rotating in plane 2 (see Fig. 23), an orientation that was obtained from plane 1 by rotating 90° about the easy axis, there is only one minimum in the AF state, as expected (Fig. 26 and Table 9 of Appendix). Moreover, at 13 kG and 15 kG (Fig. 26 and Table 9 of Appendix) the rounded minimum becomes flattened, which indicates that the spins may have flopped normal to the plane of rotation (Chapter I, Part D).

It was desirable to check these results by using a single crystal. Using x-ray diffraction, a crystal was



PLANE 3 IS 1 TO IST EASY AXIS PLANE 4 CONTAINS 1st AND 2nd **EASY AXES**

Figure 23. KMnCl₃·2H₂0 crystal with rotation planes.

Figure 24. KMnCl₃·2H₂0 plane 1 isentropic rotations -twin.

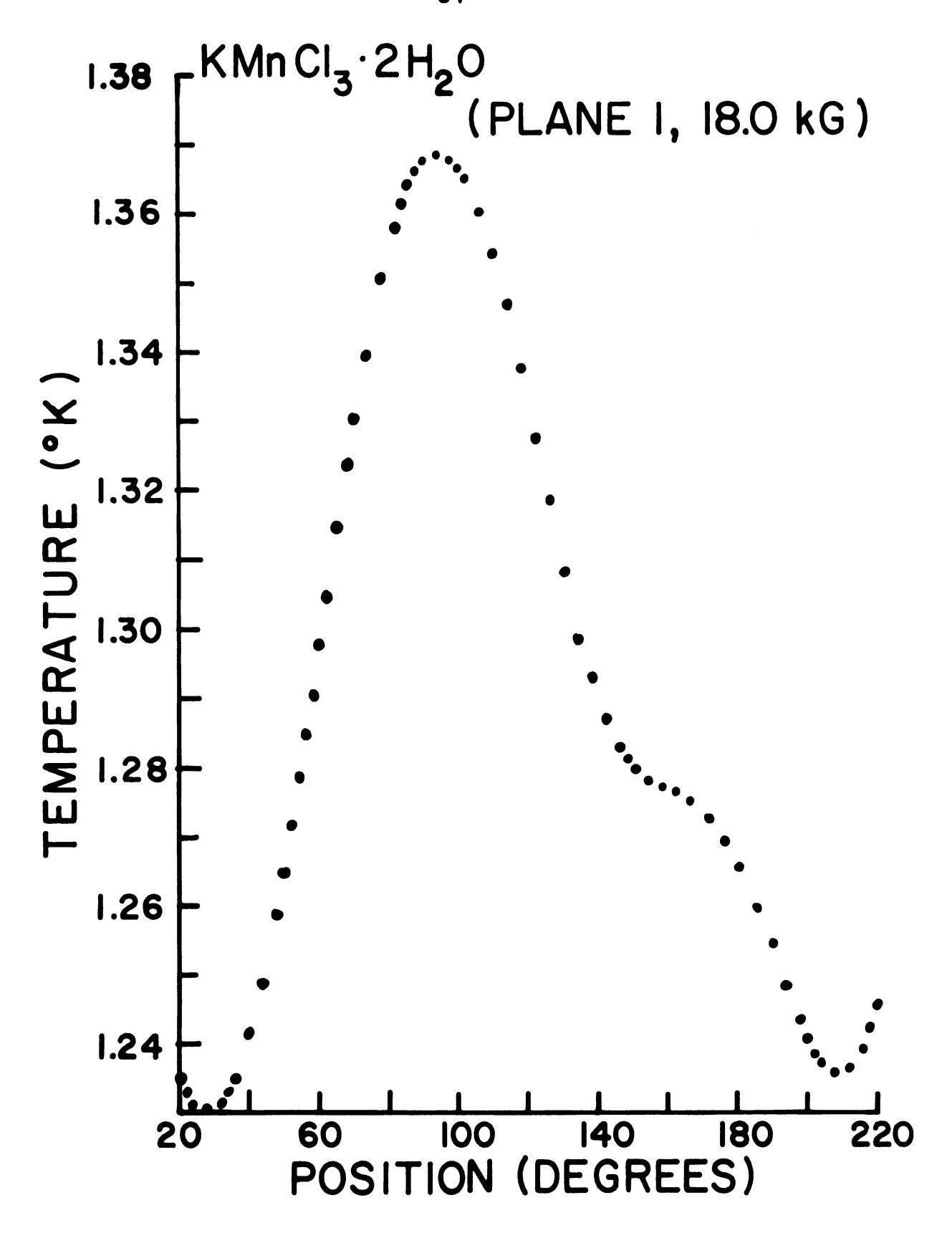


Figure 25. KMnCl₃·2H₂0 plane 1 isentropic rotation - twin.

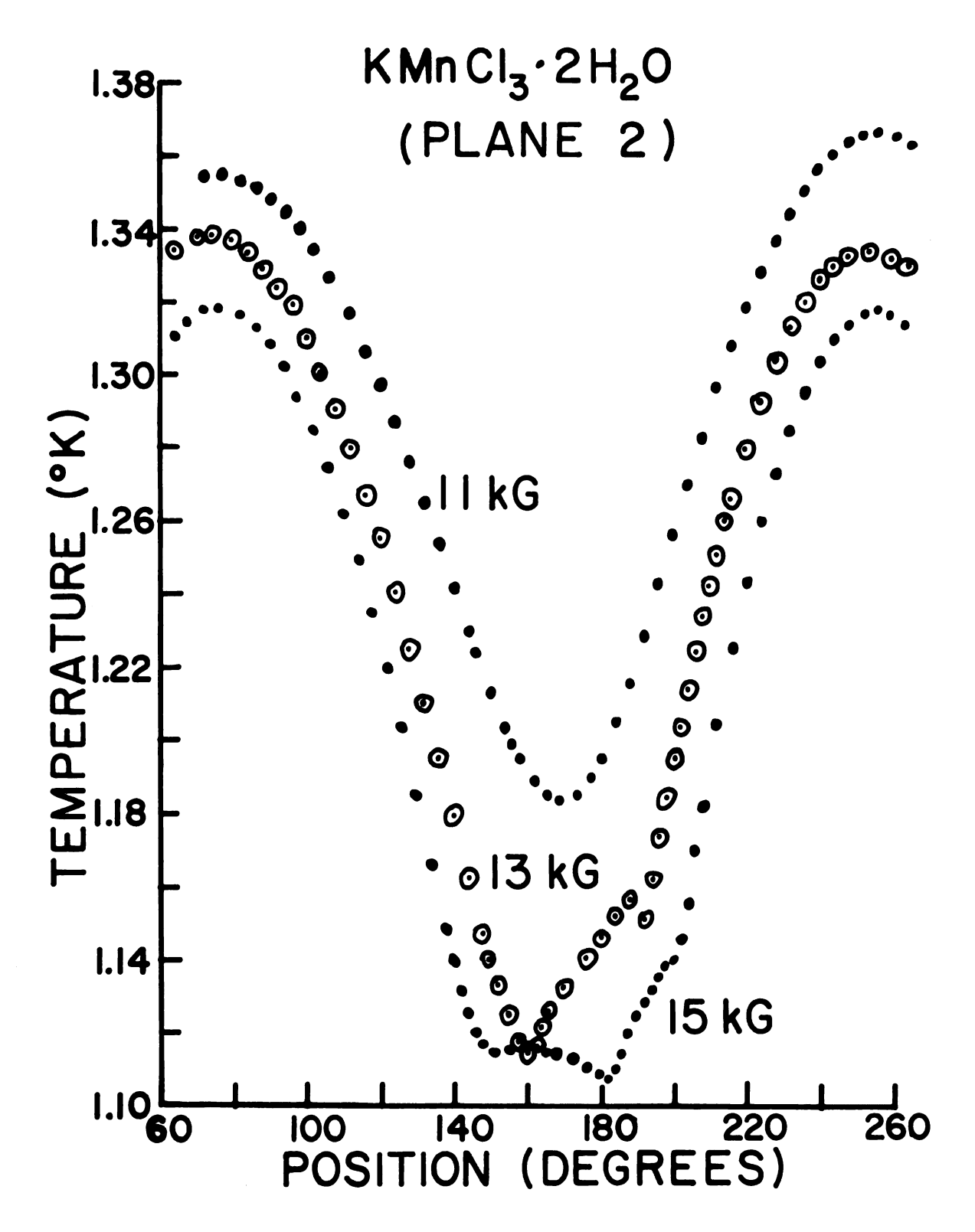


Figure 26. KMnCl₃·2H₂0 plane 2 isentropic rotations - twin.

found that showed no twinning in plane 1. Now a rotation in plane 1 confirmed that it was single (Fig. 27 and Table 10 of Appendix). There was some evidence of spin flopping in this plane as evidenced by the small hump in the minimum position at 12.3 kG (Fig. 28, and Table 10 of Appendix). As before, the small peak disappears at higher fields. In plane 2 (Fig. 29 and Table 11 of Appendix), there is a small flat region near the easy axis for 18 kG.

When investigating the AF-P perpendicular boundaries, a rotation (Fig. 30 and Table 12 of Appendix) was done in plane 3, which is perpendicular to the easy axis (shown in Fig. 23). The temperature change on rotating is more than could be explained by not having the easy axis quite perpendicular to the rotation plane. This minimum temperature position was designated the second easy axis which was believed to have a lower anisotropy energy than the principal (first) easy axis. This was deduced from the relative temperature changes during the rotations.

The next rotation was in the plane of the first and second easy axes (plane 4 of Fig. 23). These results show a definite peak at the easy axis position at and above 15 kG (Figs. 31, 32, and Table 13 of Appendix). The peak becomes higher and broader as the field increases.

Thus in region B of the magnetic phase diagram (Fig. 33), some of the spins may flop 90° in plane 1 and then do not remain flopped in regions C and D. In region

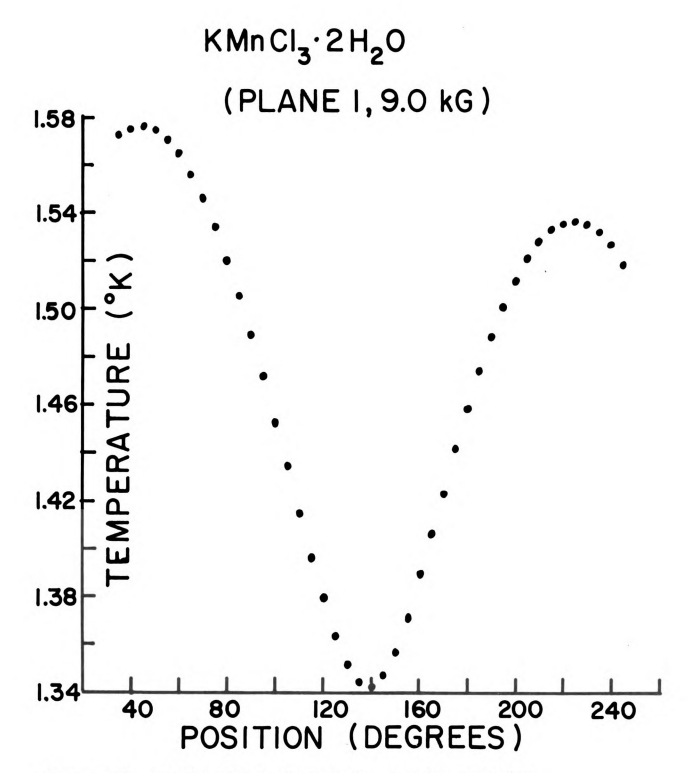
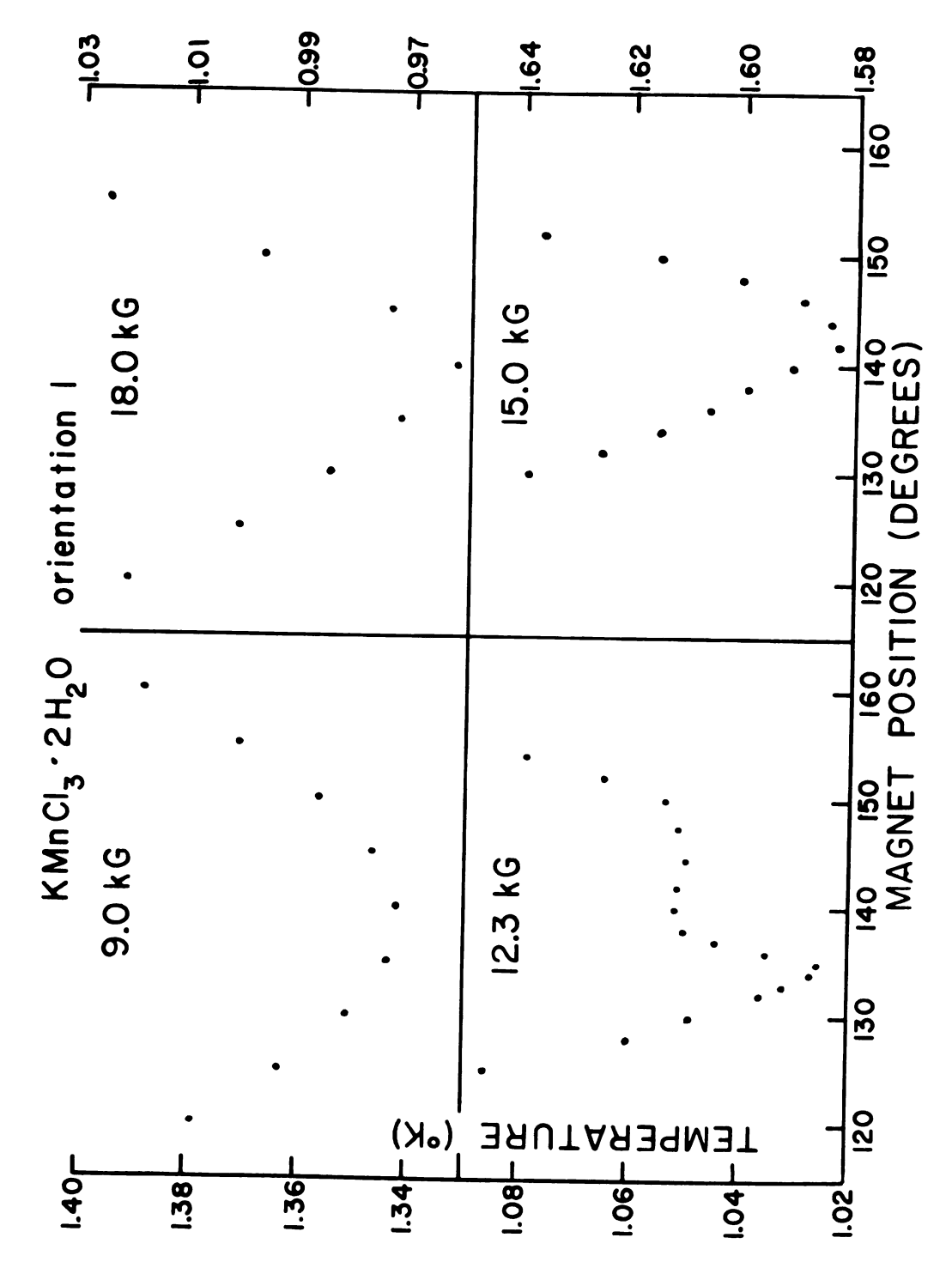


Figure 27. KMnCl₃·2H₂0 plane 1 isentropic rotation - single.



KMnCl3.2H20 plane 1 isentropic rotations - single. Figure 28.

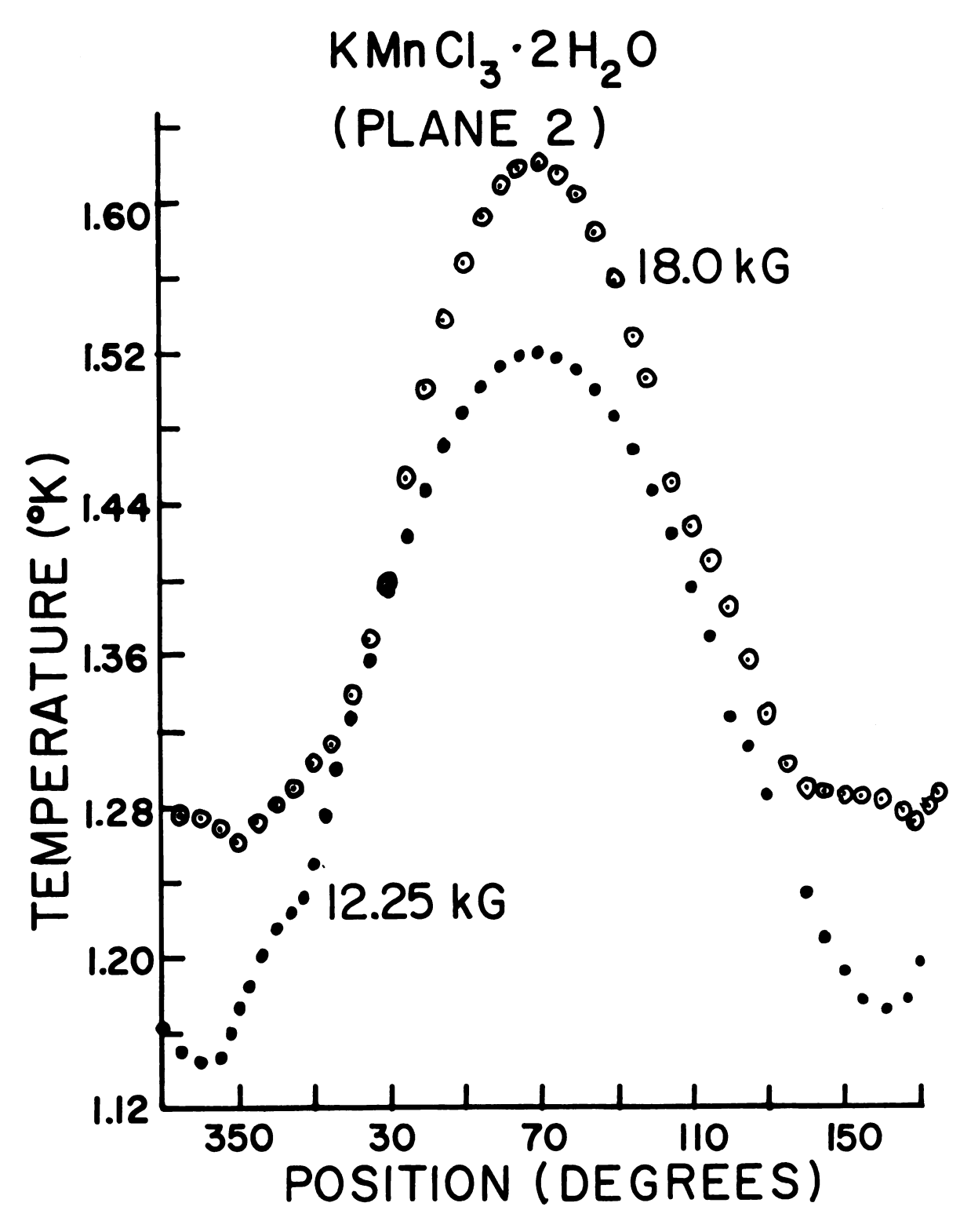


Figure 29. KMnCl₃·2H₂0 plane 2 isentropic rotations - single.

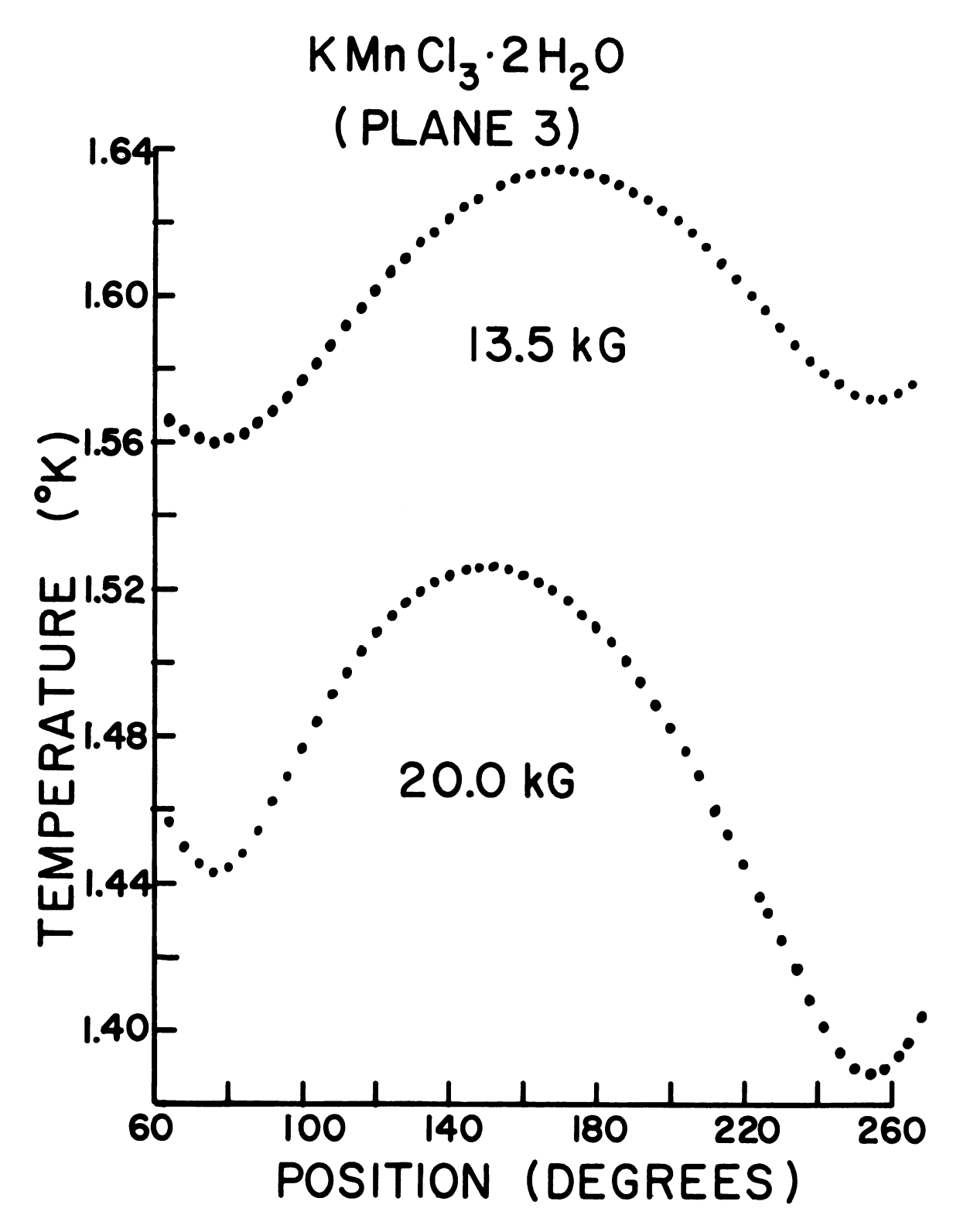


Figure 30. KMnCl₃·2H₂O plane 3 isentropic rotations - single.

KMnCl₃·2H₂O (PLANE 4)

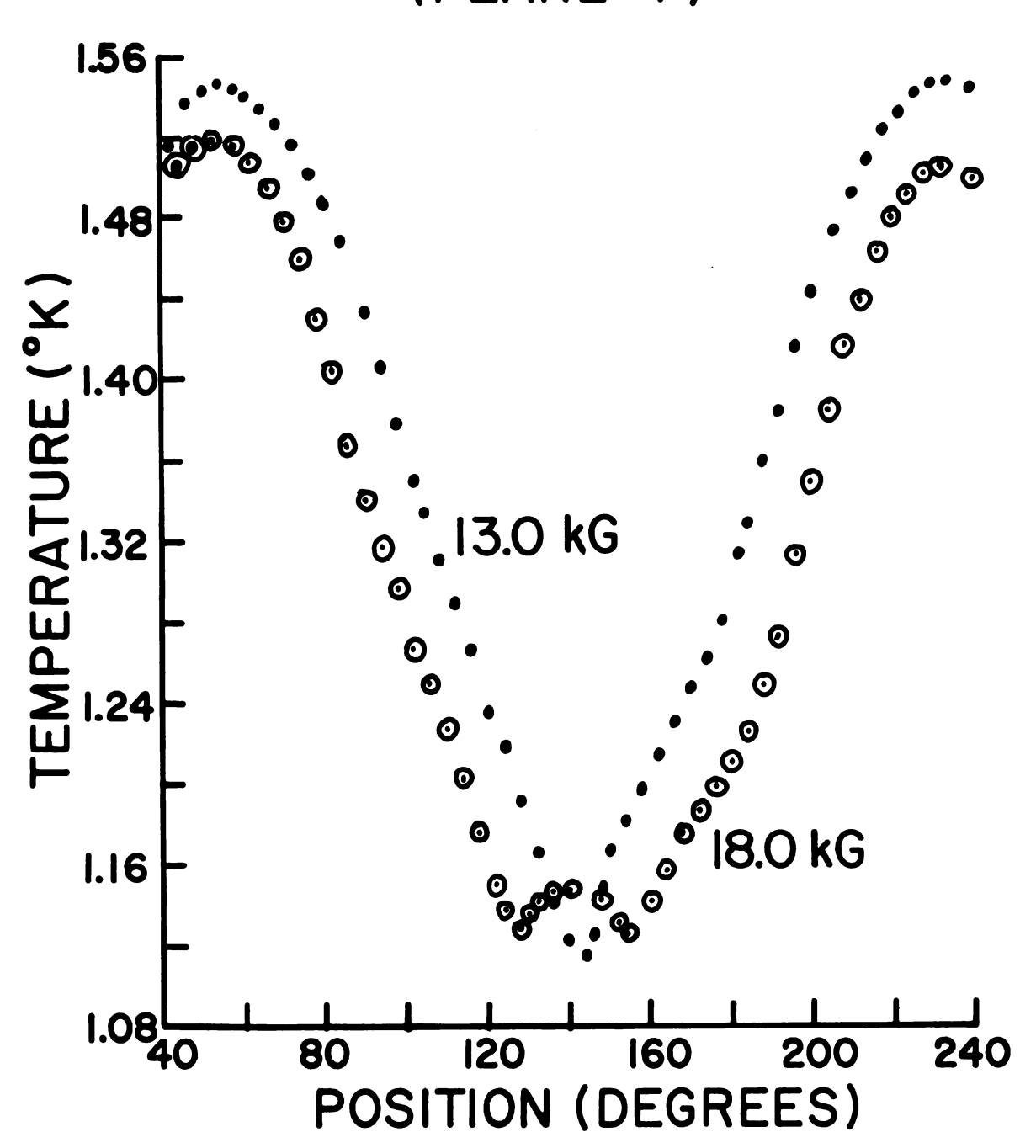


Figure 31. KMnCl₃·2H₂O plane 4 isentropic rotations - single.

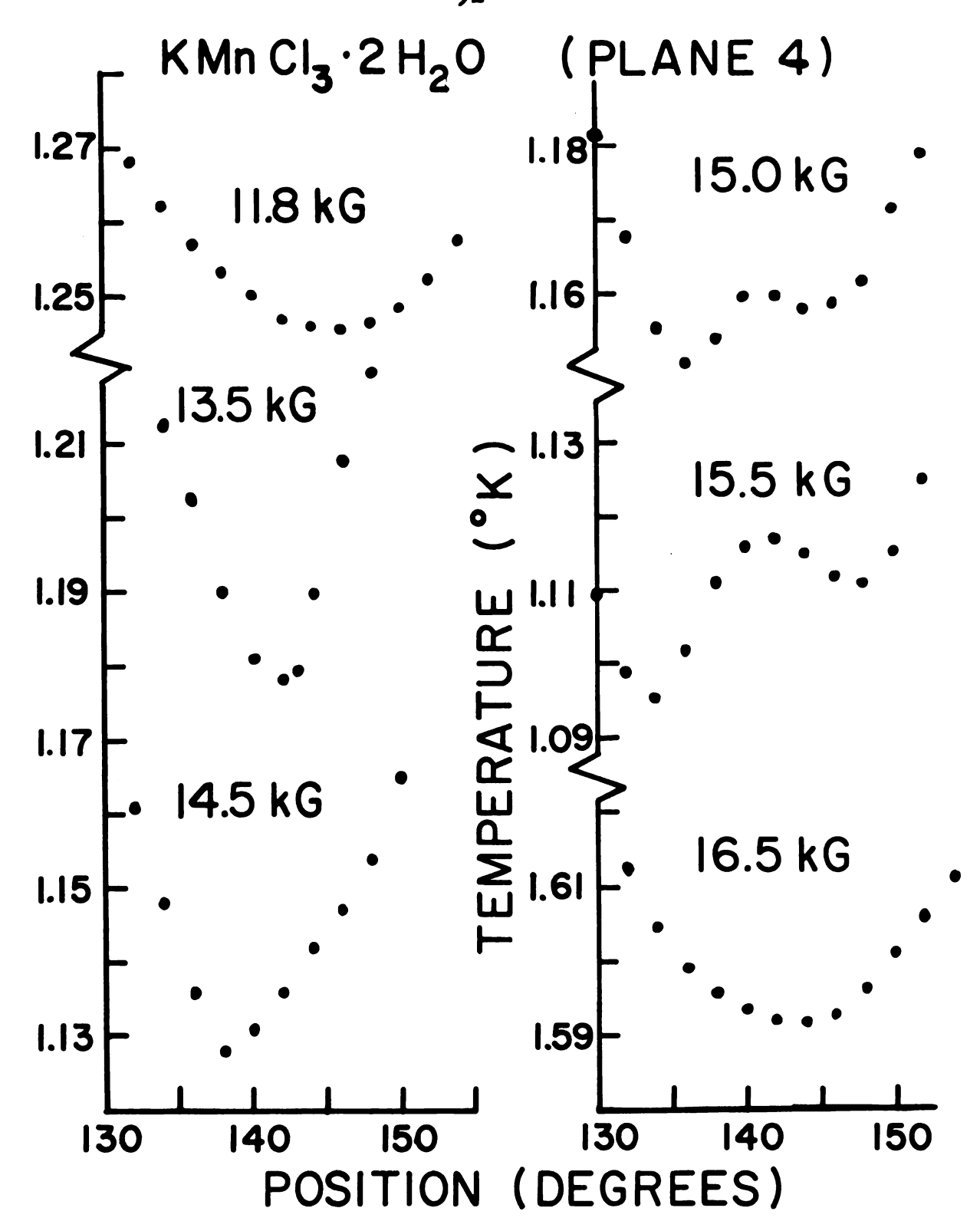


Figure 32. KMnCl₃·2H₂O plane 4 isentropic rotations - single.

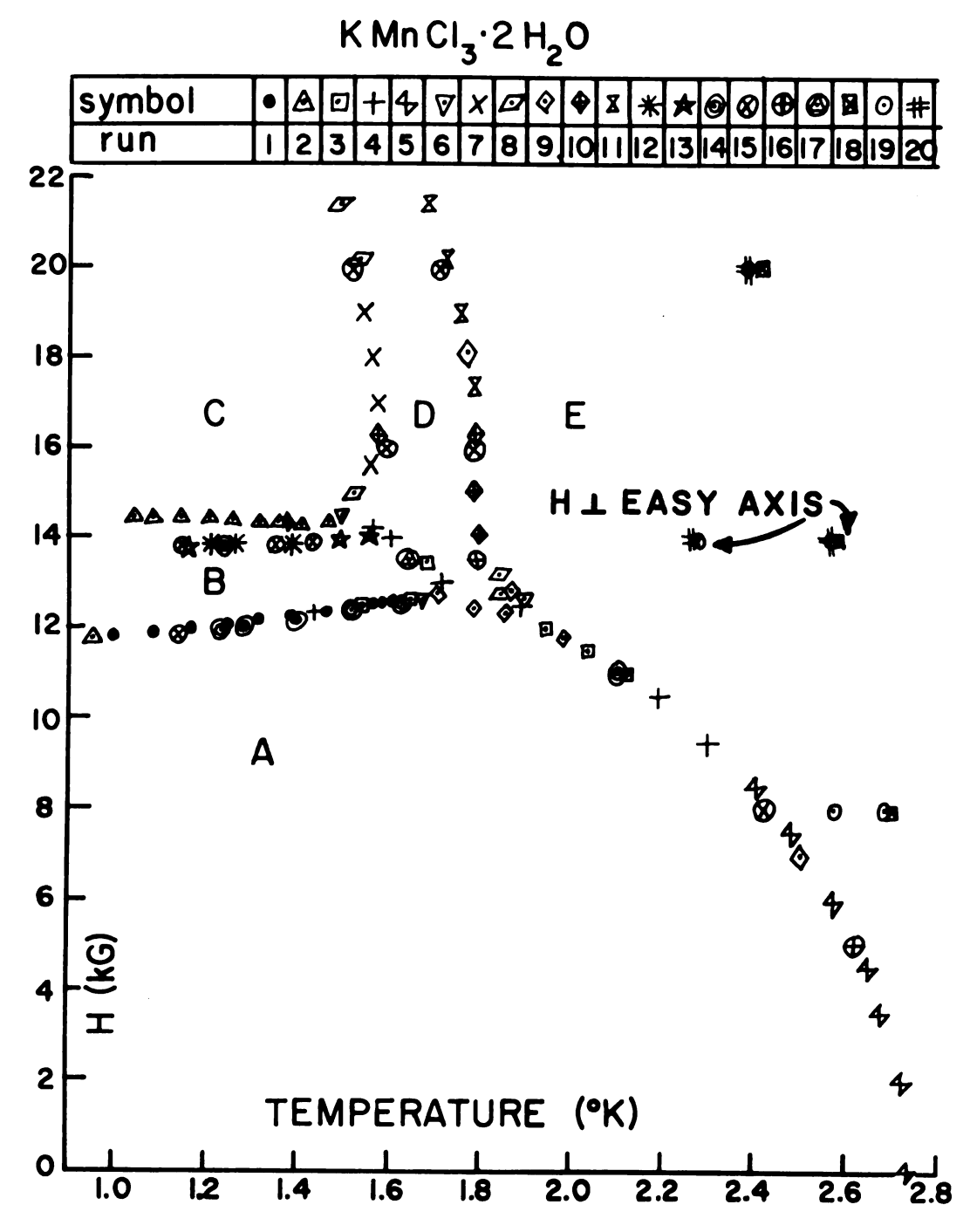


Figure 33. KMnCl₃·2H₂O phase boundaries.

C, some of the spins may flop 90° in plane 4, and then do not show flopping in region D.

B. "Antiferromagnetic-Spin Flop" Boundaries

The boundaries between regions A and B and between B and C are shown in the magnetic phase diagram (Fig. 33 and Tables 14 and 15 of Appendix). Some of the isentropes are shown in Fig. 34 (Table 16 of Appendix). As shown in Fig. 35 (Table 17 of Appendix), the lowest value of H_{C2} (upper boundary) was usually at a different angle than the lowest value of H_{C1} (lower boundary). In Fig. 35a, the isentrope slope change was the sharpest at 137°, and it was not resolvable below 135°. In Fig. 35b, the slope change could not be resolved below 162°.

Corresponding diagrams (Figs. 36, 37 and Table 18 of Appendix) are shown for the twinned crystal. The symmetry of the twin is evidenced by $\rm H_{C2}$ in Fig. 36, as the 140° minimum corresponds to the 224° minimum. In both figures, the two rotation minima at a given field correspond to the $\rm H_{C1}$ curve. Thus the region between rotation minima corresponds to the state B above $\rm H_{C1}$.

As shown in the phase diagram (Fig. 33), the $\rm H_{C2}$ boundary is slightly higher when the angle for lowest $\rm H_{C1}$ was used. By using the best angle for $\rm H_{C2}$, the slightly lower boundary was obtained. All the other boundaries

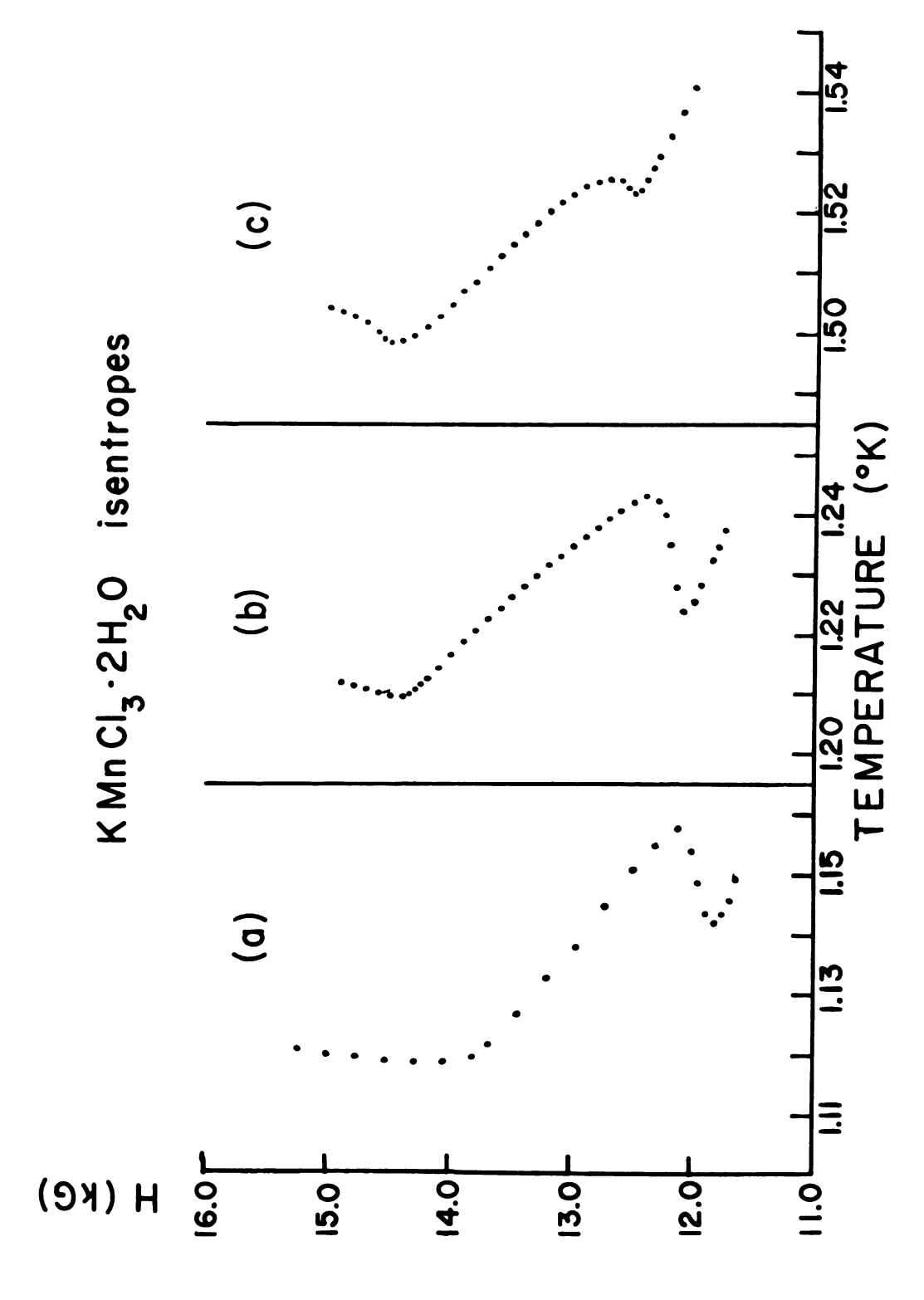


Figure 34. KMnCl3.2H2O isentropic magnetizations.

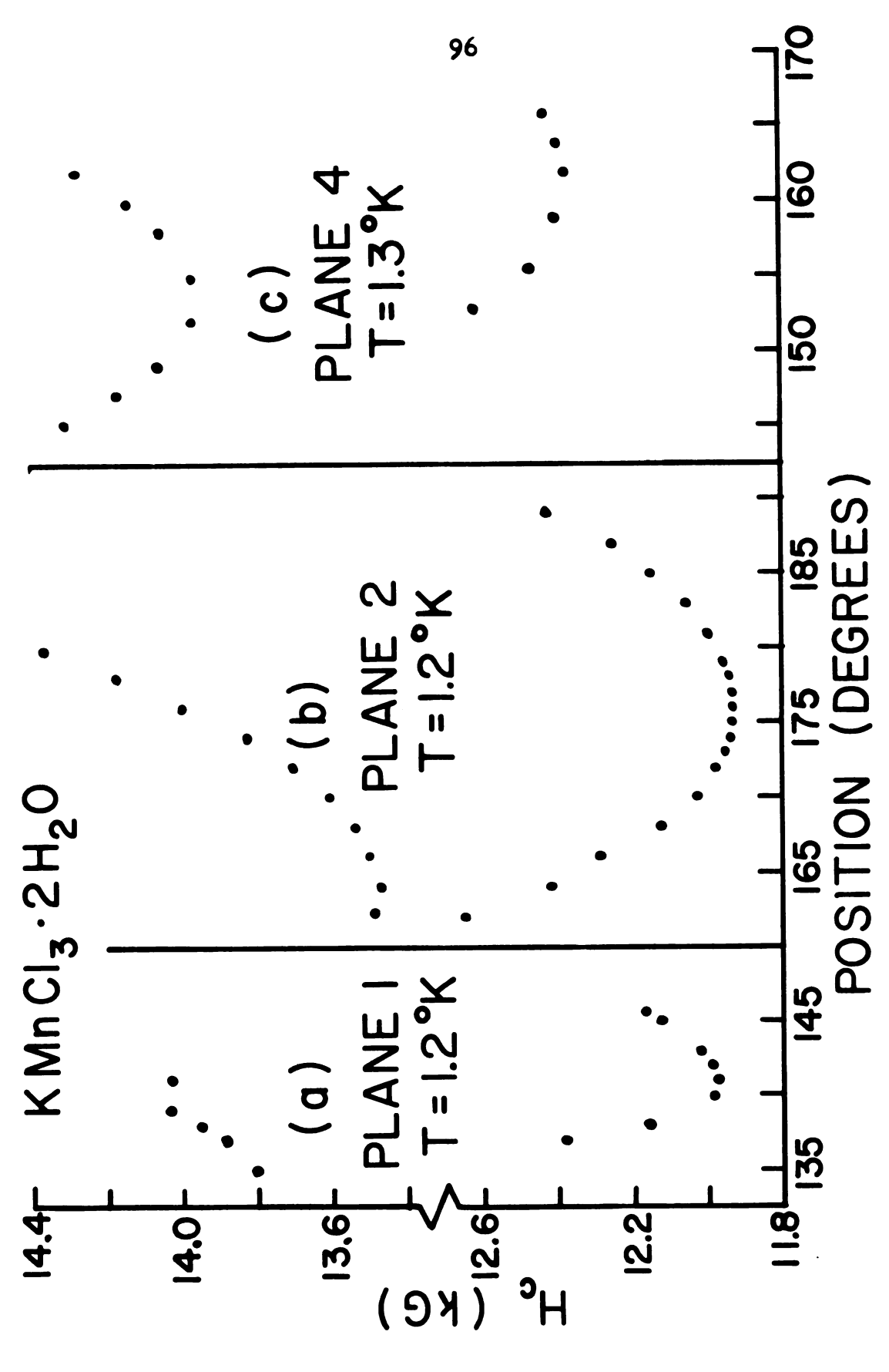


Figure 35. KMnCl $_3$ '2H $_2$ O critical field angular dependence – single.

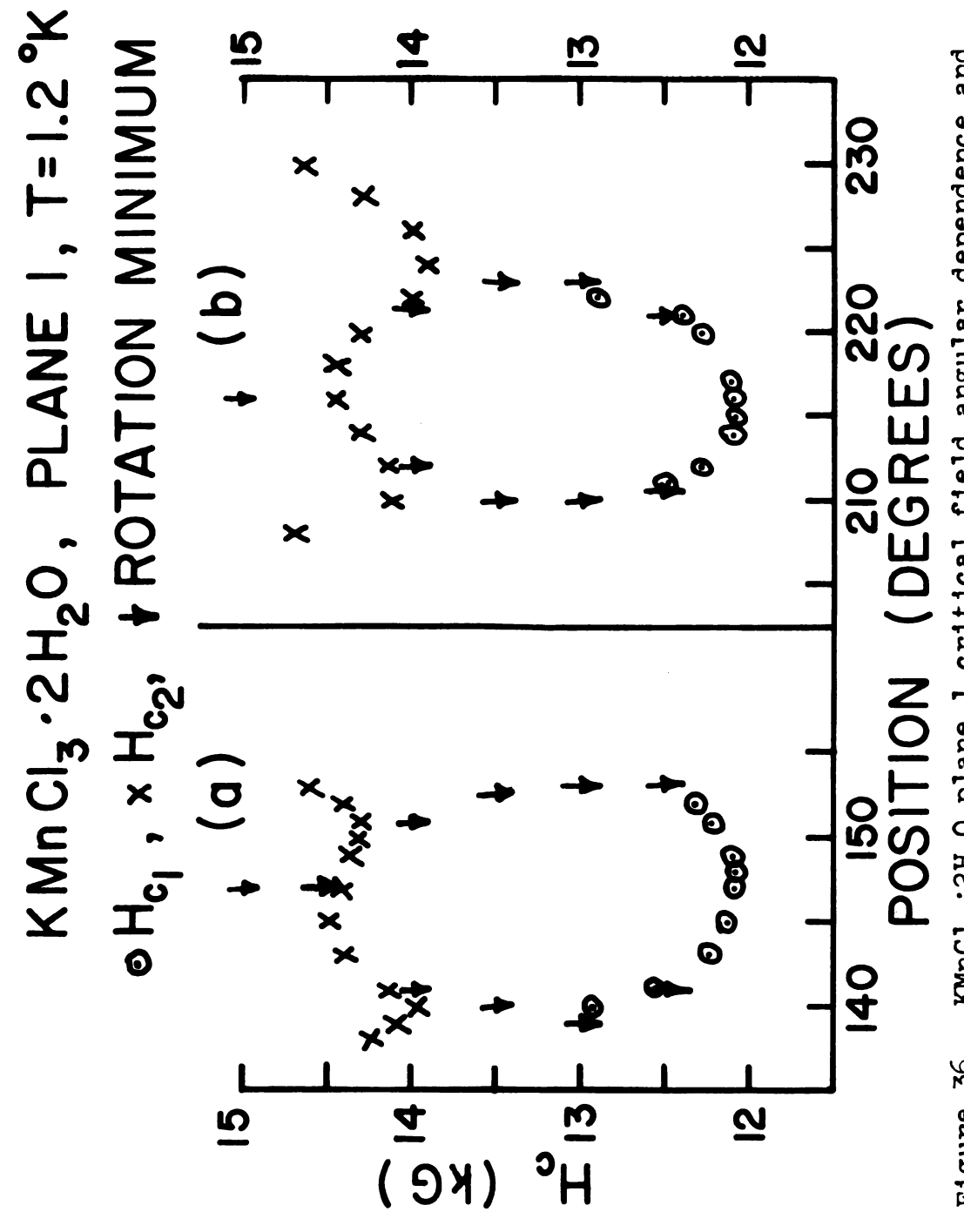


Figure 36. KMnCl3.2H2O plane I critical field angular dependence and rotation minima - twin.

 $KMnCl_3 \cdot 2H_2O$, PLANE 2, T=1.2°K **∤** ROTATION MINIMUM ×H_{c2}, • H_{cl}, 17点 16 15 ××××*** 13 12 150 160 180 190 200 POSITION (DEGREES)

Figure 37. KMnCl₃·2H₂O plane 2 critical field angular dependence and rotation minima - twin.

(for a parallel field) were found using the angle that gave the lowest $H_{\rm Cl}$. They were determined by specific heat measurements as shown in Figs. 38, 39, and Table 19 of Appendix. Runs 1-13 are for the twin crystal, and runs 14-20 are for the single one (Fig. 33).

C. Easy Axis Shift and Dipolar Anisotropy

It is also unusual that the rotation minimum in the AF state does not correspond to the best angle for $H_{\rm cl}$ or $H_{\rm c2}$ (Fig. 40 and Table 17 of Appendix). It was thought possible that the nylon sample holder might be twisting due to the magnetic torque on the crystal. However, after making a sample holder about ten times as strong (Fig. 9), identical results were found. The rotation minimum was 16° from the angle for lowest $H_{\rm cl}$ in plane 4.

The dipolar anisotropy (Chapter III, B) predicts that the easy axis shift on going from state A to B would be equal to the B-C shift, but would be the reverse of the C-D or D-E shifts. Looking at the rotation minima and maxima for plane 4 (Figs. 32, 40), the A-B shift is -4° and likewise for the B-C shift. One then might expect a + 4° shift for C-D, but a +5.5° shift is observed.

However, the best angles for H_{cl} and H_{c2} are relatively far away from these minima. Also, the angular shifts of the other orientations do not follow a pattern

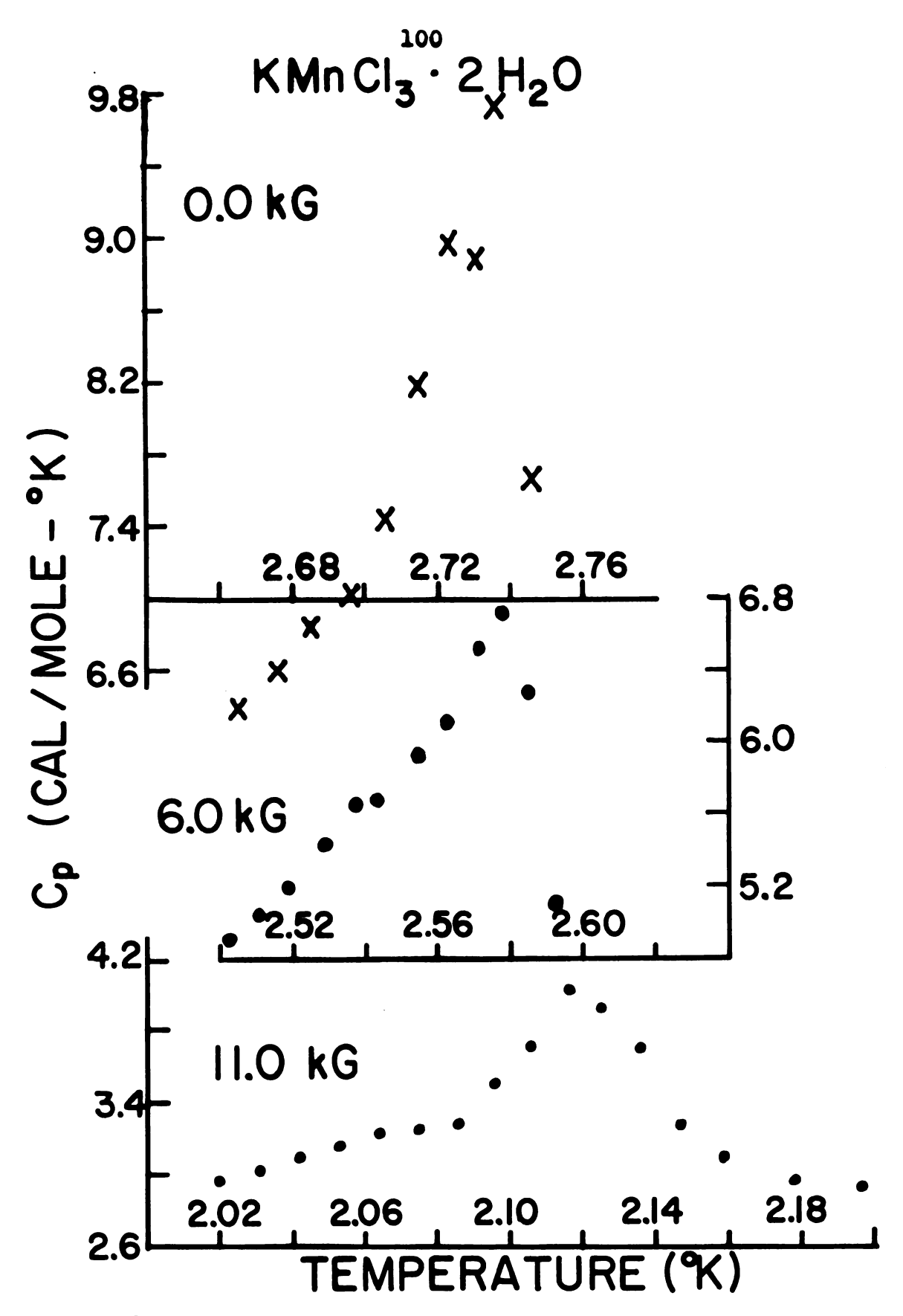


Figure 38. KMnCl₃·2H₂O specific heat data - twin.

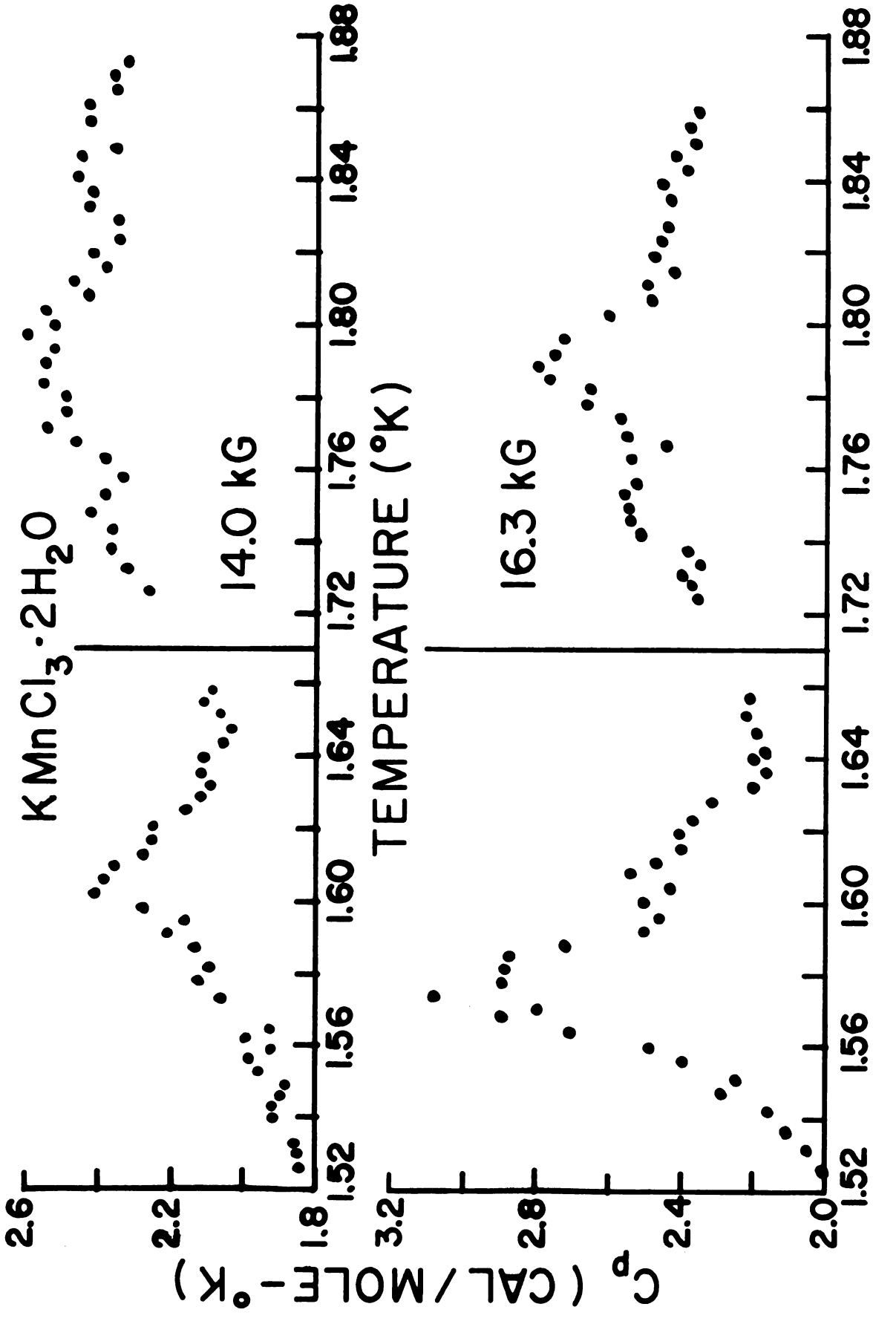


Figure 39. KMnCl₃·2H₂O specific heat data - twin.

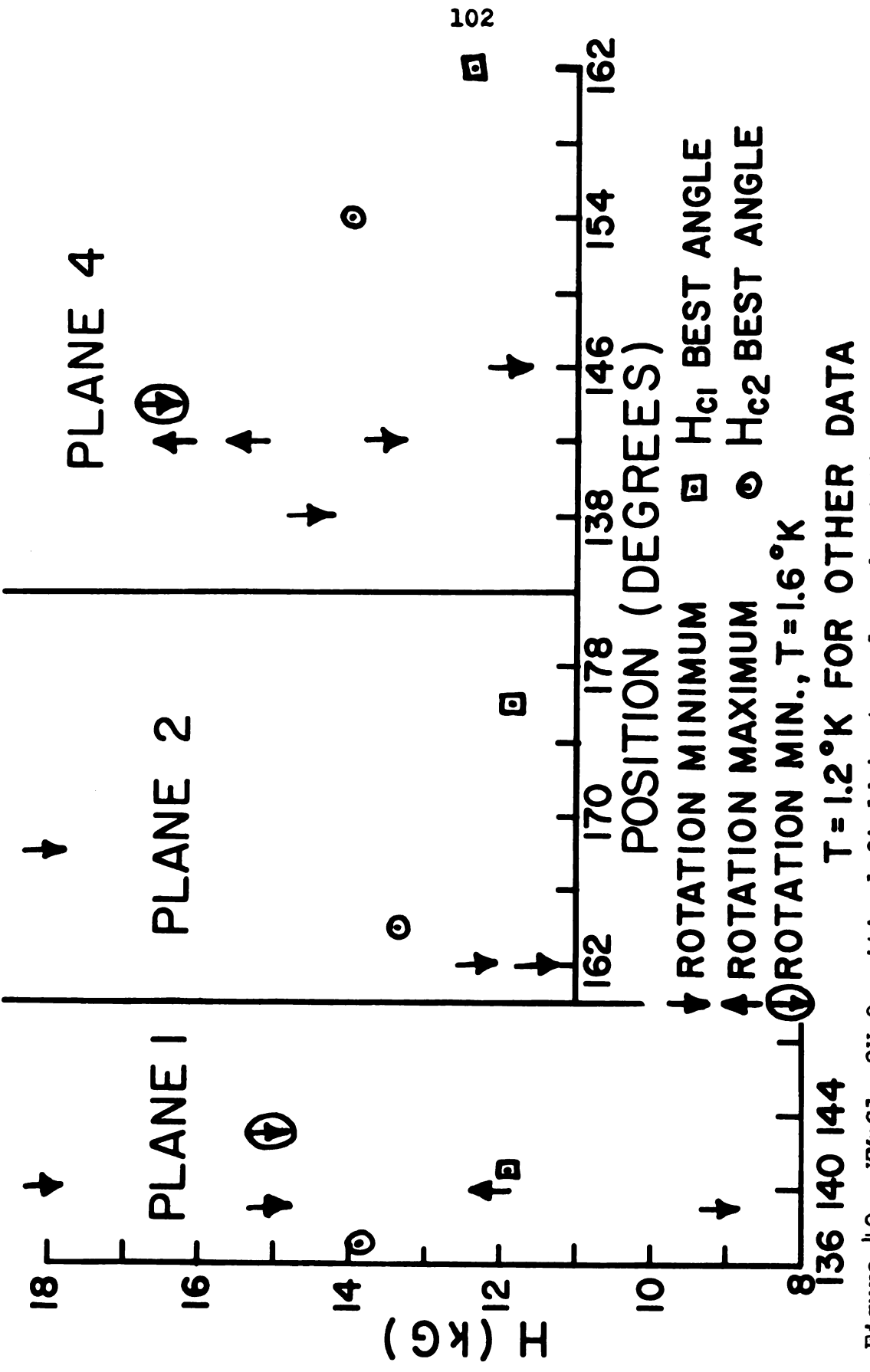


Figure 40 . KMnCl $_3$ ·2H $_2$ O critical field best angle and rotation extrema — single.

predicted by dipolar anisotropy. There must be another reason why the best angles for ${\rm H_{cl}}$ and ${\rm H_{c2}}$ do not coincide with the rotation minima.

One explanation is that the observed rotation minimum is the result of the superposition of minima from both the first and second easy axes. It is possible that the second easy axis is not exactly perpendicular to the first easy axis as was assumed. Then the second easy axis could slightly shift the rotation minimum from the actual position of the first easy axis. However, the critical field, H_{Cl}, should still have its best angle at the first easy axis.

The effect should be most pronounced in the plane of the first and second easy axes (plane 4), and it should be a minimum when the second easy axis makes the greatest angle with the plane of rotation (thus its projection on the plane would coincide with the first easy axis).

Surprisingly the results concur, as there is a 16° shift from the rotation minimum to the best angle for H_{Cl} in plane 4 (Fig. 40). Moreover, there is a 2° shift in plane 1, which can be approximately obtained from plane 4 by rotating 90° about the first easy axis. Plane 2, which is obtained from plane 1 by rotating exactly 90° about the first easy axis (and is thus not very different from plane 4), shows a 14° shift for the same case.

One could conclude that the best angles for H_{cl} and H_{c2} locate the first easy axis. Then the dipolar (or other) angle shift is given by these two angles.

D. Antiferromagnetic-Paramagnetic and "Spin Flop-Paramagnetic" Boundaries

The AF-P boundary can be compared to Foner's calculation 10 for a two sublattice Heisenberg model which assumes an anisotropic interaction that is very small compared to the exchange interaction and assumes that the intrasublattice exchange interaction is negligible compared to the intersublattice interaction. With the field parallel to the easy axis, the boundary is

$$T_N - T = (2S^2 + 2S + 1) g^2 \mu_B^2 H^2/(40 k^2 T_N)$$
 (6.1)

(H in kG), which is similar to equation 2.51. Experimentally, a least squares fit gives $T = 2.76 - .0053 \text{ H}^2$.

With the field perpendicular to the easy axis, the curvature predicted from equation 2.51 or 3.33 is 1/3 of equation 6.1, or $T_N - T = .0010 \text{ H}^2$. The fit to the data is $T = 2.74 - .00087 \text{ H}^2$ which is reasonably close. An Ising model (3.37) predicts $T_N - T = .0041 \text{ H}^2$.

Another more curved perpendicular boundary appears only when the field is near the second easy axis direction, and this boundary is absent when the field is perpendicular

to this axis. This indicates a non-uniaxial anisotropy component (equation 3.26) as did the rotation (Fig. 30) with the first easy axis perpendicular to the rotation plane. Since there are two perpendicular boundaries, this may suggest the existence of two different sets of sublattices, which might explain the two different "AF-SF" boundaries (H_{Cl} and H_{C2}).

As mentioned in section E of Chapter I, the paramagnetic boundaries can be observed as an inflection point in the isentrope. This was checked at different fields as shown in Fig. 41a, b (Table 20 of Appendix). There was some doubt about the boundary between D and A since specific heat points did not show a peak there. The run 9 isentropes (Fig. 41c, d) did give the points between A and D at 12.34 kG and 12.45 kG as shown on the phase diagram (Fig. 33). This method gives somewhat more uncertainty in the field value than do the specific heat points, but the temperature uncertainty is about the same.

E. Exchange and Anisotropy Fields

In order to calculate the exchange fields, one must extrapolate the boundaries to find their values at T=0. A straight line was found to give a good fit and the best extrapolation for the boundaries for A-B and B-C. The values at T=0 are, $H_1=10.5$ kG and $H_2=13.2$ kG.



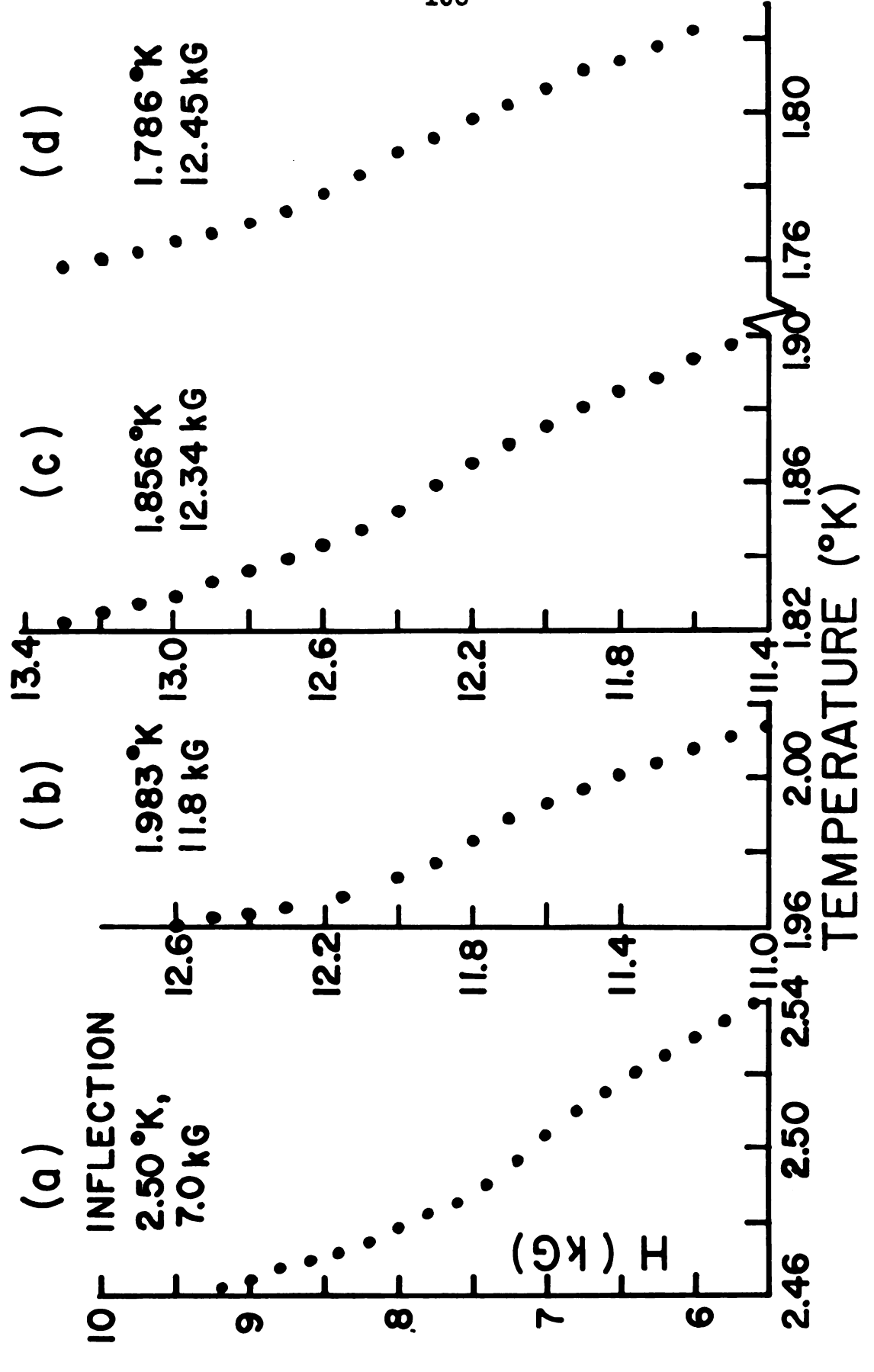


Figure 41. KMnCl3.2H20 isentropic magnetizations.

In order to examine the T = 0 separation of the C-D and D-E boundaries, the extrapolation was done using the curvature of the AF-P perpendicular boundary. Molecular field theory suggests that the SF-P boundary can be approximated by this boundary's curvature since the curvature is inversely proportional to the exchange constant (3.33), or directly proportional to X_{\perp} , where $X_{\perp} = X_{\rm SF}$ for small anisotropy (1.16). Also, from the experimental data, the perpendicular boundary's curvature approximates the curvature of the two boundaries above 17 kG. The resulting intercepts are $H_3 = 46.2$ kG and $H_4 = 48.8$ kG.

The theory suggests that $H_2 - H_1 = H_4 - H_3$. The above results show 2.7 kG and 2.6 kG for these differences which appear to confirm equation 3.14. The exchange fields are calculated using 3.15. This gives

$$H_{E1} = 16.5 \text{ kG}, H_{E2} + H_{E3} = 14.8 \text{ kG}, H_{E4} = 1.3 \text{ kG}.$$
(6.2)

Since H_{El} is the largest of the exchange fields, one might possibly expect a broad peak in the specific heat at a slightly higher temperature than T_N , representing a disordering of the intradimer spin alignment, as occurs with the vertex linked chain in $CsMnCl_3 \cdot 2H_20$. ¹⁸ However, no such anomaly was observed up to $6.8^{\circ}K$, ¹⁹ although it is possible that such an anomaly may occur at even higher temperatures. Moreover, a calculation from

this specific heat data showed that the entropy associated with the magnetic transition at T_N is within 1% of the expected value for a spin 5/2 manganese ion. This implies that if an anomaly is present, it is a rather shallow one to account for this additional 1% of entropy.

It would seem that the intradimer ordering occurs at T_N and that H_{E1} is the same order of magnitude as the sum of the interdimer exchange fields (H_{E2}, H_{E3}, H_{E4}) as expected from equation 6.2. In addition, Spence has indicated that the coordination octahedra of the dimer are similar to those of $MnC1_2 \cdot 2H_20$ in which the spins are antiparallel within the dimer. Thus he concludes that the exchange within the dimer is quite small. Since the 16.5 kG value found for H_{E1} is not a very large exchange field, it may be that such an explanation is valid for the present sample.

By setting $E_A = E_E$ (equations 3.2, 3.6), the zero temperature value for the AF-P boundary is $2(H_{E2} + H_{E3}) = 29.6$ kG (assuming that regions B, C, and D do not exist). The same value is found for the small boundary between B and D by setting $E_B = E_D$ (assuming that C does not exist). Experimentally, the AF-P boundary is fit by $T = 2.76-.00533H^2$, giving $H_{AE}(T=0) = 22.8$ kG. From a least squares fit to the higher field points of the other boundary, one obtains $T = 2.61 - .00522 H^2$, which gives $H_{BD}(T=0) = 22.4$ kG.

These intercepts are not very different, as the theory predicts, although they are somewhat lower than predicted.

The very unusual magnetic phase diagram for KMnCl₃·2H₂O certainly indicates a rather complicated spin flopping arrangement. The above analysis is clearly a first approximation attempt to understand this behavior. The fact that the Ising model with an eight sublattice structure at O°K gives reasonable agreement with the boundary separations may or may not be fortuitous. The author realizes that additional considerations for the case of non-axial symmetry may perhaps be a bit more fruitful in a more complete understanding of the magnetic behavior of this compound.

CONCLUSIONS AND SUGGESTIONS FOR FURTHER WORK

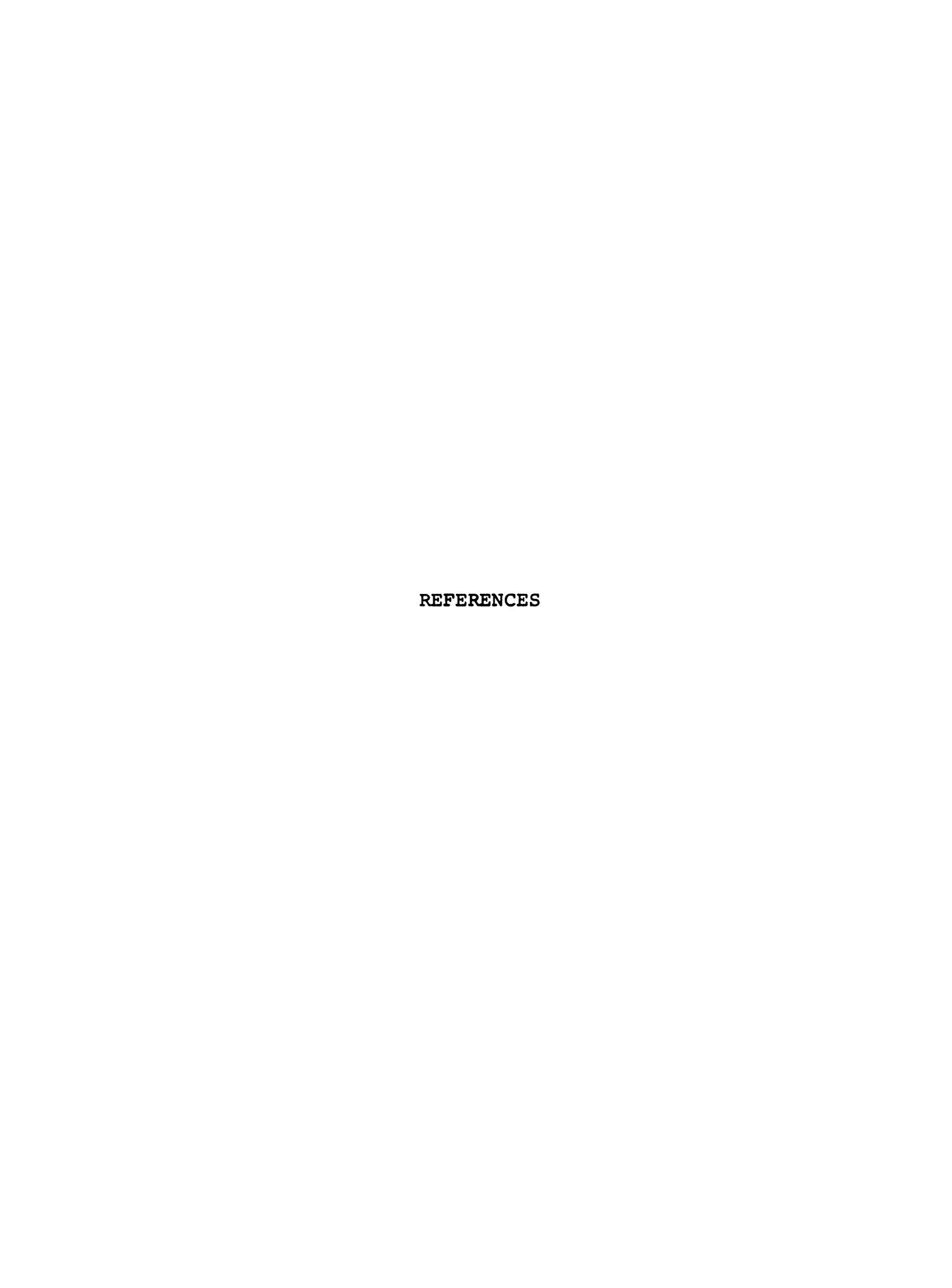
The magnetic phase diagrams of two new compounds have been studied. For LiCuCl₃·2H₂0, a single AF-SF boundary has been observed, as well as information on both the inter- and intrasublattice exchange constants. For KMnCl₃·2H₂0, a very unusual phase diagram has been observed. This compound appears to pass through several magnetic phases. A first approximation to understanding this behavior has been made by assuming an eight sublattice model with an Ising type interaction at 0°K.

Some new techniques have been used for mapping out a magnetic phase diagram. One is to use isentropic magnetizations to find the second order AF-P or SF-P boundary at regions where they make relatively small angles with the temperature axis, since the specific heat peak may not be resolvable in this case. Another is to check the easy axis position by using a sensitive gaussmeter to find the critical spin flop field at different angles near the rotation minimum. This is essential for a crystal like KMnCl₃·2H₂0 which has the lowest critical field at a position that is 16° from the rotation minimum in one plane.

The more accurate method of crystal alignment with a cathetometer was used primarily for changing the orientation slightly between runs. An improved sample rotator with at least one axis of rotation that could be rotated while in the calorimeter would be very helpful so that one could bring the easy axis closer to the rotation plane of the magnet in the event of a poor alignment.

Either specific heat or magnetic susceptibility measurements should be made at higher fields for both crystals to get a better approximation to the zero temperature intercepts of the paramagnetic boundaries. A more direct comparison between the theory and the experiment could thus be effected.

Zero field susceptibility measurements for parallel and perpendicular directions in both crystals could give more insight into the anisotropy which does not appear to be uniaxial. Field dependent susceptibility measurements should be made on LiCuCl₃·2H₂0, for which our results in one plane show a decrease in the critical field and less distinct temperature minima in the isentropes when the field direction is varied from the easy axis position. It would be interesting to observe any changes in the critical field and in the resolution of the peak in the susceptibility vs. field at these different angles.



REFERENCES

- 1. A. H. Morrish, The Physical Principles of Magnetism (Wiley, 1965).
- 2. J. N. McElearney, Ph.D. Dissertation, Michigan State University (1968).
- 3. J. H. Schelling and S. A. Friedberg, Phys. Rev. <u>185</u>, 728 (1969).
- 4. J. Skalyo, Jr., A. F. Cohen, S. A. Friedberg, and R. B. Griffiths, Phys. Rev. 164, 705 (1967).
- 5. P. H. Vossus, L. D. Jennings, and R. E. Rundle, J. Chem. Phys. 32, 1590 (1960).
- 6. P. Heller, Phys. Rev. 146, 403 (1966).
- 7. M. Date and K. Nagata, J. Appl. Phys. 34, 1038 (1963).
- 8. R. D. Spence, J. Chem. Phys. (to be published).
- 9. T. Oguchi, J. Phys. Soc. Japan 20, 2236 (1965).
- 10. Y. Shapira and S. Foner, Phys. Rev. B. $\underline{1}$, 3083 (1970).
- 11. J. W. Mellor, A Comprehensive Treatise on Inorganic and Theoretical Chemistry, 12, 367 (1932).
- 12. F. G. Brickwedde, H. van Dijk, M. Durieux, J. R. Clement, and J. K. Logan, J. Res. Nat. Bur. Stand. 64A, 1 (1960).
- 13. G. T. Armstrong, J. Res. Nat. Bur. Stand., <u>53</u>, 263 (1954).
- 14. J. R. Clement and E. H. Quinnel, Rev. Sci. Instr. 23 213 (1952).
- 15. H. Forstat and D. R. McNeely, J. Chem. Phys. <u>35</u>, 1594 (1961).
- 16. A. Bienenstock, J. Appl. Phys. 37, 1459 (1966).

- 17. S. C. Abrahams and H. J. Williams, J. Chem. Phys. 39, 2923 (1963).
- 18. R. D. Spence and K. V. S. Rama Rao, J. Chem. Phys. 52, 2740 (1970).
- 19. H. Forstat, J. N. McElearney and P. T. Bailey, Phys. Lett. 27A, 549 (1968).



Table 1. LiCuCl₃·2H₂0 AC plane isentropic rotations.

θ	T (°K)	θ	T (°K)	θ	T(°K)
4/24/70	9.0 kG	4/24/70	9.0 kG	4/24/70	12.0 kG
52	1.6330	192	1.6075	184	1.5822
56	1.6333	196	1.6129	182	1.5803
60	1.6331	200	1.6182	180	1.5791
64	1.6321	204	1.6230	178	1.5794
68	1.6306	208	1.6279	174	1.5827
72	1.6285	212	1.6319	170	1.5865
76	1.6257	218	1.6362	166	1.5894
80	1.6224	224	1.6397	162	1.5919
84	1.6189	228	1.6410	158	1.5941
88	1.6150	234	1.6417	152	1.5957
92 06	1.6106	236	1.6417	148	1.5969
96	1.6058	240 244	1.6413	144	1.5974
100 104	1.6009 1.5951	244	1.6402 1.6384	140 136	1.5964 1.5933
104	1.5895	240	1.0304	132	1.5933
112	1.5842			129	1.5838
116	1.5780	4/24/70,	12 0 kG	126	1.5872
120	1.5728	4/24/10,	12.0 KG	122	1.5985
124	1.5671	250	1.6533	118	1.6102
128	1.5620	246	1.6543	116	1.6164
132	1.5573	242	1.6547	112	1.6257
136	1.5537	238	1.6542	108	1.6352
140	1.5506	234	1.6527	104	1.6434
144	1.5487	230	1.6506	100	1.6519
148	1.5483	226	1.6477	96	1.6482
152	1.5493	222	1.6439	92	1.6639
156	1.5516	218	1.6395	88	1.6684
160	1.5554	214	1.6347	84	1.6726
164	1.5601	210	1.6293	80	1.6753
168	1.5659	206	1.6233	76	1.6777
172	1.5728	202	1.6161	72	1.6792
176	1.5792	198	1.6093	68	1.6796
180	1.5867	194	1.6016	63	1.6792
184	1.5932	190	1.5933	60	1.6780
188	1.5999	186	1.5861	56	1.6763
				52	1.6734

Table 2. LiCuCl₃·2H₂0 BC' plane isentropic rotations.

θ	T (°K)	θ	T(°K)	θ	T (°K)
4/30/70	9.0 kG	4/30/70	11.0 kG	4/30/70,	12.0 kG
2	1.6250	108.0	1.5673	105	1.5756
5	1.6252	108.5	1.5668	106	1.5749
10	1.6253	109.0	1.5665	107	1.5744
15	1.6244	109.5	1.5663	108	1.5744
20	1.6238	110.0	1.5661	109	1.5748
25	1.6223	110.5	1.5663	110	1.5759
30	1.6204	111.0	1.5665	111	1.5750
35	1.6183	111.5	1.5669	112	1.5747
40	1.6155	112.0	1.5676	113 114	1.5749
45	1.6124	4 /20 /70	11 2 60	114	1.5755 1.5764
50	1.6090	4/30/70,	11.2 KG	112	1.5/64
55 60	1.6054	112 0	1 5604	4/30/70,	13.0 kG
60 65	1.6015 1.5971	113.0 112.5	1.5694 1.5690	4/30/70,	13.0 KG
70	1.5929	112.0	1.5685	114	1.5828
75	1.5881	111.5	1.5683	112	1.5824
80	1.5824	111.0	1.5681	110	1.5827
85	1.5774	110.5	1.5681	109	1.5827
90	1.5714	110.0	1.5686	108	1.5827
95	1.5650	109.5	1.5686	107	1.5829
100	1.5584	109.0	1.5684	106	1.5833
103	1.5537	108.5	1.5684	105	1.5839
105	1.5509	108.0	1.5688		
107	1.5486	107.5	1.5692		
109	1.5475				
111	1.5484	4/30/70,	11.5 kG		
113	1.5513	, , , , , , , , ,			
115	1.5560	105.0	1.5722		
120	1.5672	106	1.5713		
125	1.5778	107	1.5706		
130	1.5858	108	1.5703		
135	1.5946	109	1.5708		
140	1.5996	110	1.5719		
145	1.6051	111	1.5705		
150	1.6099	112	1.5706		
155	1.6137	113	1.5712		
160	1.6173	114	1.5720		
165	1.6203	115	1.5731		
170	1.6219				
175	1.6236				
180	1.6247				
185	1.6251				
190	1.6253				
195	1.6250				
200	1.6241				

Table 3. LiCuCl₃·2H₂0 isentropic magnetizations.

H (kG)	T(°K)	H(kG)	T(°K)	H(kG)	T(°K)
4/20/70	AC plane	4/24/70	AC plane	4/30/70,	BC' plane
8.65	1.0753	13.00	2.3791	11.00	3.5059
8.70	1.0748	12.60	2.3786	11.10	3.5047
8.80	1.0742	12.20	2.3779	11.20	3.5038
8.90	1.0736	11.80	2.3768	11.30	3.5031
9.00	1.0732	11.40	2.3754	11.40	3.5023
9.10	1.0728	11.00	2.3740	11.50	3.5017
9.20	1.0726	10.80	2.3732	11.60	3.5015
9.25	1.0725	10.60	2.3727	11.70	3.5009
9.30	1.0725	10.40	2.3728	11.80	3.5011
9.35	1.0725	10.30	2.3732	11.90	3.5011
9.40	1.0726	10.20	2.3738	12.00	3.5009
9.45	1.0727	10.00	2.3757	12.10	3.5008
9.50	1.0729	9.80	2.3781	12.20	3.5007
9.55	1.0731	9.60	2.3804	12.30	3.5015
9.60	1.0735	9.40	2.3829	12.40	3.5009
		9.20	2.3856	12.50	3.5008
4/21/70,	AC plane	9.00	2.3885	12.60	3.5012
9.10	1.5791	4/24/70,	AC nlane	4/20/70	BC' plane
		4/24/10,	AC plane	4/30/70,	bc prane
9.20 9.30	1.5776 1.5763	9.00	3.0894	11.50	3.7678
9.40	1.5751	9.40	3.0855	11.60	3.7659
9.50	1.5741	9.80	3.0817	11.70	3.7643
9.60	1.5733	10.20	3.0784	11.80	3.7638
9.70	1.5727	10.40	3.0768	11.90	3.7631
9.80	1.5726	10.60	3.0752	12.00	3.7622
9.90	1.5729	10.80	3.0742	12.10	3.7619
10.00	1.5736	11.00	3.0730	12.20	3.7622
10.10	1.5746	11.20	3.0723	12.30	3.7621
10.20	1.5759	11.30	3.0722	12.40	3.7619
11.30	1.5775	11.50	3.0722	12.40	3.7019
11.40	1.5790	11.70	3.0723		
11.50	1.5806	11.90	3.0726		
11.60	1.5820	12.30	3.0732		
11.70	1.5833	12.60	3.0732		
11.80	1.5844	12.00	3.0733		
10.89	1.5855				
11.00	1.5863				

Table 4. LiCuCl₃·2H₂0 specific heat data.

T(°K)	Cp	T(°K)	c _p	T(°K)	Cp
4/23/70	0.0 kG	4/21/70,	9.0 kG	4/23/70,	17.0 kG
4.145	1.488	4.069	1.312	4.056	1.508
4.175	1.830	4.099	1.347	4.068	1.537
4.307 4.318	1.820 2.120	4.129 4.163	1.529 1.548	4.087 4.103	1.581 1.537
4.316	2.120	4.196	1.670	4.119	1.614
4.373	2.161	4.226	1.651	4.127	1.514
4.386	2.259	4.253	1.950	4.134	1.672
4.404	2.388	4.284	2.088	4.148	1.822
4.429	1.569	4.322	1.656	4.162	1.721
4.456	1.318	4.359	1.272	4.175	1.751
	2.020	4.408	1.257	4.195	1.323
		4.453	1.209	4.216	1.102
4/21/70,	5.0 kG	4.501	1.187	4.235	1.037
-,, ,				4.255	1.200
4.018	1.348			4.269	1.137
4.053	1.362	4/22/70,	13.0 kG		
4.080	1.376				
4.112	1.422	3.930	1.423	4/23/70,	21.0 kG
4.141	1.414	3.981	1.660		
4.152	1.429	4.019	1.582	3.851	1.405
4.177	1.441	4.054	1.866	3.873	1.422
4.210	1.832	4.087	1.712	3.898	1.490
4.251	1.713	4.129	1.673	3.911	1.471
4.286	1.897	4.163	1.744	3.928	1.581
4.317	1.855	4.201	1.892	3.945	1.587
4.345	2.129	4.235	1.540	3.962	1.656
4.377	1.875	4.272	1.233	3.971	1.868
4.418	1.349	4.319	1.184	3.990	1.658
4.452	1.306			4.005	1.903
4.495	1.345			4.023	1.777
				4.041	1.563
				4.058 4.071	1.378 1.285
				4.071	1.314
				4.113	1.314
				4.113	T. 2TO

Table 5. LiCuCl₃·2H₂0 isentropic magnetization critical fields.

Sample 1		Sample 2		Sam	Sample 3	
T(°K)	H(kG)	T(°K)	H(kG)	T(°K)	H(kG)	
4/20/70	AC plane	5/8/70	AC plane	6/10/70	BC' plane	
1.079	9.49	1.235	9.66	1.370	9.65	
1.110	9.52	1.510	9.82	1.550	9.89	
1.240	9.62	1.850	10.01	1.770	10.07	
1.360	9.66	2.170	10.26	2.270	10.44	
1.450	9.72	2.800	10.81	2.950	10.90	
1.610	9.82	3.170	11.65	2.980	11.00	
1.833	10.00	3.510	11.90			
2.210	10.27	3.920	12.50			
2.560	10.58			6/5/70,	AC plane	
3.000	11.32					
		5/18/70,	BC' plane	3.422	11.88	
				3.426	11.87	
4/21/70,	AC plane	1.180	9.85	3.760	12.30	
		1.600	10.08	4.060	12.80	
1.574	9.82	2.120	10.38			
2.020	10.12	2.600	10.76			
2.380	10.47	3.090	11.20			
		3.440	11.60			
		3.630	11.80			
4/22/70,	AC plane	3.800	11.90			
		3.930	12.30			
2.290	10.43	4.090	12.35			
2.640	10.75					
2.910	11.17					
3.164	11.80	5/20/70,	BC' plane			
		1.180	9.77			
4/30/70,	BC' plane	1.610	10.13			
	-	2.590	10.80			
1.204	9.95	3.410	11.53			
1.414	10.07					
1.600	10.17					
1.566	10.13					
3.090	11.20					
3.510	11.65					
3.780	12.10					

Table 6. LiCuCl₃·2H₂0 specific heat maxima - sample 1.

н	easy axis	^H _ eas	y axis
T(°K)	H(kG)	T (°K)	H(kG)
4/21/70		5/27/70 H b axis	
4.284 4.324 4.346	9.0 7.0 5.0	4.23 4.21 4.32 4.41	19.1 15.0 10.0 5.0
4/22/70 4.256 4.201	11.0	H_ b axis	
4.179 4.146 4/23/70	14.0 15.0	4.43 4.42 4.41 4.42	10.0 15.0 19.0 5.0
4.168 4.175 4.107 4.010 4.203 4.385 4.404	16.0 17.0 19.0 21.0 14.5 2.5 0.0		

Table 7. LiCuCl₃·2H₂0 angular dependence of critical field.

BC' plane T = 1.6°K	, C' = 110°	AC plane, C T = 1.1°K	C' = 154°
θ	H (kG)	θ	H(kG)
108 110 112 114 116 118 120	9.68 10.13 9.68 9.38 9.06 8.87 8.70	151.5 153.0 155.0 158.0	9.51 9.49 9.49 9.52

Table 8. KMnCl₃·2H₂0 plane 1 isentropic rotations - twin.

θ	T(°K)	θ	T(°K)	θ	T(°K)
1/29/70,	9.3 kG	1/29/70	9.3 kG	2/10/70,	18.0 kG
280	.9364	100	.9757	220	1.2455
276	.9386	95	.9765	216	1.2396
272	.9391	90	.9754	212	1.2365
268	.9383	85	.9723	208	1.2360
265	.9368	80	.9677	204	1.2371
260	.9329			200	1.2409
255	.9278			194	1.2488
250	.9211	1/29/70,	12.5 kG	190	1.2543
245	.9129			185	1.2596
240	.9042	250	.9799	180	1.2656
235	.8957	245	.9622	176	1.2694
230	.8882	240	.9397	172	1.2723
225	.8823	235	.9158	166	1.2751
220	.8791	230	.8873	162	1.2762
218	.8788	225	.8570	158	1.2769
216	.8790	222	.8378	154	1.2780
214	.8800	221	.8435	150	1.2799
210	.8829	218	.8822	146	1.2828
205	.8895	215	.8864	142	1.2869
200	.8976	210	.8840	138	1.2929
190	.9128	205	.8584	134	1.2986
185	.9190	202	.8738	130	1.3081
180	.9233	200	.8831	126	1.3186
174	.9263	195	.9074	122	1.3273
172	.9268	190	.9246	118	1.3376
170	.9269	184	.9400	114	1.3467
169	.9270	180	.9468	110	1.3542
166	.9267	174	.9496	106	1.3602
164	.9263	170	.9476	100	1.3665
160	.9250	165	.9413	96	1.3683
155	.9233	160	.9317	92	1.3682
150	.9222	155	.9167	88	1.3600
148	.9221	152	.9105	84	1.3613
146	.9222	150	.9145	78	1.3506
144	.9229	148	.9268	74	1.3394
142	.9239	146	.9307	70	1.3300
140	.9252	143	.9350	65	1.3145
135	.9300	142	.9364	60	1.2977
130	.9370	140	.9351	56	1.2846
125	.9453	138	.9241	52	1.2717
120	.9535	136	.9093	48	1.2586
115	.9609	134	.9133	40	1.2416
110	.9684	132	.9227	36	1.2350
105	.9727	130	.9319	32	1.2312
		128	.9427	28	1.2306
		126	.9516	24	1.2313

Table 9. KMnCl₃·2H₂0 plane 2 isentropic rotations - twin.

θ	T (°K)	θ	T (°K)	θ	T(°K)
3/19/70,	11.0 kG	3/19/70	13.0 kG	3/19/70	15.0 kG
		•			
262	1.3650	64	1.3340	264	1.3137
257	1.3662	70	1.3376	256	1.3171
252	1.3653	74	1.3383	248	1.3138
248	1.3637	80	1.3367	240	1.3036
244	1.3603	88	1.3293	232	1.2849
240	1.3562	96	1.3173	224	1.2598
236	1.3504	104	1.3008	216	1.2258
232	1.3446	112	1.2799	208 204	1.1823 1.1563
228 224	1.3363	120 128	1.2548 1.2254	204	1.1460
224	1.3274 1.3182	136	1.1943	200	1.1396
216	1.3078	144	1.1620	196	1.1356
212	1.2963	150	1.1400	192	1.1278
208	1.2829	155	1.1244	188	1.1199
204	1.2701	158	1.1169	184	1.1099
200	1.2566	160	1.1142	182	1.1082
196	1.2428	164	1.1212	180	1.1085
192	1.2290	170	1.1325	176	1.1100
188	1.2162	176	1.1404	172	1.1132
184	1.2048	182	1.1493	168	1.1145
180	1.1951	186	1.1547	164	1.1154
178	1.1905	188	1.1560	160	1.1157
174	1.1857	190	1.1553	156	1.1155
169	1.1834	192	1.1515	152	1.1150
164	1.1864	194	1.1625	148	1.1169
160	1.1919	196	1.1740	144	1.1258
156	1.1992	200	1.1948	140	1.1403
150	1.2128	204	1.2142	134	1.1663
146	1.2245	208	1.2341	126	1.2038
140	1.2417	212	1.2510	118	1.2351
136	1.2535	216	1.2665	110	1.2623
132	1.2648	220	1.2798	102	1.2849
128	1.2762	228	1.3034	94	1.3026
124	1.2870	236	1.3198	86 80	1.3133 1.3176
120	1.2969	244	1.3296	76	1.3176
116 112	1.3067 1.3166	254 264	1.3338 1.3297	76 72	1.3179
106	1.3272	204	1.3431	72 67	1.3144
100	1.3341			0 /	T. 7744
98	1.3400				
94	1.3445				
90	1.3485				
86	1.3517				
82	1.3535		*		
77	1.3547				
72	1.3540				
					

Table 10. KMnCl₃·2H₂0 plane 1 isentropic rotations - single.

θ	T(°K)	θ	T(°K)
8/27/70	9.0 kG	8/31/70	12.3 kG
35	1.5726	154	1.0795
40	1.5747	150	1.0535
45	1.5754	145	1.0503
50	1.5741	140	1.0515
55	1.5705	138	1.0500
60	1.5646	136	1.0350
65 70	1.5560	135	1.0255
70 75	1.5459	133	1.0320
75 80	1.5338 1.5206	130 125	1.0510 1.0858
85	1.5053	123	1.0030
90	1.4890		
95	1.4714	8/31/70	18.0 kG
100	1.4524	J, J2, J3	
105	1.4342	120	1.0217
110	1.4145	125	1.0020
115	1.3960	130	0.9855
120	1.3790	135	0.9727
125	1.3632	140	0.9626
130	1.3510	145	0.9743
135	1.3440	150	0.9975
140 145	1.3422 1.3468	155	1.0256
150	1.3566		
155	1.3712	8/31/70	15.0 kG
160	1.3885	0, 01, 10	2310 110
165	1.4060	152	1.6368
170	1.4226	150	1.6156
175	1.4420	148	1.6008
180	1.4586	146	1.5897
185	1.4742	144	1.5844
190	1.4883	142	1.5832
195	1.5006	140	1.5915
200	1.5116	138	1.5995
205	1.5211 1.5284	136 134	1.6063 1.6156
210 215	1.5324	132	1.6261
220	1.5352	130	1.6394
225	1.5352		2.0004
230	1.5351		
235	1.5313		
245	1.5180		

Table 11. KMnCl₃·2H₂O plane 2 isentropic rotations - single.

θ	T(°K)	θ	T(°K)
9/8/70	12.25 kG	9/8/70	18.0 kG
170	1.1974	175	1.2849
165	1.1738	170	1.2712
160	1.1720	168	1.2697
155	1.1777	166	1.2747
150	1.1924	160	1.2818
145	1.2111	155	1.2840
140 130	1.2338 1.2857	150 145	1.2850 1.2856
125	1.3122	140	1.2884
120	1.3275	135	1.3013
115	1.3695	130	1.3270
110	1.3955	125	1.3559
105	1.4241	120	1.3830
100	1.4473	115	1.4090
95	1.4687	110	1.4265
90	1.4858	105	1.4498
85	1.5009	98	1.5036
80	1.5111	95	1.5261
75 70	1.5168	90	1.5568
70 65	1.5191 1.5184	85 80	1.5818 1.6016
60	1.5184	75	1.6130
55	1.5019	70 70	1.6178
50	1.4874	65	1.6164
45	1.4709	60	1.6074
40	1.4481	55	1.5905
35	1.4223	50	1.5662
30	1.3940	45	1.5356
25	1.3575	40	1.4955
20	1.3269	35	1.4516
13	1.2755	30	1.3942
10	1.2492	25	1.3662
4 0	1.2232 1.2160	20 15	1.3381 1.3118
353	1.1839	10	1.3016
350	1.1735	5	1.2886
345	1.1474	Õ	1.2742
340	1.1445	355	1.2747
335	1.1504	350	1.2600
330	1.1625	345	1.2680
		340	1.2729
		335	1.2753
		325	1.2768

Table 12. KMnCl₃·2H₂0 plane 3 isentropic rotations - single.

θ	T(°K)	θ	T(°K)
12/9/70	13.5 kG	12/9/70	20.0 kG
266	1.5754	64	1.4567
262	1.5733	72	1.4451
258	1.5722	76	1.4433
254	1.5722	80	1.4443
250	1.5734	88	1.4545
246	1.5759	96	1.4692
238	1.5824	104	1.4843
230	1.5913	112	1.4974
222	1.6003	120	1.5080
214	1.6091	128	1.5164
206	1.6172	136	1.5222
198	1.6238	144	1.5251
190	1.6285	152	1.5260
182	1.6320	160	1.5242
174	1.6336	168	1.5203
166	1.6334	176	1.5140
158 152	1.6314 1.6288	184 192	1.5059 1.4955
144	1.6241	200	1.4831
136	1.6241	208	1.4696
128	1.6097	216	1.4544
120	1.6008	224	1.4374
112	1.5913	230	1.4247
104	1.5813	238	1.4089
96	1.5722	246	1.3953
88	1.5648	250	1.3905
80	1.5608	254	1.3887
72	1.5613	258	1.3894
64	1.5659	262	1.3938
		268	1.4041

Table 13. KMnCl₃·2H₂O plane 4 isentropic rotations - single.

θ	T(°K)	θ	T(°K)	θ	T(°K)
12/11/70	13.0 kG	12/11/70	18.0 kG	12/11/70	14.5 kG
256	1.5062	244	1.4862	130	1.1732
248	1.5320	236	1.5016	132	1.1608
240	1.5320	232	1.5026	134	1.1481
234	1.5474	224	1.4908	136	1.1363
230	1.5454	216	1.4608	138	1.1283
222	1.5328	208	1.4150	140	1.1310
214	1.5078	200	1.3478	142	1.1359
206	1.4730	192	1.2731	144	1.1416
196	1.4150	184	1.2243	146	1.1468
188	1.3595	176	1.1984	148	1.1543
182	1.3143	168	1.1746	150	1.1652
174	1.2618	160	1.1413		
166	1.2312	154	1.1245		
158	1.1973	152	1.1309	12/11/70	15.0 kG
150	1.1657	148	1.1423	3.50	
148	1.1483	140	1.1466	150	1.1714
146	1.1238	136	1.1457	148	1.1620
144	1.1150	132	1.1410	144	1.1578
140	1.1219	128	1.1284	142	1.1596
136	1.1410	126	1.1299	140	1.1595
132	1.1647	124	1.1375	138	1.1540
124	1.2181	118	1.1757	136	1.1507
116	1.2657	110	1.2268	134	1.1554
108 102	1.3095 1.3498	102 94	1.2675	132	1.1679
94	1.4056	94 86	1.3167 1.3671		
84	1.4691	78	1.4294	12/11/70	15 5 kC
76	1.5015	78 70	1.4766	12/11/70	13.5 KG
68	1.5269	62	1.5060	130	1.1095
60	1.5406	52	1.5174	134	1.0954
54	1.5431	44	1.5054	134	1.1113
46	1.5370	44	1.3034	142	1.1174
37	1.5159			144	1.1150
0,	21020			148	1.1109
12/11/70	11.8 kG	12/11/70	13.5 kG	152	1.1244
132	1.2677	132	1.2244	12/11/70	16.5 kG
136	1.2569	134	1.2123	,,	
140	1.2494	136	1.2031	132	1.6127
144	1.2459	138	1.1897	136	1.5987
146	1.2457	140	1.1807	140	1.5933
148	1.2463	142	1.1779	144	1.5915
152	1.2522	144	1.1899	148	1.5961
156	1.2622	146	1.2079	152	1.6060
160	1.2778	148	1.2204	- -	

Table 14. KMnCl₃·2H₂0 isentropic magnetization boundary points.

T (°K)	H _{cl} (kG)	T(°K)	H _{C2} (kG)	T(°K)	H(kG)
1/27/70	twin	1/29/70	twin	2/13/70	single
				(inflect	cions)
0.997	11.80	1.041	14.46		
1.085	11.90	1.083	14.46	1.983	11.8
1.246	12.09	1.143	14.46	1.856	12.34
1.314	12.18	1.206	14.44	1.786	12.45
1.384	12.28	1.260	14.40	. 2.503	7.0
1.462	12.39	1.314	14.36	1.770	18.1
1.540	12.50	1.358	14.33		
1.602	12.62	1.409	14.33		
1.570	12.54	1.468	14.36		
1.583	12.57	1.516	14.54		
1.588	12.59		2		
1.617	12.60	3/5/70	single		
1/30/70	twin	1.208	13.84		
_, _, , ,		1.263	13.84		
1.540	12.50	1.388	13.86		
1.645	12.62	_,,,,,,,,,,,,,,,,,,,,,,,,,,,,,,,,,,,,,,			
1.0.3	22.02	3/10/70	single		
2/2/70	twin	3/10/70	Single		
2/2/10	CWIII	1.151	13.85		
1.437	12.37	1.495			
1.43/	12.37		13.95		
2 /6 /70	44	1.562	14.12		
2/6/70	twin	2 /3 5 /5 2			
		3/17/70	single		
1.620	12.62				
1.676	12.64	1.170	13.80		
		1.480	13.91		
8/27/70	single				
		8/27/70	single		
1.234	11.98		_		
1.283	12.02	1.240	13.80		
1.396	12.19				
1.520	12.41	8/28/70	single		
1.637	12.55	-,,			
		1.150	13.80		
8/28/70	single	1.252	13.85		
0,20,70	5111910	1.353	13.85		
1.142	11.83	1.432	13.90		

Table 15. KMnCl₃·2H₂0 specific heat maxima.

$^{ m H}{\parallel}$ easy	axis	$H_{ }$ eas	sy axis	$^{\mathrm{H}}$ _ ea	sy axis
T (°K)	H(kG)	T(°K)	H(kG)	T(°K)	H(kG)
1/30/70	twin	2/13/70	twin	12/2/70 H in pl	single
1.681	13.50	1.706	12.80	n in pr	ane I
2.120	11.00	1.865	12.80	2.698	8.00
2.039	11.50	2.000		2.585	14.00
1.945	12.00	2/25/70	twin	2.416	20.00
2/2/70	twin	1.574	16.30	12/7/70	single
-, -,		1.788	16.30	H in p	
1.603	14.00	1.784	15.03	<u>-</u> -	
1.567	14.20	1.797	14.06	2.578	8.00
1.715	13.00	2000	21.00	2.675	8.00
1.89	12.50	2/27/70	twin	2.278	14.00
2.192	10.50	2/21/10	CWIII	2.569	14.00
2.298	9.50	1.786	17.40	2.490	17.00
2.290	9.30	1.754	19.00	2.386	20.00
2/2/70	Acces to		20.20	2.300	20.00
2/3/70	twin	1.726	21.40	12/0/70	ainela
2 407	0 50	1.683	21.40	12/9/70	single
2.407	8.50	0/07/70			cond easy
2.485	7.50	8/27/70	single	··· a	xis
2.578	6.00	2 102	11 00	2 262	14.00
2.650	4.50	2.102	11.00	2.263	14.00
2.679	3.50	0 /00 /50		2.568	14.00
2.724	2.00	8/28/70	single	2.383	20.00
2.737	0.00				
		1.597	16.00		
2/6/70	twin	1.519	20.00		
		2.422	8.00		
1.500	14.50				
1.894	12.60	8/31/70	single		
2/9/70	twin	1.789	13.50		
		2.620	5.00		
1.558	15.64				
1.574	17.00	9/8/70	single		
1.563	18.00				
1.547	19.00	1.644	13.50		
2/10/70	twin				
1.536	20.20				
1.493	21.40				
1.552	15.00				
					•

Table 16. KMnCl₃·2H₂0 isentropic magnetizations.

H(kG)	T(°K)	H(kG)	T(°K)	H(kG)	T(°K)
8/28/70	single	3/27/70	twin	3/20/70	twin
11.64	1.1491	14.90	1.2177	12.00	1.5407
11.70	1.1458	14.80	1.2111	12.10	1.5367
11.76	1.1432	14.70	1.2106	12.20	1.5330
11.82	1.1491	14.60	1.2100	12.30	1.5293
11.88	1.1432	14.50	1.2095	12.35	1.5273
11.94	1.1485	14.40	1.2095	12.40	1.5255
12.00	1.1538	14.35	1.2099	12.45	1.5238
12.12	1.1576	14.30	1.2105	12.50	1.5232
12.30	1.1547	14.20	1.2122	12.55	1.5241
12.48	1.1503	14.10	1.2143	12.60	1.5253
12.72	1.1445	14.00	1.2163	12.65	1.5257
12.96	1.1378	13.90	1.2185	12.70	1.5254
13.20	1.1325	13.80	1.2203	12.80	1.5250
13.44	1.1263	13.70	1.2223	12.90	1.5244
13.68	1.1212	13.60	1.2241	13.00	1.5230
13.80	1.1194	13.50	1.2261	13.10	1.5217
14.04	1.1184	13.40	1.2279	13.20	1.5201
14.28	1.1185	13.30	1.2296	13.30	1.5183
14.52	1.1189	13.20	1.2313	13.40	1.5165
14.76	1.1194	13.10	1.2329	13.50	1.5148
15.00	1.1199	13.00	1.2346	13.60	1.5130
15.24	1.1204	12.90	1.2362	13.70	1.5109
		12.80	1.2378	13.80	1.5086
		12.70	1.2393	13.90	1.5071
		12.60	1.2406	14.00	1.5049
		12.50	1.2421	14.10	1.5029
		12.40	1.2430	14.20	1.5011
		12.35	1.2430	14.30	1.4997
		12.30	1.2421	14.40	1.4990
		12.25	1.2400	14.45	1.4987
		12.20	1.2349	14.50	1.4987
		12.15	1.2279	14.55	1.4993
		12.10	1.2238	14.60	1.5002
		12.05	1.2235	14.65	1.5011
		12.00	1.2252	14.70	1.5019
		11.95	1.2279	14.80	1.5029
		11.85	1.2323	14.90	1.5036
		11.80	1.2347	15.00	1.5043
		11.75	1.2374		

Table 17. KMnCl₃·2H₂0 critical field angular dependence, single crystal.

θ	H _{cl} (kG)	H _{c2} (kG)	θ	H _{cl} (kG)	H _{c2} (kG)
	8/27/70, plane T = 1.2°K	1	12/:	ll/70, plar T = 1.3°K	ne 4
135		13.80	145		14.31
137	12.38	13.88	147		14.17
138	12.16	13.96	149		14.06
139	11.00	14.03	152	10.60	13.97
140	11.99	14.02	153	12.60	12.06
141	11.98	14.03	155	10 47	13.96
142	11.99		156	12.47	14.05
143 145	12.02		158	10 40	14.05
145.	12.13 5 12.17		159 160	12.40	14.14
143.	5 12.17		162	12.37	14.14
			164	12.39	14.45
	9/8/70, plane	2	166	12.42	14.45
	T = 1.2°K	_	200		
162	12.65	13.49			
164	12.42	13.48			
166	12.29	13.50			
168	12.14	13.54			
170	12.04	13.61			
172	11.98	13.71			
173	11.95				
174	11.94	13.83			
175	11.94				
176	11.93	14.00			
177	11.93				
178	11.94	14.18			
179	11.96	14.00			
180	10.00	14.38			
181	12.00				
183	12.06				
185 187	12.16 12.26				
189	12.26				
109	14.73				

KMnCl $_3 \cdot 2\mathrm{H}_2$ 0 critical field angular dependence and rotation minima, twin crystal. Table 18.

θ	H _{c1} (kG)	H _{C2} (kG)	θ	H _{C1} (kG)	H _{C2} (kG)	H (kG)	θ minimum	
3/25/70 T =	, plane 1 1.2°K		3/19/ T	70, plane = 1.2°K	7	plane	l, T = 1.2°K 3/25/70	3/27/70
က		4.2	9		3.5	2	41,15	11,22
m		4.1	9		13.65	ب	39,15	10,22
4	2.9	3.9	9		3.7	13.5	140,152	210,223
4	2.5	4.1	9	12.19		4.	41,15	12,22
4	2.2	4.4	7		3.7	4.	4	
4	2.1	4.4	7	2.0	13.92	5.	4	216
4	12.09	4.4	7	2.0				
149	2.1	14.37	175	12.02	14.15	plane	$2, T = 1.2^{\circ}K,$	3/19/70
Ŋ		4.3	~	2.0				
2	2.2	4.3	7	2.0		7	~	
S	12.31	4.4	7	2.0		5	68,18	
S	2.5	4.6	∞	2.1		2	65,18	
			∞	2.1		.	62,19	
3/27/70	, pl					.	59,19	
H	1.2°K					14.0	157,173,196	
						4	55,17	
0		14.70				ъ.	53,18	
\vdash		4.1				9	50,18	
\vdash	2.4					7	48,19	
\vdash	2.5	•						
Н	2.0	4.3						
_	2.0							
\vdash	12.06	14.45						
_	2.0							
_		14.46						
2	12.28	4.3						
2	2.3							
~	2.9	4.0						
~		3.8						
226		13.98						
2		4.2						
က		4.6						

Table 19. KMnCl₃·2H₂0 specific heat data - twin.

T(°K)	C _p	T (°K)	C _p	T(°K)	Cp
2/3/70	0.0 kG	2/2/70,	14.0 kG	2/25/70,	16.3 kg
2.665	6.390	1.573	2.074	1.531	2.049
2.676	6.395	1.578	2.130	1.536	2.105
2.685	6.850	1.582	2.096	1.542	2.154
2.696	6.979	1.587	2.138	1.547	2.288
2.706	7.428	1.591	2.216	1.551	2.248
2.715	8.185	1.595	2.163	1.556	2.401
2.724	8.954	1.598	2.281	1.560	2.484
2.731	8.881	1.602	2.415	1.564	2.709
2.737	9.732	1.606	2.389	1.568	2.896
2.746	7.671	1.610	2.364	1.571	2.791
2.758	4.275	1.613	2.282	1.574	3.083
2.774	3.627	1.617	2.259	1.578	2.894
		1.621	2.255	1.581	2.889
2/3/70,	6.0 kG	1.625	2.161	1.585	2.883
		1.629	2.123	1.588	2.717
2.511	5.032	1.632	2.096	1.592	2.501
2.519	5.198			1.596	2.464
2.529	5.427	2/25/70,	14.0 kG	1.600	2.506
2.538	5.647			1.604	2.437
2.547	5.672	1.763	2.392	1.608	2.544
2.555	5.924	1.767	2.471	1.611	2.470
2.563	6.110	1.771	2.550	1.615	2.400
2.571	6.534	1.776	2.493	1.619	2.409
2.578	6.716	1.780	2.493	1.756	2.524
2.585	6.272	1.784	2.562	1.763	2.542
2.593	5.054	1.789	2.550	1.767	2.444
2.603	4.790	1.793	2.527	1.770	2.554
		1.797	2.603	1.774	2.573
1 /20 /70	11 0 1-0	1.800	2.530	1.778	2.662
1/30/70	11.0 kG	1.804	2.556	1.782	2.652
2 042	2 104	1.808	2.427	1.785	2.771
2.042	3.104	1.812	2.474	1.788	2.795
2.053	3.164	1.816	2.384	1.792	2.749
2.064	3.229	1.820	2.419	1.796	2.728
2.075 2.086	3.241 3.284	1.824 1.829	2.352	1.803 1.807	2.602 2.480
2.086		1.833	2.352 2.436	1.811	2.498
2.106	3.505 3.724	1.837	2.436	1.815	2.430
2.116	4.028	1.03/	2.423	1.819	2.421
2.116	3.933			1.823	2.475
2.125	3.708			1.827	2.435
2.130	3.286			1.021	2.77
2.159	3.109				
2.179	2.978				
	2.970				

Table 20. KMnCl₃·2H₂0 isentropic magnetizations, 2/13/70.

H(kG)		T(°K)	H(kG)	T(°K)
	(a)		(c)
5.6 6.8 6.2 6.6 6.8 7.2 7.4 7.8 8.2 8.6 8.9 9.2		2.539 2.534 2.530 2.525 2.520 2.515 2.510 2.503 2.496 2.496 2.485 2.482 2.478 2.474 2.471 2.469 2.469 2.464 2.462	11.5 11.6 11.7 11.8 11.9 12.0 12.1 12.2 12.3 12.4 12.5 12.6 12.7 12.8 12.9 13.0 13.1 13.2	1.897 1.893 1.888 1.884 1.880 1.875 1.870 1.865 1.859 1.852 1.847 1.843 1.839 1.836 1.839 1.829 1.825 1.825
	(b)		(d	
12.6 12.5 12.4 12.3 12.15 12.0 11.9 11.8 11.7 11.6 11.5 11.4 11.3 11.2	••	1.960 1.962 1.963 1.965 1.968 1.977 1.983 1.989 1.993 1.997 2.001 2.004 2.008 2.011 2.014	11.6 11.7 11.8 11.9 12.0 12.1 12.2 12.3 12.4 12.5 12.6 12.7 12.8 12.9 13.0 13.1 13.2	1.822 1.818 1.814 1.810 1.806 1.802 1.798 1.793 1.789 1.778 1.773 1.770 1.767 1.765 1.762 1.760 1.758

